

**Western Australian School of Mines: Minerals, Energy and  
Chemical Engineering  
Faculty of Science and Engineering**

**Experimental and Theoretical Study of Effects of Varying  
Hydration on Elastic Properties and Microstructure of Shales and  
Sandstones**

**Alexey Yurikov**

**This thesis is presented for the Degree of  
Doctor of Philosophy  
of  
Curtin University**

**December 2018**



## Declaration

To the best of my knowledge and belief this thesis contains no material previously published by any other person except where due acknowledgement has been made.

This thesis contains no material which has been accepted for the award of any other degree or diploma in any university.

Signature:  / Alexey Yarikov

Date: 21 December 2018

This thesis is dedicated to my grandmother, my first teacher and friend.

## Acknowledgments

This thesis would not be possible without help of many people who supported me during my research work.

First of all, I would like to express my deep gratitude to the fantastic trio of my supervisors, Prof. Maxim Lebedev, Dr. Marina Pervukhina and Prof. Boris Gurevich. Their valuable ideas, suggestions and contribution helped to shape this work. I wish to thank them for their continual guidance, encouragement and support in my research and daily life.

Importantly, I wish to thank Prof. Gennady Y. Gor for insightful discussions and meaningful contribution to this work.

I am grateful to Dr. Matthew Josh and Dr. Lionel Esteban for laboratorial and technical support.

I appreciate Dr. Valeria Shulakova and Dr. Vassili Mikhaltsevitch for contributing their time to help me to improve my knowledge and competencies.

I wish to thank Prof. Andrej Bona and Dr. Brett Harris for their guidance and support.

An essential part of my accomplishments in my research work is due to the inspiring and challenging atmosphere created and maintained by my fellow colleagues and peers at Curtin University and CSIRO. My special thanks go to Dr. Roman Beloborodov, Mr. Zubair Ahmed, Ms. Anastasia Pirogova, Ms. Nazanin Nourifard, and Mr. Yongyang Sun for fruitful discussions and sharing valuable ideas.

I wish to acknowledge Dr. Roman Pevzner, Dr. Konstantin Tertysnikov, Dr. Milovan Urosevic and members of the Curtin University seismic crew for their significant contribution to my professional development and for guidance during fieldwork.

I am grateful to Ms. Nichole Sik and Ms. Deirdre Hollingsworth for their administrative help and to Mr. Robert Verstanding for the IT support.

The Opalinus shale samples used in this research were kindly provided by CSIRO. I wish to thank Mr. David Nguyen for his technical assistance.

I am grateful to Dr. Roland Pellenq and Dr. Davoud Ebrahimi for sharing the results of their work with me.

I must acknowledge Ms. Pia Smith, a professional editor, for her help with proofreading of the thesis.

I must also acknowledge the sponsors of the Curtin Reservoir Geophysical Consortium (CRGC). This research was supported by the resources of the Pawsey Supercomputing Centre with funding from the Australian Government and the Government of Western Australia. This PhD program was funded by a Curtin Strategic International Postgraduate Research Scholarship and an Australian Government Research Training Program Scholarship.

Finally, I wish to thank my wife, Ms. Elena Iurikova, for her unconditional love and for inspiring me all along the way.

## **Abstract**

Understanding the dependence of the elastic properties of reservoir rocks on fluid content is of practical importance for the interpretation of seismic and acoustic well log data as well as the monitoring of fluid flow in the subsurface. While the mechanical effect of the pore fluid on elastic properties is well understood, the physico-chemical interaction of rocks with pore-filling fluid can also have a significant effect on the mechanical properties of rocks, introducing an additional challenge into reservoir characterisation. Therefore, it is important to understand how changes in fluid content affect the elastic properties and microstructure of rocks forming reservoir formations.

To explore these phenomena, I study the effects of changing fluid content on the elastic properties and microstructure of shales and sandstones, which constitute the majority of hydrocarbon reservoirs. The study includes obtaining comprehensive experimental data on the elastic properties and microstructure of rocks subjected to variations in fluid content. The study also contains theoretical quantitative and qualitative analysis of the obtained experimental data.

First, I develop an experimental procedure of ultrasonic measurements of elastic wave velocities in shale samples at different hydration states under applied pressure. Due to the low permeability of shales, it is extremely time-consuming to change the hydration in samples of the shape and size conventionally used in laboratory measurements. Therefore, in order to reduce the duration of experiments on shales, I design an experimental method of ultrasonic measurements on thin disc samples. The method is validated by comparison of the results of ultrasonic measurements on samples of both conventional and disc shapes. The validation of this experimental method is also supported by numerical simulations of stress distribution inside the samples of both shapes and propagation of elastic waves in the experimental setup.

Then, I measure the elastic properties of Opalinus shale in different hydration states using the developed experimental technique. The ultrasonic measurements are done under hydrostatic confining pressures of up to 50 MPa. Additionally, I investigate the influence of changing hydration on the microstructure of the Opalinus shale. It is found that the shale swells with hydration and shrinks with drying with no

visible damage. The pore space of the shale deforms, exhibiting a reduction in the total porosity with drying and an increase in the total porosity with hydration. The elastic properties of the shale show substantial changes with variations in hydration. The reported results show a drastic increase of shear velocities with drying, while velocities of compressional waves propagated along and normal to the bedding plane of the shales exhibit the opposite trends on hydration. This behaviour cannot be explained with a single driving mechanism.

Therefore in the next step, I suggest that changes of the elastic moduli with variations in hydration are driven by multiple competing factors: 1) variations in total porosity; 2) substitution of pore filling fluid; 3) change in stiffness of the contacts between clay particles; and 4) chemical hardening/softening of clay particles. I qualitatively and quantitatively analyse and discuss the influence of each of these factors on the elastic moduli. I conclude that, depending on the microstructure and composition of a particular shale, some of these factors dominate over others, resulting in different dependencies of the elastic properties on hydration. The theoretical analysis of the measured velocities under confining pressure shows that changing stiffness of the contacts between clay particles is an important factor that can explain, for example, the drastic increase of shear velocities with drying.

Due to the high structural complexity and heterogeneity of shales, it is extremely challenging to study the effect of the changing stiffness of contacts between particles with varying hydration as a stand-alone process. Therefore, in the next step, I study the same phenomenon in a less heterogeneous rock – Bentheim sandstone. I measure the elastic properties and deformation of the sandstone sample at low saturations, when water forms a thin film on the surface of grains, which fully saturates only thin compliant pores at grain contacts. I observe a very substantial (~20%) reduction in the P- and S-wave velocities and a strain of the order of  $10^{-4}$  with variation in saturation from 0.1 to 1–2%. I suggest that these two effects are driven by the change in pressure in the fluid adsorbed in small compliant pores. In order to validate this concept, I estimate the magnitude of the change in the fluid pressure from the measured deformation. Then, I compare the variations of the elastic properties related to the estimated fluid pressure against the stress dependencies of the bulk and shear moduli of the Bentheim sandstone measured in a triaxial cell. Broad agreement between the two sets of data and a reasonable

magnitude of the estimated change in fluid pressure is consistent with the suggested hypothesis.

The changing stiffness of compliant pores is a crucial driving factor affecting the elastic properties of rocks with variations in hydration. The research shows that the reduction in velocities of elastic waves with hydration in shales and sandstones seems to have a similar nature. Due to the high percentage of nano-scale compliant pores, this effect is much stronger in shales.

This work provides a unique set of experimental measurements of the elastic properties of shales and sandstones with changing hydration. The theoretical analysis of the experimental results advances understanding of the effect of fluid on the elastic properties of rocks. Eventually, this research has the potential to improve seismic and well-log interpretation and reservoir characterisation.

# Table of Contents

<b>Declaration</b> .....	3
<b>Acknowledgments</b> .....	5
<b>Abstract</b> .....	7
<b>Introduction</b> .....	12
<b>Research background</b> .....	12
<b>Objectives of the research</b> .....	15
<b>Overview of the thesis</b> .....	16
<b>List of publications related to the research project</b> .....	19
<b>Chapter 1. Ultrasonic measurements on thin disc samples under confining stress</b> .....	20
<b>1.1 Introduction</b> .....	20
<b>1.2 Methodology and the experimental setup</b> .....	22
<b>1.3 Numerical modelling of wave propagation</b> .....	25
<b>1.4 Comparison of measurements on thin and standard samples</b> .....	31
<b>1.5 Numerical modelling of stress distribution</b> .....	32
<b>1.6 Conclusions</b> .....	43
<b>Chapter 2. Experimental study of the effects of varying hydration on the elastic properties of shales</b> .....	45
<b>2.1 Introduction</b> .....	45
<b>2.2 Experimental method</b> .....	47
2.2.1 Studied samples .....	47
2.2.2 Hydration procedure .....	49
2.2.3 Characterisation of structural changes .....	49
2.2.4 Measurements of elastic properties .....	51
<b>2.3 Results</b> .....	52
2.3.1 Structural changes with varying hydration state .....	52
2.3.2 Variation of elastic properties with varying hydration state .....	55
<b>2.4 Conclusions</b> .....	57
<b>Chapter 3. Theoretical study of the dependency of the elastic properties of shales on hydration</b> .....	60
<b>3.1 Introduction</b> .....	60

3.2 The role of variation in the total porosity .....	61
3.3 The fluid substitution effect .....	62
3.4 Change of stiffness of contacts between clay particles .....	65
3.5 Chemical hardening/softening of clay particles .....	68
3.6 Conclusions.....	71
<b>Chapter 4. The effect of varying hydration on the deformation and elastic properties of sandstones .....</b>	<b>73</b>
4.1 Introduction.....	73
4.2 Materials and Methods.....	75
4.2.1 Studied sample.....	75
4.2.2 Control of saturation .....	76
4.2.3 Measurements of deformation .....	77
4.2.4 Ultrasonic measurements.....	77
4.2.5 Hydration procedure .....	78
4.3 Results .....	79
4.3.1 Deformation and saturation .....	79
4.3.2 Analysis of ultrasonic measurements .....	81
4.4 Analysis of results .....	85
4.5 Conclusions.....	90
<b>Chapter 5. Thesis conclusions.....</b>	<b>92</b>
<b>List of figures.....</b>	<b>96</b>
<b>List of tables .....</b>	<b>101</b>
<b>References.....</b>	<b>103</b>
<b>Appendices.....</b>	<b>119</b>
<b>Data and scripts .....</b>	<b>119</b>
Chapter 1.....	119
Chapter 2.....	121
Chapter 3.....	123
Chapter 4.....	124
<b>Attribution tables.....</b>	<b>125</b>
<b>Copyright permissions.....</b>	<b>128</b>

# Introduction

## Research background

Shales and sandstones are sedimentary rocks that constitute the majority of oil and gas reservoirs. Such rocks are heterogeneous media containing solid phase and pore space filled with various fluids. The physical properties of such heterogeneous media are determined by their composition, the properties of the individual components and the microstructure of rocks. For example, the fluid content is known to significantly affect the elastic properties of sedimentary rocks, which are crucial for exploration with seismic and acoustic well-log methods. One of the most important problems in rock physics analysis of seismic and acoustic data is characterisation of the fluid saturating a rock formation from elastic wave velocities. Solving this problem requires understanding the effect of fluid on the propagation of elastic waves in rocks. This effect is usually studied on core samples in laboratories, where various physical and chemical processes can be imitated and one can control the conditions of experiments, such as saturation of samples, confining pressure, temperature, etc.

Over the past few decades, propagation and attenuation of elastic waves in rocks saturated with fluids have been extensively studied. Excellent reviews of properties of fluid-saturated rocks can be found in Batzle and Wang (1992), Winkler and Murphy (1995), Mavko *et al.* (2009) and Müller *et al.* (2010). Generally, the presence of fluid in the pore space results in increased elastic moduli compared to those of a dry rock. This happens because the fluid stiffens the pores, resisting the compression of a rock. Biot (1956a, b) developed a theory for predicting the velocities of elastic waves in fluid-saturated rocks from dry-rock moduli. He showed that fluid-saturated rocks exhibit velocity dispersion and attenuation. In the low-frequency range, Biot's (1956a, b) predictions are consistent with the Gassmann's equation (Gassmann, 1951). In the low-frequency limit, the period of oscillations is sufficient for any pressure gradients in the fluid to vanish. In other words, solid and fluid are coupled and move in phase. The extensions of the Gassmann's equation and discussions of their applicability are reported, for example, by Brown and Korrington (1975), Berryman and Milton (1991), Zimmermann (1991), Berryman (1999), Smith *et al.* (2003), and Han and Batzle (2004). The low-frequency limit Biot-Gassmann

theory is often applicable for low-frequency seismic data ( $< 1$  kHz) and acoustic well logs ( $>10$  kHz). It may show discrepancy in the case of laboratory ultrasonic measurements ( $\sim 1$  MHz). In the case of higher-frequency oscillations, the pressure of the fluid in pores has no time to equilibrate, which results in the decoupling of solid and fluid movements. The critical frequency, when the motion of fluid and solid is decoupled, depends on the permeability and porosity of the rock as well as on the viscosity and density of the saturating fluid (e.g., Mavko *et al.*, 2009). The unrelaxed pressure gradients result in higher elastic moduli. Studies of the dispersion and attenuation of elastic wave velocities in fluid-saturated rocks report two driving mechanisms of this phenomenon: the macroscopic fluid flow, often called Biot's dispersion (Biot, 1956b; Geertsma and Smit, 1961; Biot, 1962; Stoll, 1977; Berryman, 1980), and microscopic flow, also called local flow or squirt flow (Mavko and Jizba, 1991; Dvorkin and Nur, 1993; Dvorkin *et al.*, 1994; Mukerji and Mavko, 1994; Gurevich *et al.*, 2010). In order to consider the dispersion of velocities, laboratory measurements are done using different methods operating in a wide range of frequencies. The most common methods used in laboratories are ultrasonic  $\sim$ MHz (Birch, 1960), resonant bar  $\sim$ kHz – MHz (Winkler and Nur, 1979), and quasi-static forced-oscillation  $<$  kHz (Spencer, 1981) techniques.

Another important aspect of fluid effect on the seismic properties of sedimentary rocks is the effect of partial or mixed saturation. This effect was extensively studied in the laboratory in past decades (e.g., Wyllie *et al.*, 1956; Wyllie *et al.*, 1962; Domenico, 1976; Clark *et al.*, 1980; Saito, 1981; Murphy, 1982; Knight and Nolen-Hoeksema, 1990; Tutuncu, 1992; Cadoret, 1993; Vales *et al.*, 2004; Wild *et al.*, 2005; Ghorbani *et al.*, 2009; Dell Piane *et al.*, 2014; Mikhaltsevich *et al.*, 2016, 2017; Szewczyk *et al.*, 2018). The simplest approach in rock physics modelling to deal with the mix of fluids is to replace the combination of different phases with a single effective fluid (Domenico, 1976), which reflects the macroscale behaviour of the rock. Properties of this effective fluid depend on the properties and volume fractions of all constituting phases and the scale of heterogeneities in the fluid mix. In particular, when phases of immiscible fluids are mixed at the finest scale or, in other words, wave-induced pore pressure has enough time to equilibrate among the phases (low-frequency regime), the bulk modulus of an effective fluid is well described with an isostress Reuss (1929) average:

$$\frac{1}{K_{fl}} = \sum_i \frac{s_i}{K_i} \quad (1)$$

where  $K_{fl}$  is the bulk modulus of the effective fluid,  $K_i$  and  $s_i$  are the bulk moduli and saturations of individual phases of the mixture. If the size of heterogeneities in the mix of fluids exceeds the so-called diffusion length

$$L_D = \sqrt{D/f}, \quad (2)$$

where  $D$  is the diffusivity, and  $f$  is the frequency of the propagating wave, there is no time for fluid pressure to equilibrate among different phases. Thus wave-induced pore pressure heterogeneities, also called patches, result in spatially varying bulk modulus in the rock. The elastic moduli of individual patches are described locally by Gassmann's equation with the effective fluid bulk modulus determined by equation 1. Then the effective moduli of patchy saturated rock can be described by Hill's (1963) relation:

$$K_{eff} = \left( \sum_i \frac{f_i}{K_i + 4/3\mu_i} \right)^{-1} - \frac{4}{3}\mu_{eff}, \quad (3)$$

where  $K_{eff}$  and  $\mu_{eff}$  are the effective bulk and shear moduli of the patchy saturated rock,  $K_i$  and  $\mu_i$  are the bulk and shear moduli of the individual patches, and  $f_i$  are the volumetric fractions of patches.

The partial water-saturation effect – i.e., the effect of the mix of water and gas – on the elastic properties of sandstones is generally well described by the Biot-Gassmann and squirt-flow theories with effective fluid and patchy saturation approaches – as was discussed, for example, by Murphy (1984), Cadoret (1993) and Mavko and Nolen-Hoeksema (1994). However, these theories and approaches do not describe the behaviour of the elastic properties of sandstones at very low saturations. It is observed that a small increase in water content in dry sandstones as the result of adsorption leads to a drastic drop in velocities and an increase in attenuation of elastic waves at all ranges of frequencies (e.g., Clark *et al.*, 1980; Murphy, 1982; Knight and Nolen-Hoeksema, 1990; Tutuncu, 1992; Cadoret, 1993; Pimienta *et al.*, 2014). This effect is often called elastic weakening. It is of practical importance for near-surface seismic studies and for applications of conventional rock physics theories, which require measurements of the elastic properties of dry rocks (Rasolofosaon and Zinszner, 2004). Due to the very low amount of water, this effect cannot be attributed to purely mechanical interactions as in the Biot-Gassmann or squirt-flow theories. The measurements show that the ultra-dry effects are strong

even in sandstone – rocks with relatively simple microstructure. The observed effects have been explained by the softening of cement, swelling of clays, and change of surface energy (e.g., Murphy *et al.*, 1984; Mavko and Nolen-Hoeksema, 1994; Pimienta *et al.*, 2014). However, these ultra-dry effects are still not fully understood.

Similar effects of partial water saturation on the seismic properties of shales are even more challenging to study because of their complex morphological features. First, shales are highly anisotropic, which introduces additional challenges to shale characterisation (e.g., Vernik and Nur, 1992). Second, shales often have small pores and low permeability, which complicates control of the saturation in the rock, making hydration or drying of shales extremely time-consuming (e.g., Ferrari *et al.*, 2014). Third, shales contain high amounts of clay, which is highly reactive to water. For example, smectite tends to swell with an increase in water content. Thus, variations in saturation in shales lead to microstructural changes such as expansion or contraction of samples, or induction of microfractures (e.g., Romero *et al.*, 2011). Due to the complexity of laboratory study of the dependence of the elastic properties of shales on water content, the number of such studies is limited (Vales *et al.*, 2004; Wild *et al.*, 2005; Ghorbani *et al.*, 2009; Dell Piane *et al.*, 2014; Mikhaltsevich *et al.*, 2017; Szewczyk *et al.*, 2018;). Moreover, the data reported in different works for different shales seem contradictory. For example, different dependencies of elastic wave velocities on water content are reported for Tournemire shale (Vales *et al.*, 2004), Callovo-Oxfordian argillite (Ghorbani *et al.*, 2009) and Mancos shale (Szewczyk *et al.*, 2018). Additionally, Ghorbani *et al.* (2009) observed that S-wave velocities in Callovo-Oxfordian argillite samples exhibit strong weakening with hydration, which cannot be described using conventional Biot-Gassmann theories. Currently there is no comprehensive rock physics theory describing the behaviour of the elastic properties in shales with changing water content. Broadly, the reasons for differences between dependencies of elastic wave velocities on hydration in different shales are not fully understood.

### **Objectives of the research**

The main objective of this research is to investigate the effect of varying water content on the elastic properties of common sedimentary rocks, namely shales and sandstones. To achieve this objective, the research aims first to measure the dependence of the elastic properties of these rocks on water content. The

experimental measurements are focused on an ultrasonic frequency range. Second, the analysis of the experimental data is performed to advance understanding of the mechanisms of the effect of fluid on the elastic properties of sedimentary rocks. Eventually, this work has the potential to improve seismic and well-log interpretation and reservoir characterisation.

## **Overview of the thesis**

The first part of the thesis is focused on investigation of the effect of varying water content on the elastic properties of shales. Control of water content in shales in laboratories is usually done with a desiccation technique involving a sorption process (e.g., Greenspan, 1977). Such a technique is always time-consuming if applied to shales due to the small pore size and low permeability of this rock (e.g., Ferrari *et al.*, 2014). In order to decrease the time required for stabilisation of saturation in shale samples, I use thin disc samples (~15 mm long) instead of the standard plugs (~40–100 mm long) typically used for ultrasonic measurements in the laboratory. Therefore, in **Chapter 1**, I develop and validate an experimental technique for laboratory ultrasonic measurements on thin (~15 mm long) disc samples. Such samples are not typically used for measurements due to the implication of the inhomogeneity of the stress fields inside. While a few results of measurements on thin disc samples have been reported in the literature, detailed justifications of the procedures have not yet been done. To fill this gap, I compare ultrasonic velocities measured at confining stresses up to 50 MPa done on standard and thin samples with diameters of 38.5 mm and lengths of 60 and 15 mm, respectively. I determine how to reliably measure the elastic properties of the rocks using the thin samples. **Chapter 1** gives detailed description and validation of the experimental procedure, supported by numerical modelling of the stress distribution and propagation of elastic waves in the experimental setup.

The experimental procedure developed – of ultrasonic measurements on thin disc samples – is used in **Chapter 2** to investigate the effect of varying water content on the elastic properties of Opalinus shale. The elastic moduli of the shale exhibit substantial changes with variation in hydration. Decrease in the water content of the shale leads to a strong increase in the shear wave velocities and the velocity of the compressional wave propagating in the bedding plane. On the contrary, the velocity of the compressional wave propagating perpendicular to the bedding plane of the

shale decreases with drying. In order to better understand the effect of varying water content on the elastic properties of the shale, I obtain the elastic velocities' dependencies on confining stress, and characterise structural changes in the shale at different hydration states. The characterisation of microstructure is done using laboratory measurements and X-ray micro-computed tomography. I observe that the measured velocities are stress-dependent and the shale swells with hydration and shrinks with drying with no visible damage. The pore space of the shale deforms exhibiting reduction/increase of the total porosity with drying/hydration.

In **Chapter 3**, I use the obtained experimental data to highlight and analyse the main driving factors for the effect of varying water saturation on the elastic properties of the Opalinus shale. I suggest that this effect is driven by several competing factors: 1) variations in the total porosity; 2) substitution of pore-filling fluid; 3) change in stiffness of the contacts between clay particles; and 4) chemical hardening/softening of clay particles. I perform qualitative and quantitative analysis of the data using a number of rock physics models and theories, and discuss the influence of each of these factors on the elastic moduli of shales. First, I conclude that, depending on the microstructure and composition of a particular shale, some of the factors dominate over the others resulting in different moduli dependencies on hydration. Second, I show that a change in stiffness of the contacts between clay particles plays an important role in the studied effect. Due to the high complexity and heterogeneity of shales, the building of a comprehensive rock physics model describing the observed phenomena is challenging and requires good understanding of every factor responsible for the behaviour of the elastic properties.

Therefore, in the second part of the thesis, I focus on the effect of changing hydration on the stiffness of the contacts between particles that dictates the stiffness of the rock. In order to better understand this effect, I select sandstone as the subject of this study. Sandstones are usually isotropic and have a less complex structure than shales. At low saturations, water forms a thin film on the grains constituting sandstones and fully saturates only the small compliant pores located at the contacts between grains. A number of studies show that an increase in water content at low saturations gained by changes in air humidity leads to adsorption of a small amount of water, and results in significant reduction of the elastic moduli and increase of elastic waves attenuation. Additionally, adsorption of water is known to cause deformation of porous materials and rocks (e.g., Gor *et al.*, 2017). Thus, in **Chapter**

4, I investigate the effect of changing water content at low saturations on the elastic properties and deformation of Bentheim sandstone. I simultaneously measure the deformation and the change in the elastic properties in the same sample with sorption of water. Upon adsorption/desorption, the sample exhibits ~20% change in the bulk and shear dynamic moduli, accompanied by strain of the order of  $10^{-4}$ . In order to cause deformation of the sandstone of such magnitude, it is necessary to apply stress of the order of several MPa. Such stress can originate from changing fluid pressure (also called solvation pressure) in compliant pores on grain contacts, which is also responsible for the adsorption-induced elastic weakening of the sandstone. In order to validate this concept, I compare the measured variations of the elastic moduli related to the estimated change in solvation pressure with the stress dependency of the bulk and shear moduli in Bentheim sandstone. I observe a broad agreement between the two sets of measurements. Additionally, a reasonable magnitude of the estimated change in solvation pressure is consistent with the suggested hypothesis.

Therefore, this research improves understanding of the effect of changing water content in shales and sandstones and discusses an important mechanism of the influence of changing water content on the elastic properties of the rocks. A summary of the main outcomes of this work and suggestions about future research directions are given in **Chapter 5**.

The results reported in the thesis are the outcome of collaborative work with researchers from Curtin University, CSIRO Energy and the New Jersey Institute of Technology. The experimental work reported in Chapters 1, 2 and 4 is done by me under the guidance of my supervisor, Prof. Maxim Lebedev. I performed the numerical modelling (Chapters 1 and 3) under the guidance of Dr. Marina Pervukhina. The analysis of the experimental data in Chapter 4 is done in collaboration with Prof. Boris Gurevich and Prof. Gennady Gor. The explicit declaration of contribution of each co-author to this work is presented in the Appendices.

## **List of publications related to the research project**

The chapters of the thesis are extended versions of the following publications. All copyright material, where necessary, has been reproduced with permission.

### ***Journal papers:***

Yurikov, A., M. Lebedev, and M. Pervukhina, 2018, Ultrasonic velocity measurements on thin rock samples: experiment and numerical modelling: *Geophysics*, **83**(2), MR47–MR56, doi: 10.1190/GEO2016-0685.1.

Yurikov, A., M. Lebedev, M. Pervukhina, and B. Gurevich, 2018, Water retention effects on elastic properties of Opalinus shale: *Geophysical Prospecting*, Special Issue, doi: 10.1111/1365-2478.12673.

Yurikov, A., M. Lebedev, G. Gor, and B. Gurevich, 2018, Sorption-induced deformation and elastic weakening of Bentheim sandstone: *Journal of Geophysical Research – Solid Earth*, **123**(10), 8589–8601, doi: 10.1029/2018JB016003.

### ***Conference proceedings:***

Yurikov A., M. Lebedev, and M. Pervukhina, 2016, Ultrasonic measurements on thin samples: numerical modelling, 25<sup>th</sup> International Geophysical Conference and Exhibition, ASEG Extended Abstracts, 327–331.

Yurikov A., M. Lebedev, and M. Pervukhina, 2016, Ultrasonic measurements on thin samples: experiment and numerical modelling, SEG International Exposition and 86th Annual Meeting, SEG Technical Program Expanded Abstracts, 3338–3342.

Yurikov A., M. Lebedev, and M. Pervukhina, 2017, Water retention effects on the elastic properties of Opalinus shale, 4<sup>th</sup> International Workshop on Rock Physics, Trondheim, Norway.

Yurikov, A., M. Lebedev, M. Pervukhina, and B. Gurevich, 2018, Experimental and theoretical study of water retention effects on elastic properties of Opalinus shale, First Australasian Exploration Geoscience Conference, AEGC Extended Abstracts: Poster Complete Session, 252–259.

# Chapter 1. Ultrasonic measurements on thin disc samples under confining stress<sup>\*</sup>

## 1.1 Introduction

The ultrasonic pulse transmission (UPT) method is widely used for laboratory measurements of the elastic properties of rocks (e.g., Hughes and Cross, 1951; Birch, 1960; Steward and Peselnick, 1977; Vernik and Nur, 1992; Mah and Schmitt, 2001; Nakagawa *et al.*, 2002; Prasad, 2002; Kitamura *et al.*, 2003; Schubnel *et al.*, 2003; Fortin *et al.*, 2007; Kono *et al.*, 2009; Blake *et al.*, 2012; Lebedev *et al.*, 2013; Sarout *et al.*, 2014; Bauer *et al.*, 2016). Over the past decades, the method was elaborated and many challenging aspects of ultrasonic measurements have been addressed (e.g., Dellinger and Vernik, 1994; Molyneux and Schmitt, 2000; Dewhurst and Siggins, 2006). One of the major improvements of the UPT method is the possibility of velocity measurements under controlled confining and uniaxial stresses (e.g., Christensen and Wang, 1985; Scott *et al.*, 1993; Dewhurst and Siggins, 2006; Ougier-Simonin *et al.*, 2011). Accurate measurement of the stress dependencies of the elastic properties of rocks allowed prediction of perturbations of velocity caused by changes in stress related to the production or injection of fluids. The availability of such measurements has also led to the development of theoretical models that allow insight into the microstructure of rocks (e.g., Sayers and Kachanov, 1995; Saenger *et al.*, 2006; Pervukhina *et al.*, 2010, 2011; De Paula *et al.*, 2012). Accurate calibration of the time-lapse seismic responses caused by changes in stress requires establishing correct stress dependencies of the velocities of elastic waves, which implies uniform and homogeneous loading of samples during the ultrasonic experiments. The stress field in a sample depends on its size and shape. Thus the standards for the dimensions of rock samples used in UPT measurements were established in the early studies (e.g., Hughes and Cross, 1951; Birch, 1960). Birch (1960) showed that the most convenient sample shape is cylindrical, and the length-

---

<sup>\*</sup> This chapter is an extended version of the paper Yurikov, A., M. Lebedev, and M. Pervukhina, 2018, Ultrasonic velocity measurements on thin rock samples: experiment and numerical modelling: *Geophysics*, **83**(2), MR47–MR56, doi: 10.1190/GEO2016-0685.1

to-diameter ratio of a sample should not exceed five to prevent excessive energy dissipation by wave reflections on the sample's boundaries. The length-to-diameter ratio of samples required for ultrasonic measurements was further influenced by the rock mechanics sample preparation procedure, which requires the length of the sample to be at least two times larger than the diameter to insure uniform loading. Over the years, these constraints on the length-to-diameter ratio became industry standards (ASTM International, 2008, 2014). Nowadays, typical samples used for ultrasonic measurements are cylinders with 20–50 mm diameter and 40–100 mm length. Hereafter I refer to such samples as standard samples.

Ultrasonic velocity measurements are often performed on samples subjected to desiccation and saturation with different fluids. Such experiments might be extremely time-consuming if done on samples of 40–100 mm length. For example, the desiccation process can take several months to stabilise saturation of low-permeable samples of the standard size (e.g., Ferrari *et al.*, 2014). Thinner samples are preferable for such studies. Ultrasonic velocity measurements are often combined with other measurements on the same rock samples. For instance, comprehensive characterisation of rocks usually comprises dielectric permittivity measurements that are used to quantify the water content (Garrouch and Sharma, 1994; Jones and Friedman, 2000; Josh *et al.*, 2012). Thin disc samples (10–15 mm long) are required for such experiments (Josh, 2014). Moreover, researchers often have to work with limited core material or brittle rocks, making manufacturing of the standard samples challenging.

In spite of these three obvious reasons to cut down the length of samples used for ultrasonic velocity measurements – namely, economy of rock material, shorter saturation/desiccation time, and compatibility with other experimental setups – just a few measurements on shorter samples were reported (e.g., Fujii and Kawashima, 1995; Kitamura *et al.*, 2003; Kono *et al.*, 2009). One possible reason for the limited use of short samples is the implication of an inhomogeneous stress distribution in such samples. However, the issue of stress distribution inside tested samples should be addressed for each experimental setup, as is done for geomechanical experiments in, for instance, Yoshikawa and Mogi (1990), Raper and Erbach (1990), Özcan *et al.* (2009), and Saksala *et al.* (2013). For example, Saenger *et al.* (2014) applied finite-element method (FEM) modelling to check the homogeneity of stress distribution inside the standard cylindrical samples used for low-frequency measurements.

In this study, I compare ultrasonic velocity measurements done on standard plugs (38 mm diameter, 60 mm length) and thin discs (38 mm diameter, 15 mm length). In the first section I describe a newly developed experimental setup for UPT measurements on thin discs. The next section covers important aspects of the design of the experiment setup, where the use of shear transducers for measurements of both P- and S-wave velocities is validated with the FEM modelling of elastic waves propagation. In the next section, I compare the results of experimental measurements on standard and thin disc samples of selected sets of rocks and materials. Then I use FEM modelling to estimate the stress distribution in samples of both types in the experimental rig. Finally, I discuss how the geometry of the experimental rig influences the results of UPT measurements and show how to obtain reliable elastic properties of rocks from measurements on thin disc samples.

## 1.2 Methodology and the experimental setup

To investigate the feasibility of UPT measurements on thin disc samples and to benchmark the obtained experimental results on the measurements done on standard plugs, standard cylindrical samples with 60 mm length and 38 mm diameter are prepared from poly-methyl methacrylate (PMMA), dry Berea sandstone, dry Bentheim sandstone, and preserved Opalinus shale (see Figure 1). The thin disc of 15 mm length is cut off from each standard sample after the ultrasonic velocities are measured. By doing this, I am trying to minimise the effect of heterogeneity in natural samples.

I use a two-transducer pulse transmission technique to obtain ultrasonic P- and S-wave velocities ( $V_P$  and  $V_S$ ). The schematic of the arrangement of experimental equipment is shown in Figure 2. A rectangular form electrical pulser / receiver 5077PR (Olympus Ltd.) and a digital phosphor oscilloscope TDS 3034C (Tektronix Ltd.) are used to generate and acquire electrical signals. A pair of piezoelectric shear transducers V153 1 MHz / 0.5 in. (Olympus Panametrics-NDT<sup>TM</sup>) is used as a source and a receiver of ultrasonic pulses. Such transducers generate and register both P- and S-waves as was demonstrated previously in experiments (e.g., Lebedev *et al.*, 2013). In the following section, I report the results of FEM numerical modelling of the propagation of elastic waves generated and captured by shear transducers, which validates the used technique. In the experiment, all electronic

components are synchronised in time. The dead time of the electronics and the dead time of the transducers are taken into account by calibration of the system.



**Figure 1** PMMA, Berea sandstone, Bentheim sandstone, and Opalinus shale samples. Standard samples, 60 mm long, were used for experimental measurements first. Then 15 mm long thin-disc samples were cut out of the standard plugs. The Opalinus shale sample shown in the figure is before cutting.

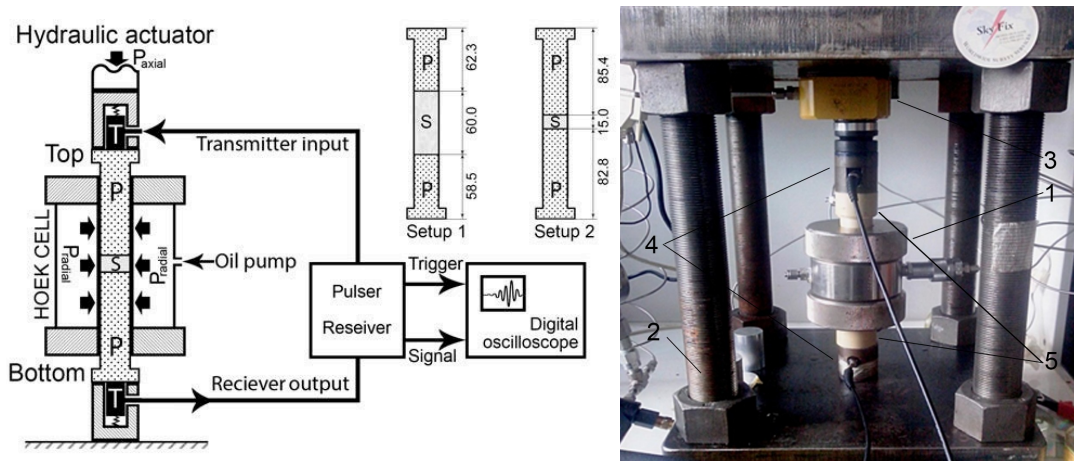


**Figure 2** Left: schematic of the arrangement of the experimental equipment: T, transducer; P, PEEK piston; and S, sample. Setups 1 and 2 at the top right corner show the standard and thin disc samples, respectively, placed between short and long PEEK pistons. Right: image of the apparatus: the Hoek cell (1), the steel frame of the rig (2), the hydraulic actuator (3), the transducers (4), and the PEEK pistons (5).

A sample is placed inside a rubber sleeve (38.5 mm inner diameter) in the Hoek cell between two polyether ether ketone (PEEK) pistons. The measurements are done under hydrostatic stress in a range from 2 to 50 MPa. The axial stress is applied to the cylindrical samples by a hydraulic actuator mounted at the top of the experimental rig, whereas the radial stress is applied directly to a jacketed sample via

pressurised hydraulic oil (Figure 2). In addition to the delivery of the axial stress to samples inside the Hoek cell, the PEEK pistons are used to separate P- and S-wave arrivals in time and to ensure a planar wavefront when the pulse reaches the tested samples (Lebedev *et al.*, 2013). I use two pairs of PEEK pistons (short and long) for the standard and thin disc samples, respectively. Thus, I perform the experiment with two different setups, as shown in Figure 2. The length-to-diameter ratio of both setups does not exceed five, thus Birch's (1960) condition is met.

Typical records of waveforms are shown in Figure 3. As reported by Lebedev *et al.* (2013), the traveltimes of the P-wave can be determined as the moment of the first onset of energy, whereas the traveltimes of the S-wave corresponds to the moment of arrival of the high-magnitude signal. To ensure a consistent approach and to enhance the precision of the picking of traveltimes, I apply the algorithms of automatic picking described, for example, by Akram and Eaton (2016). I use an iterative cross-correlation-based workflow (De Meersman *et al.*, 2009) applied for a set of waveforms obtained for the same sample under different hydrostatic stresses. The initial picking of traveltimes required for the workflow is done using the short- and long-time average ratio method (STA / LTA) (Trnkoczy, 2002) in time windows localised in the neighbourhood of P- or S-wave arrivals. This workflow is applied independently for the detection of P- and S-wave traveltimes.

Implementation of the described workflow is feasible due to the use of PEEK pistons in the experimental setup, because the arrivals of P- and S-waves are separated in time by more than  $50 \mu\text{s}$ , the S-wave signal is less contaminated with multiple oscillations, and it is possible to locate time windows for an STA / LTA algorithm of sufficient width capturing only the P-wave or only the S-wave. The elastic properties of PEEK pistons are stress-dependent. Therefore, I calibrate the measurements to take into account the traveltimes of P- and S-waves in PEEK in the pressure range 2–50 MPa for both experimental setups. To this end I measure the traveltimes of the elastic waves through the experimental setups with aluminium samples (15 and 60 mm long) with known elastic moduli. The elastic properties of aluminium do not change under stresses up to 50 MPa, thus it is straightforward to use this material for the calibration.

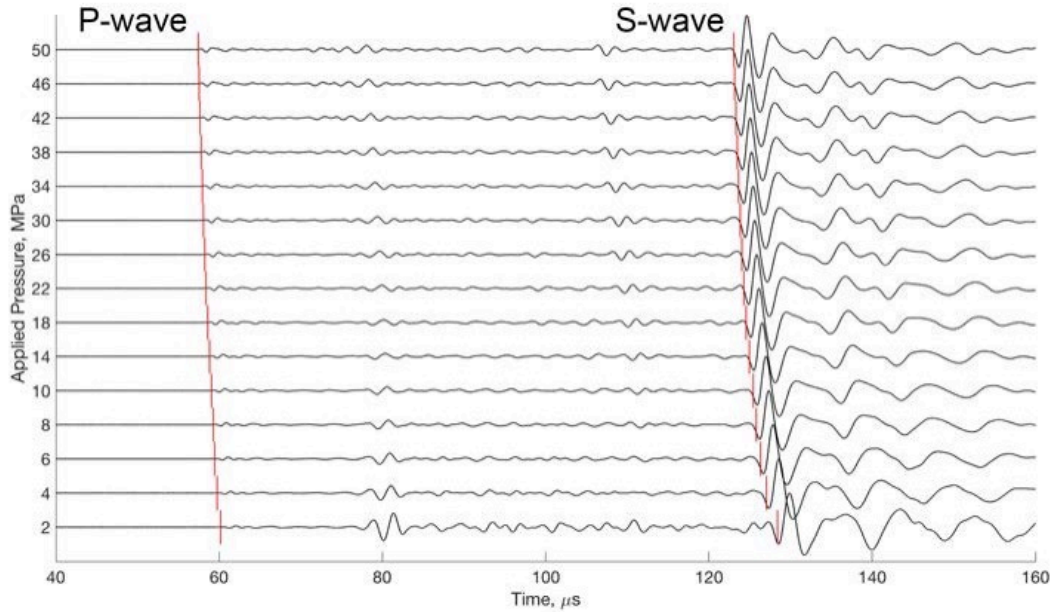


**Figure 3** The example of experimentally obtained waveforms on a setup with a standard dry Berea sandstone. The red vertical lines show the determined arrivals of the P- and S-waves.

### 1.3 Numerical modelling of wave propagation

The developed experimental technique of UPT measurements involves using a pair of shear transducers to generate and register both P- and S-waves. Lebedev *et al.* (2013) demonstrated how P- and S-wave arrivals could be detected at recorded waveforms (also see Figure 3). In order to validate this technique and to highlight the mechanism of initiation and propagation of P- and S-waves emitted by shear transducers, I perform an FEM numerical modelling of the propagation of elastic waves using Abaqus Finite Element Analysis software (Dassault Systèmes).

I build a 3D model of a standard 50 mm long aluminium sample (Figure 4a). I allocate the nodes at the top of the sample that correspond to the area where the source transducer is attached ( $S_a^{src}$  at Figure 4a). I assume that the source shear transducer produces only shear displacement in the plane of the transducer's polarity. Thus I apply a time-dependent displacement boundary condition to the nodes within  $S_a^{src}$  to simulate the initiation of the ultrasonic pulse. The polarity of the transducer in Figure 4a is in the XY plane, and the shear displacement is simulated by movement of the  $S_a^{src}$  nodes along the X-axis. The form of the input pulse (Figure 4b) is obtained experimentally by putting the source and the receiver transducers into direct contact. Propagation of the ultrasonic pulse through the sample is simulated using the Abaqus Dynamic Explicit solver.

Work of the receiver transducer is simulated similarly to the source transducer. I allocate nodes at the bottom of the sample corresponding to the area where the receiver is attached ( $S_a^{rcv}$  at Figure 4a). I assume that the shear receiver registers only shear displacement of the surface of the sample in the direction of the transducer's polarity, i.e. along the X-axis. The X-displacement is integrated over the nodes in the  $S_a^{rcv}$  area to obtain the signal captured by the receiver at each time step. Such simplified representation of the receiver transducer does not give an opportunity to directly compare experimentally recorded waveforms with simulated signals, but allows validation of the picking of the traveltimes of P- and S-waves.

The material of the sample is set to be purely elastic with the elastic moduli and density of aluminium ( $E_{al} = 69.8$  GPa,  $\nu_{al} = 0.34$ ,  $\rho_{al} = 2.7$  kg/m<sup>3</sup>). The spatial cell dimensions are chosen to satisfy the condition that at least ten spatial cells per wavelength are needed to capture wave propagation accurately. As the slowest wave is a shear wave propagating in aluminium with the velocity of  $\sim 3000$  m/s and its frequency is  $\sim 1$  MHz, the cell size should be smaller than 0.3 mm. To be on the safe side, I set the size of spatial cells twice as small as this value,  $\Delta l = 0.15$  mm (Figure 4c). The time step  $\Delta t < 10^{-7}$  s is chosen to satisfy the Courant–Friedrichs–Lewy condition.

Figure 5 shows the results of the FEM modelling of the propagation of elastic waves. A set of snapshots made at three sequential moments in time shows displacement of nodes in the computational domain. A cross-section shown in Figure 5 cuts the cylinder along its symmetry axis in the XY plane – the plane of the shear transducers' polarity. The first and second rows of the snapshots show the magnitude of displacement of the nodes along the X-axis (transverse displacement) and the Y-axis (normal displacement), respectively. The transverse displacement of the nodes is initiated first in the area of the source transducer, and then propagates through the sample with the S-wave velocity.

The first image in the second row of snapshots shows that two regions of the normal displacement of the same magnitude and the opposite direction are formed at the moment of initiation of the shear pulse. These displacements correspond to the compression and dilation of the sample caused by the displacement of the source transducer parallel to the top surface of the sample. Thus along with emitting the S-

wave, the shear transducer initiates the compressional dipole that causes an ensemble of P-waves. This ensemble propagates through the sample with the P-wave velocity.

At the moment when the compressional dipole reaches the bottom of the sample, dilation of the sample's material at the left and compression at the right causes displacement of the nodes along the X-axis, where the shear receiver is placed (Figure 6). Even if the simplified representation of the receiver transducer is used and the normal displacement of the adjacent nodes is not captured, the registration of the P-wave arrival with such a transducer is feasible because of the compressional dipole, which causes the shear displacement between the compression and dilation zones.

Figure 7 shows a comparison of the simulated average displacement in the receiver zone with the results of actual UPT measurements on the standard aluminium sample with the same geometry as used in the modelling. I do not directly transform the simulated average displacement of the receiver nodes into the form of electrical signal because the focus of the comparison is the arrival of the P- and S-waves. This does not require such transformation, which could be non-linear.

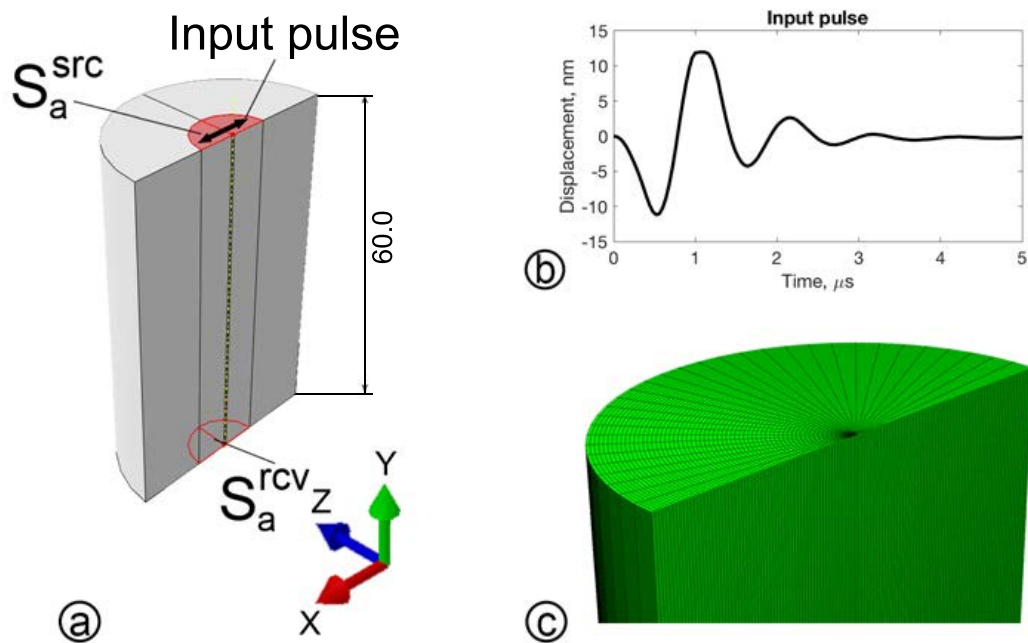


**Figure 4** a) A cross-section of the 3D model of the standard aluminium sample. b) The input pulse. c) An example of meshing.

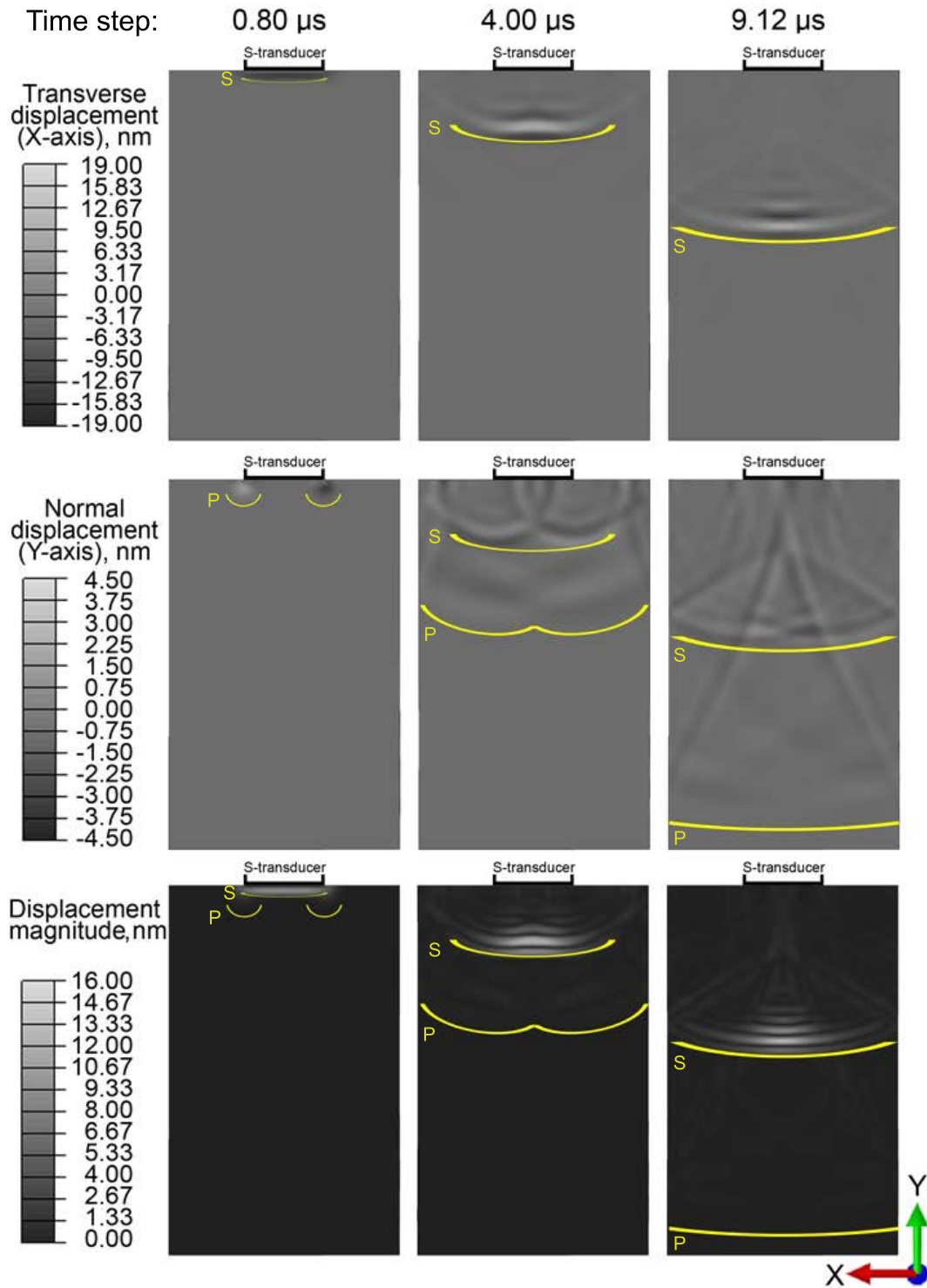


**Figure 5** The results of FEM modelling of the propagation of elastic waves through the standard aluminium sample. The figure shows the cross-section of the sample made through its vertical axis of symmetry in the XY plane, the plane of the shear transducers polarity. Two components of the displacement of nodes and their total magnitude are shown in the first, second and third rows, respectively. Three vertical columns show these parameters at

three sequential moments in time. The fronts of the P-wave dipole and the S-wave are highlighted.

The first onset of energy and the arrival of the high-amplitude signal could be easily picked at the experimental waveform. The time of the first onset at the experimental waveform is in a good agreement with the time of arrival of the simulated P-wave caused by the compressional dipole. Additionally, the arrival of the high-amplitude signal at the experimental waveform matches the traveltimes of the simulated high-amplitude shear oscillation.

Therefore, when shear transducers are used as a source and a receiver of the ultrasonic pulse, the first onset of energy is related to the arrival of the P-wave, the velocity of which is higher than the velocity of the S-wave. The arrival of the S-wave is denoted by the moment of registration of high-energy oscillations. The amplitude of the P-wave is significantly lower than the amplitude of the S-wave because the P-wave propagates in the form of the compressional dipole generated by minor compressional and dilatational strains produced by the shear transducer, as can be seen in Figure 5 and Figure 6. The performed FEM modelling improves understanding of the initiation and propagation of the elastic waves emitted by a shear transducer, justifies use of a shear transducer as a receiver of both P- and S-waves, and facilitates the method of picking the traveltimes.

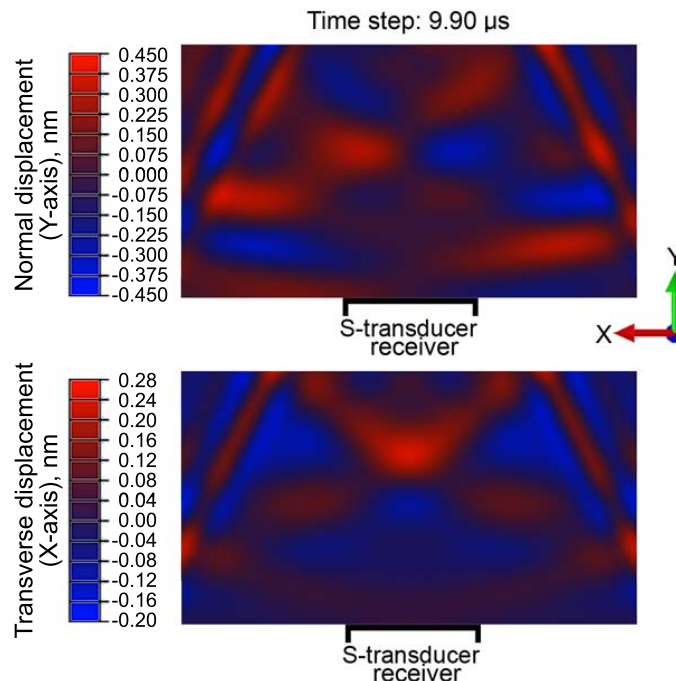


**Figure 6** Example of the displacement field at the bottom part of the standard aluminium sample when the compressional dipole reaches the receiver transducer.

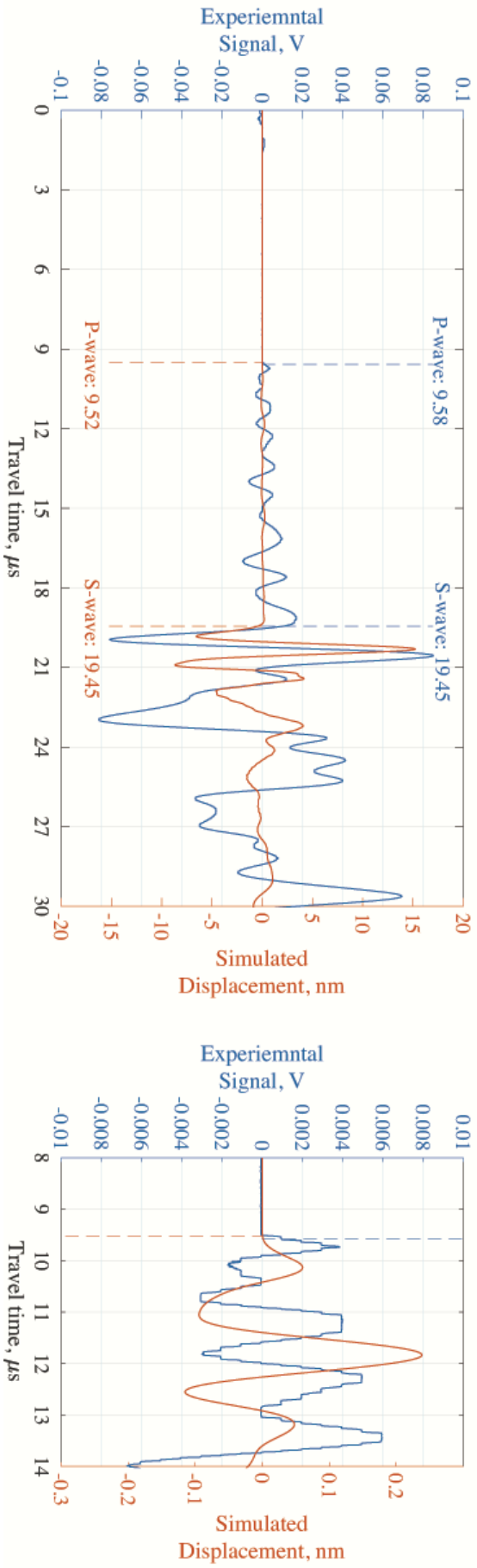


**Figure 7** Experimental (blue) and simulated (red) waveforms of the ultrasonic signal passed through the standard aluminium sample. Primary (V) and secondary (nm) vertical axes are used for experimental and simulated waveforms, respectively. The amplitude of the simulated waveform relates to the average shear displacement of the nodes in the area of the receiver. At the right: magnified section of the waveforms corresponding to the first arrivals.

#### 1.4 Comparison of measurements on thin and standard samples

The velocities measured on standard and thin samples as functions of hydrostatic confining stresses within the range of 2–50 MPa are shown in Figure 8. Solid markers and dots with error bars represent the velocities measured on standard plugs and thin discs, respectively. The measurements are done without pore-pressure control and, consequently, the confining stresses are equal to the effective ones.

The experimental errors are shown only for measurements on thin discs because they are approximately four times higher than the errors of velocities measured on standard plugs. Because the velocities of elastic waves are calculated as  $V = L/T$ , where  $L$  is the length of the sample and  $T$  is the measured traveltimes, the errors of velocity measurements are inversely proportional to the lengths of the samples:

$$\Delta V = \sqrt{\left(\frac{\partial V}{\partial L} \Delta L\right)^2 + \left(\frac{\partial V}{\partial T} \Delta T\right)^2} = \sqrt{\left(\frac{V}{L} \Delta L\right)^2 + \left(\frac{V^2}{L} \Delta T\right)^2} = \frac{V}{L} \sqrt{(\Delta L)^2 + (V \Delta T)^2}, \quad (4)$$

where  $\Delta L$  and  $\Delta T$  are the absolute errors of measurements of length of a sample and traveltimes, respectively. Using a thin 15 mm disc sample instead of a standard one increases the experimental errors fourfold. However, using the systematic approach of automatically picking traveltimes described earlier, I exclude the human factor influence on the experimental errors and enhance the accuracy of the measurements.

As expected, the velocities measured on the PMMA samples show little stress dependency. At the same time, the velocities measured on the Berea and Bentheim sandstones show typical (for sandstones) exponential saturation into a linear trend at low applied pressures (e.g., Christensen and Wang, 1985). This strong stress sensitivity is explained with the closure of cracks and grain contacts with increasing applied pressure (e.g., Walsh, 1965; Shapiro, 2003; Pervukhina *et al.*, 2010). In the Opalinus shale, I measured  $V_P$  and  $V_S$  propagating in the direction of the bedding plane. The S-wave was polarised along the bedding plane. Both  $V_P$  and  $V_S$  slightly increase with the increase of confining stress. Such behaviour is typical for saturated shales (e.g., Dewhurst and Siggins, 2006).

The velocities measured on discs and standard samples match each other within the experimental errors. However, the discrepancies are higher in sandstones, which show the highest stress sensitivity in the sample collection. In the next section,

I simulate stress distribution in the Berea and Bentheim samples to better understand the differences in stress distribution in thin and standard samples.

### 1.5 Numerical modelling of stress distribution

The numerical simulations are fulfilled using Abaqus Finite Element Analysis software (Dassault Systèmes) to understand the influence of the experimental setup and geometry of samples on a stress field and to compare stress distributions inside standard and thin samples. I build two 3D models imitating the experimental setups with standard (Figure 9a) and disc (Figure 9b) samples placed in a Hoek cell between a pair of short and long PEEK pistons, respectively. I numerically apply pressure to the setup in the same way it is done in the experiment: 1) the radial pressure  $P_{radial}$  is applied to a region where the rubber sleeve in a Hoek cell confines the sample and the PEEK pistons ( $S_r$  in Figure 9); 2) the axial pressure  $P_{axial}$  is applied to the top surface of the setups in a region where the jacket of the top transducer is attached to the upper PEEK piston ( $S_a^{top}$  in Figure 9).

As the area on top of the upper PEEK piston, where the axial pressure is applied, differs from the area of the contact between the piston and a sample, the magnitude of axial pressure acting on a sample  $P_{axial}^{sample}$  is not the same as  $P_{axial}$  applied to the top surface  $S_a^{top}$ . The force  $F$  produced by the pressure applied to the upper PEEK piston through the area  $S_a^{top}$  is transmitted to the sample acting on a different area of the base of a cylinder sample  $S_{base}$ :

$$F = P_{axial} S_a^{top} = P_{axial}^{sample} S_{base}. \quad (5)$$

In order to apply a hydrostatic pressure to the sample inside the Hoek cell ( $P_{axial}^{sample} = P_{radial}$ ), the magnitude of the numerically applied axial pressure should correspond to the magnitude of the applied radial pressure as the ratio of the area of the base of a cylinder sample  $S_{base}$  to the area of the surface  $S_a^{top}$ :

$$P_{axial} = \frac{S_{base}}{S_a^{top}} P_{axial}^{sample} = \frac{S_{base}}{S_a^{top}} P_{radial}. \quad (6)$$

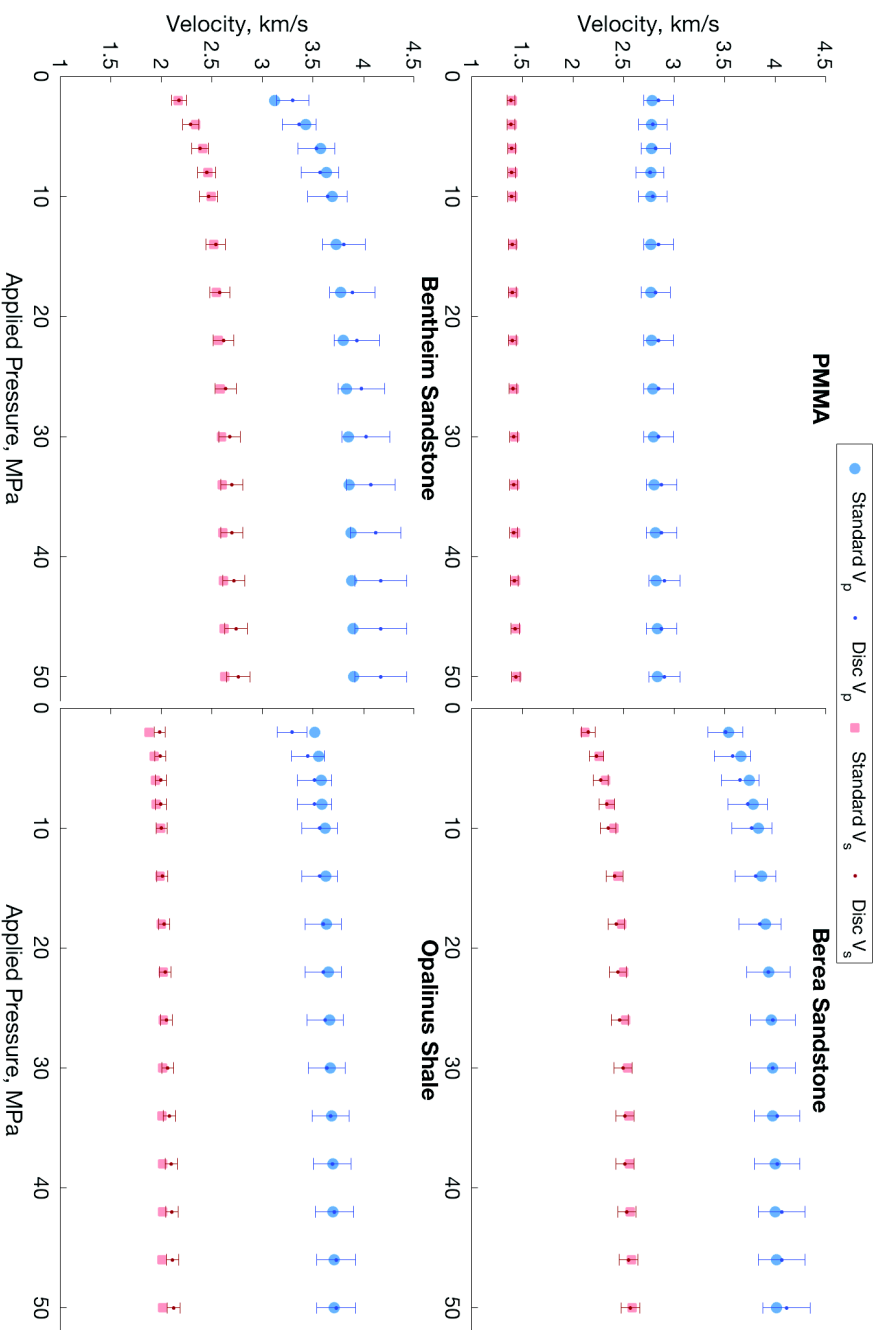


**Figure 8** Measured  $V_p$  and  $V_s$  on the set of standard and thin samples made of four different materials. Experimental errors are shown for measurements on thin samples. Shear velocity  $V_s$  of the Opalinus shale is the velocity of the S-wave propagating and polarised in the bedding plane.

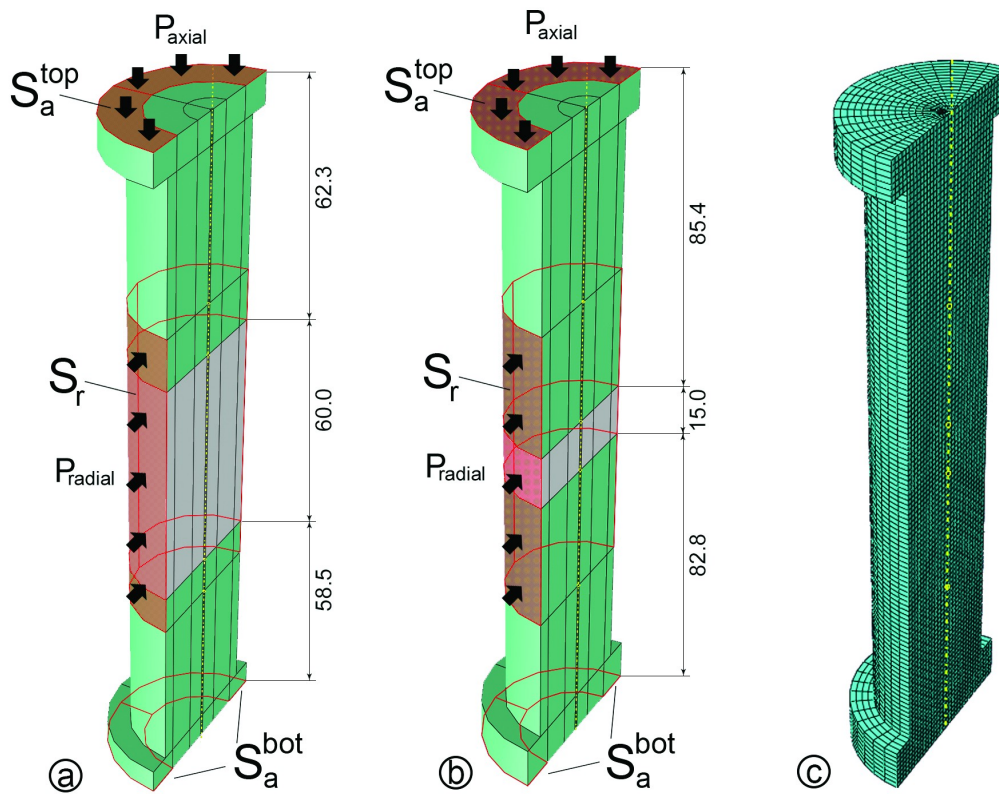


**Figure 9** The Abaqus models built for static stress distribution modelling. The models are full 3D copies of the experimental setups. Figure shows half of the models cut by vertical plane along the main axis. The PEEK pistons are green, the tested samples are grey. The areas with applied boundary conditions are highlighted with red colour.  $S_a^{top}$  is the area, where the axial stress  $P_{axial}$  is applied;  $S_r$  is the area, where the radial stress  $P_{radial}$  is applied;  $S_a^{bot}$  is the fixed area, where the motion of particles in a vertical direction is restricted, simulating a rigid surface underneath the setup. All dimensions are in millimetres. a) The setup with a standard sample. b) The setup with a thin sample. c) Hexahedral meshing of the models.

The nodes of the model at the bottom surface  $S_a^{bot}$  are restricted to move in the vertical direction imitating the contact between the bottom PEEK pistons and the transducer's jacket. The contacts between the PEEK pistons and samples are assumed to be perfect, i.e. there is no slip or friction between these parts.

I use Abaqus Standard solver to analyse the stress field in standard and disc samples within the described geometries. I calculate components of the stress tensor in the spatial cells of the model. Hexahedral cells with  $\sim 1$  mm length in the vertical direction are used (Figure 9c).

I numerically apply hydrostatic pressure in a range of 2–50 MPa to the samples as has been done in the experiment. The stress-dependent elastic properties of the PEEK pistons are taken into account in the model; namely, Young’s modulus  $E$  and Poisson’s ratio  $\nu$  are calculated from the experimentally measured velocities in PEEK (Table 1). Assuming the velocities measured on the standard samples to be the reference data, I derive stress-dependent  $E$  and  $\nu$  of Berea and Bentheim sandstones from experiments on the standard plugs (Table 1) and assign these elastic properties to both standard and thin samples within the numerical models. Generally, the dynamic moduli used for simulation in this work differ from the static moduli. However, here I focus on comparison of stress distribution inside the samples of different geometry; thus, the demonstrated results are valid as long as the same properties are assigned to the tested samples.

**Table 1** Stress-dependent properties of rocks and materials used for modelling.

Pressure, MPa	PEEK long		PEEK short		Berea		Bentheim	
	$E$ , GPa	$\nu$						
2	4.71	0.379	4.70	0.377	23.11	0.222	19.19	0.033
4	4.71	0.379	4.71	0.378	25.63	0.195	22.99	0.062
6	4.72	0.378	4.72	0.378	27.01	0.187	24.91	0.085
8	4.73	0.379	4.72	0.378	27.86	0.177	25.75	0.077
10	4.74	0.379	4.73	0.378	28.63	0.175	26.52	0.080
14	4.76	0.379	4.74	0.379	29.41	0.168	27.10	0.081
18	4.77	0.379	4.75	0.379	30.14	0.163	27.71	0.082
22	4.78	0.380	4.76	0.379	30.60	0.161	28.10	0.080
26	4.79	0.380	4.77	0.380	31.08	0.159	28.56	0.085
30	4.80	0.381	4.78	0.380	31.38	0.155	28.85	0.082
34	4.81	0.381	4.79	0.380	31.52	0.150	28.97	0.083
38	4.82	0.381	4.80	0.381	31.87	0.153	29.22	0.086
42	4.83	0.382	4.81	0.381	31.94	0.150	29.34	0.087
46	4.84	0.382	4.82	0.381	32.19	0.149	29.46	0.088
50	4.85	0.383	4.83	0.382	32.25	0.146	29.61	0.087

The simulated stress distribution inside the setups with standard and thin Berea sandstone samples under isotropic confining stress of 50 MPa is shown in Figure 10, colour-coded by  $p = -1/3 \cdot \text{tr}(\boldsymbol{\sigma})$ , an independent of the coordinate system first invariant of the stress tensor  $\boldsymbol{\sigma}$ , also known as hydrostatic stress. The deviatoric stress can also be useful to provide the full representation of the stress field. However, the purpose of this study is to show whether the reduction of the length of the sample in the experimental setup results in any changes in stress distribution. Therefore, I use the first invariant of the stress tensor, which clearly illustrates the effect of geometry of the experimental setup on the stress field. Figure 10c shows rescaled stress distribution in the thin disc and the standard sample in order to better visualise a detailed stress field inside the samples. One can observe a non-uniform distribution of  $p$  inside the standard and thin samples, which is caused by edge effects; i.e., concentration of stress at the edges, also leading to the well-known barrel shape of a loaded cylindrical sample (Charlez, 1991). The asymmetry of the stress field inside the samples is caused by the geometry of the pistons, which have different sizes in the model as well as in the experiment.

As the elastic waves are initiated and registered by transducers of a certain size mounted at the top and bottom of the setups, I select the central parts of the samples shown in Figure 10c with dashed line for analysis of the stress field. The selected parts have a diameter equal to the size of the transducers. I average the numerically simulated stress magnitude in this volume and calculate the standard deviation.

In the case of the standard sample, high stress areas are located primarily at the top and bottom surfaces of the cylinder near the edges. The central part of the sample is loaded uniformly, as the average stress is equal to 50.65 MPa with standard deviation of 0.86 MPa. The average magnitude of  $p$  at this volume is close to the applied hydrostatic confining pressure of 50 MPa. Hence, the measured ultrasonic velocities are the velocities of the wave propagated throughout the medium uniformly loaded to the applied hydrostatic confining pressure.

In the case of the thin disc sample, the geometry of the setup influences the stress distribution significantly. The stress distribution in the central part of the sample is uniform, but due to the small size of the sample, the edge effects impact the central part, where stress (average stress is 55.39 MPa with standard deviation of 0.27 MPa) is ~11% higher than the applied hydrostatic confining pressure.

Therefore, elastic waves propagating through the thin sample actually travel through a material under higher stress than the pressure applied to the setup. This issue should be taken into account, as the difference in stress distribution between the standard and thin disc samples can result in a discrepancy of the measured velocities, especially in the samples with high stress sensitivity.

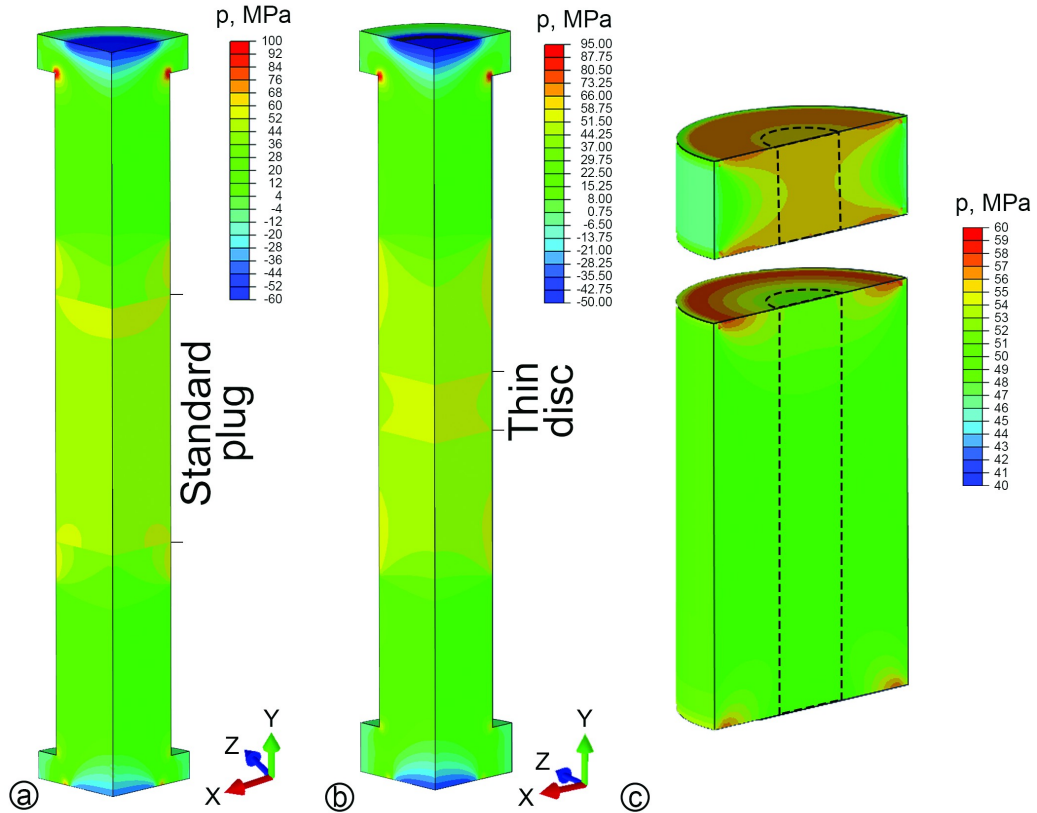


**Figure 10** Modelling of the static stress distribution inside the experimental setups. The applied hydrostatic pressure is equal to 50 MPa. Equivalent pressure stress  $p = -(\sigma_{11} + \sigma_{22} + \sigma_{33}) / 3$  is colour-coded,  $\sigma_{11}$ ,  $\sigma_{22}$ ,  $\sigma_{33}$  are the diagonal components of the stress tensor. a) The setup with a standard Berea sandstone sample. b) The setup with a thin Berea sandstone sample. c) Rescaled stress fields inside the thin and standard samples.

To introduce a relevant correction to the stress-dependent velocities of Berea and Bentheim sandstones measured on thin discs, I calculate the average stress in the central part of the samples at applied pressures in the range 2–50 MPa. Table 2 reports the results of the stress averaging obtained for standard and disc Berea and Bentheim sandstones (as well as for Berea sandstone samples of intermediate sizes, which is discussed below). As mentioned before, the stress distribution along the main axis of the standard samples both for the Berea and Bentheim sandstones is homogeneous and close to the applied pressure, with the relative differences below

1.4% and 0.6% respectively (see Figure 11). The stresses in the middle of the thin disc samples differ from the ones in the standard plugs. The relative difference for the Berea sandstone sample is as high as 11% and it is almost constant for all the applied pressures. In Bentheim sandstone, the relative error increases from 1.5% to 8% when pressure increases from 2 to 50 MPa.

Taking into account the calculated stress distributions, I apply corrections to the experimental data shown in Figure 8. These corrections result in shifting the data points of velocities measured on thin discs along the horizontal axis to the calculated stress values (Figure 12).

The presented results raise several questions: (1) the effect of the discrepancy between applied pressure and stress inside thin samples on measured velocities of elastic waves, (2) the effect of the length of samples on stress distribution, (3) the effect of using different materials in the setups on stress distribution.

**Table 2** The average values of  $p$ , the first invariant of the stress tensor, in the middle parts of Bentheim and Berea sandstone samples of different lengths. Stress values are in MPa. The standard samples are 60 mm long; the thin samples are 15 mm long.

Press ure, MPa	---Bentheim---		-----Berea-----					
	Stan- dard	Thin	Stan- dard	50mm	40mm	30mm	20mm	Thin
2	1.98	2.03	2.02	2.07	2.10	2.13	2.18	2.21
4	3.99	4.20	4.05	4.14	4.20	4.27	4.36	4.43
6	6.01	6.40	6.08	6.21	6.31	6.42	6.55	6.66
8	8.02	8.54	8.11	8.28	8.42	8.56	8.73	8.88
10	10.04	10.72	10.14	10.37	10.53	10.71	10.94	11.12
14	14.06	15.04	14.20	14.51	14.75	15.00	15.31	15.56
18	18.09	19.38	18.26	18.66	18.96	19.29	19.68	20.01
22	22.11	23.70	22.32	22.81	23.18	23.57	24.05	24.47
26	26.15	28.08	26.38	26.96	27.40	27.87	28.44	28.92
30	30.17	32.38	30.43	31.09	31.60	32.13	32.78	33.34
34	34.19	36.71	34.46	35.21	35.78	36.37	37.09	37.73
38	38.23	41.06	38.53	39.38	40.01	40.69	41.50	42.22
42	42.25	45.39	42.57	43.50	44.19	44.93	45.82	46.61
46	46.27	49.71	46.62	47.64	48.40	49.20	50.17	51.02
50	50.29	54.01	50.65	51.75	52.57	53.43	54.46	55.39

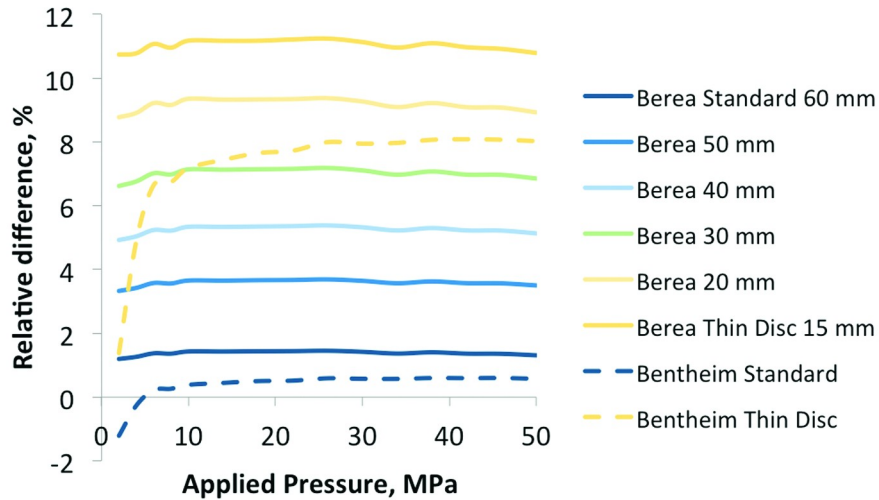


**Figure 11** Relative differences between applied pressure and averaged stress in a central part of the samples, calculated from data reported in **Table 2**.

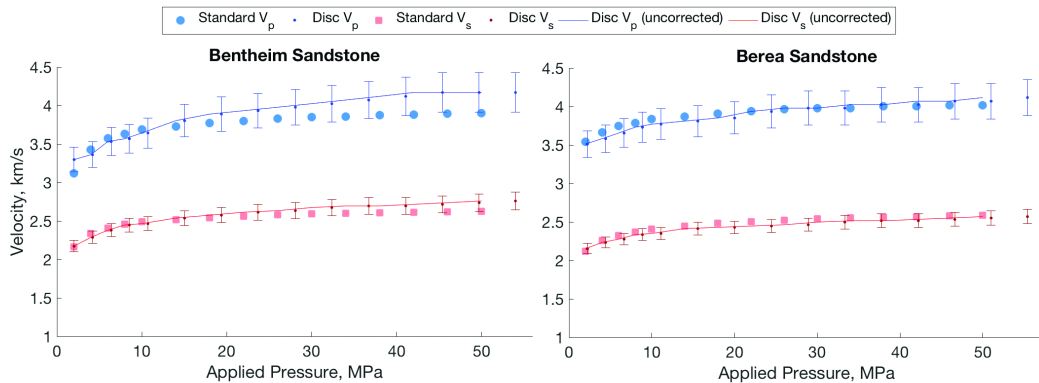


**Figure 12**  $V_p$  and  $V_s$  measured on the standard Berea and Bentheim sandstone samples versus corrected  $V_p$  and  $V_s$  obtained on thin samples. Experimental errors are shown for measurements on thin samples. Solid lines represent velocities measured on thin disc samples before introduced correction.

The data reported in Table 2 show that discrepancy between applied pressure and resultant stress inside a thin disc sample could be significant (for example, up to 11% in Berea sandstone). However, comparison of the results reported in Figure 12 shows that the difference between the initial and corrected data is almost negligible. The difference of 11% between the applied pressure and experienced stress is substantial only at high pressures, where the velocity–stress curve exhibits a linear trend. At pressures lower than 20 MPa, where the stress dependency of velocities is significant, the stress correction in thin samples is small.

However, some rocks exhibit significant stress dependency – like, for instance, Westerly granite and Navajo sandstone from Coyner (1984) and Mavko and

Jizba (1991). Therefore, accurate simulation of the stress distribution is required to interpret the results of ultrasonic measurements under stress and to estimate experimental errors caused by the redistribution of stress in thin samples. The geometry of an experimental setup, and, in particular, the length of the tested samples should be taken into account as a possible source of discrepancy in measured velocities.

In order to understand the effect of the length of samples on stress distribution, I conducted a set of numerical simulations with Berea sandstone samples of different lengths. Figure 13 shows the stress distribution inside the samples with applied hydrostatic confining pressure of 50 MPa. The stress distribution becomes more inhomogeneous with the stronger edge effects on the central part of the sample with the decreasing length of a sample. Table 2 reports the averaged stress inside the central part of samples of different lengths showing an increase in discrepancy between the applied confining stress and gained magnitude of averaged stress with the decrease in sample length (see also Figure 11).

An alternative approach to reducing the discrepancy of the measured elastic properties due to inhomogeneous stress distribution resulting from the edge effect is using a lubricant between the PEEK pistons and the samples. The lubrication reduces friction and allows slip between the parts of the experimental setup, resulting in a more homogeneous stress field inside the samples. However, this approach has a significant drawback: the lubrication of the contacts makes detection of the S-wave using the UPT method challenging due to high attenuation of the S-wave at such contacts.

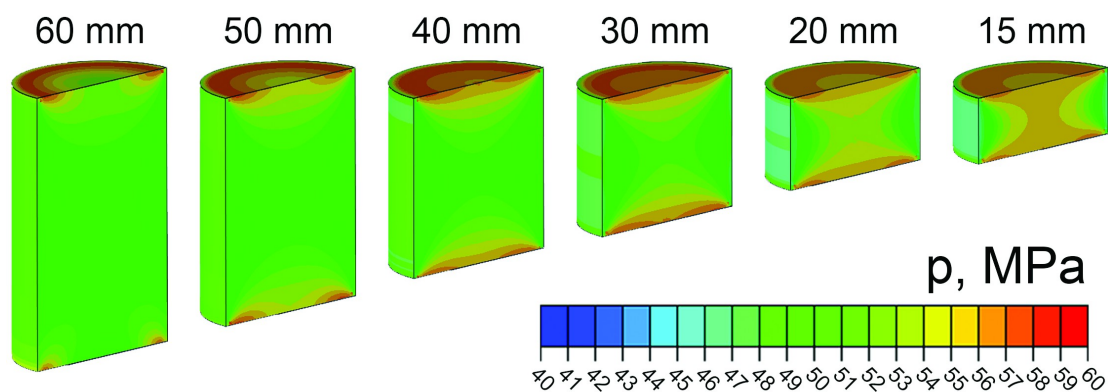


**Figure 13** Results of the numerical modelling of stress redistribution inside Berea sandstone samples of different lengths. Equivalent pressure stress  $p = -(\sigma_{11} + \sigma_{22} + \sigma_{33}) / 3$  is colour-coded;  $\sigma_{11}$ ,  $\sigma_{22}$ ,  $\sigma_{33}$  are diagonal components of the stress tensor.

The material of the pistons used in the experimental setups also affects the stress distribution in the samples. In this work I use pistons made from PEEK, which is a soft material with stress-dependent elastic properties. The stress dependency of its elastic properties introduces complexity into the experimental data processing, as calibration is required for each stress state. This is one of the reasons the pistons in the experimental rigs are traditionally made from aluminium. In order to estimate the influence of aluminium pistons on the stress distribution in the samples, I repeated the numerical modelling described in the previous section, but replaced PEEK pistons with aluminium ones.

The results (Figure 14) show that using materials with a higher contrast in elastic properties than those of a tested sample leads to more inhomogeneous stress distribution. The average stress in the central part of the standard Berea sample is 45.73 MPa, which is significantly lower than an applied pressure of 50 MPa. The stress distribution is also significantly less homogeneous within the sample, which is shown by significant standard deviation of 4.74 MPa. In case of the thin disc of Berea sandstone, the average stress in the central part is 36.05 MPa with standard deviation of 0.99 MPa. Here, the stress field can be considered homogeneous as standard deviation is less than 3% of average stress, however the magnitude of  $p$  in the central area is significantly lower than applied 50 MPa, and the high magnitude stress  $\sim 55$  MPa is concentrated at the lateral surface of the thin sample. The significant inhomogeneity of the stress field inside both standard and thin samples is caused by using aluminium pistons, the elastic properties of which substantially differ from the elastic properties of Berea sandstone. Therefore, the use of aluminium pistons instead of PEEK pistons results in simplification of the calibration routine, but leads to two major drawbacks: 1) high reflection coefficient at the contact between pistons and sample resulting in low energy transmission, and 2) more inhomogeneous stress distribution inside the rock samples, leading to inaccurate measurements of velocities, especially in soft, stress-sensitive samples. Generally, the best option would be to manufacture pistons of a material with elastic properties similar to the tested samples. However, as the results of numerical modelling show, the use of different materials leads to different stress distribution inside the tested samples. Thus, the UPT laboratory experiments should be complemented with numerical modelling to ensure uniform stress distribution in the samples.

Finally, it is worth mentioning that, apart from the reasons discussed above, the discrepancies in measured velocities between the standard samples and the short discs in the natural samples can be caused by inhomogeneity of the samples. When a good-quality core material is available, desiccation/saturation processes are not time-consuming and the ultrasonic measurements are not a part of a comprehensive study that requires measurements on short discs, and the velocities measured on standard samples are more accurate and less affected by the local heterogeneities intrinsic to natural rocks. However, in cases where the ultrasonic measurements must for some reason be fulfilled on thin discs, reliable results can be obtained if the measurements are complemented with numerical simulation of the stress distribution in samples.

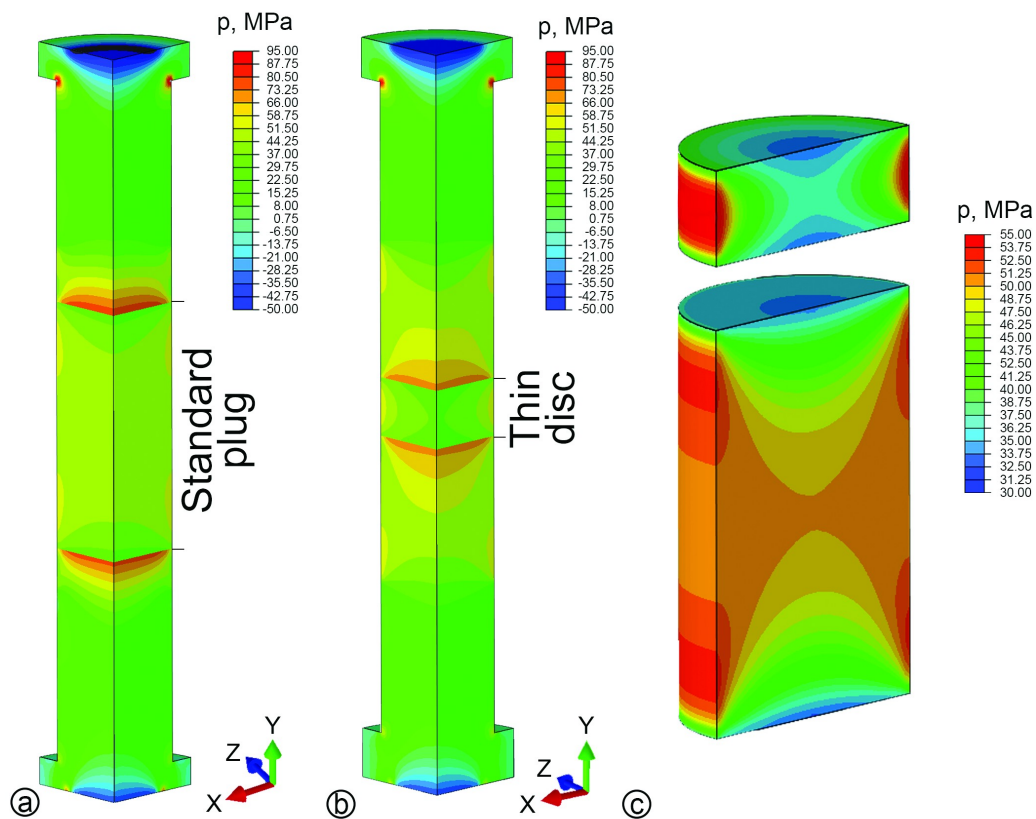


**Figure 14** Modelling of static stress distribution inside the experimental setups with aluminium pistons instead of PEEK parts. The applied hydrostatic pressure is equal to 50 MPa. Equivalent pressure stress  $p = -(\sigma_{11} + \sigma_{22} + \sigma_{33}) / 3$  is colour-coded;  $\sigma_{11}$ ,  $\sigma_{22}$ ,  $\sigma_{33}$  are diagonal components of the stress tensor. a) The setup with a standard Berea sandstone sample. b) The setup with a thin Berea sandstone sample. c) Rescaled stress fields inside the thin and standard samples.

## 1.6 Conclusions

An experimental setup for UPT measurements on thin 15 mm disc samples has been developed, and compressional and shear velocities have been measured on thin and standard samples of PMMA, Opalinus shale, dry Berea and dry Bentheim sandstones. The velocities measured on the thin discs match the velocities measured on the standard samples within the experimental errors. The measurements done under applied hydrostatic confining pressures in a range 2–50 MPa show that reliable stress dependencies of the velocities can be obtained on the thin disc samples as well as on the standard plugs.

At the same time, numerical modelling shows that the stress distributions in the standard samples and thin discs are different and the average stress in the thin samples between the ultrasonic transducers might deviate significantly from the applied confining pressure. This fact can affect the measured ultrasonic velocities, especially in soft, stress-sensitive samples. I have demonstrated that, for example, in the thin Berea sandstone sample, the stress inside the central part of the sample along the propagation of elastic waves is 11% higher than the applied confining pressure. In this case the velocities measured at the applied pressure actually correspond and have to be attributed to higher values of stress. The actual stress distribution within the samples depends on the length of the sample, its elastic properties, and the elastic properties of the pistons used in the experimental setup. When aluminium pistons are used, the relative difference between the applied confining pressure and the actual stress in the sample can be significant even for samples of the standard length. Therefore, the inhomogeneity of the stress field is a critical issue that has to be taken into account during UPT measurements on rock samples. The measured velocities can be attributed to the correct stress, and reliable stress dependencies can be obtained on the thin discs as well as on the standard samples if experimental measurements are combined with a numerical simulation of the stress field in a given experimental setup.

The results presented in Chapter 1 are an important milestone in this research. The developed workflow of the UPT measurements is used in the following chapters of this work for correct measurements of velocities made on thin shale samples. The use of thin samples is unavoidable when the effects of varying saturation on elastic properties of shales is studied because the saturation or drying of shale is an

extremely time-consuming process due to the low permeability and small pore size of this rock. The use of thin samples instead of standard plugs significantly reduces the duration of experiments.

## Chapter 2. Experimental study of the effects of varying hydration on the elastic properties of shales\*

### 2.1 Introduction

The hydromechanical behaviour of shales is extensively studied nowadays because this type of rock is often involved in many challenging applications such as the geological storage of nuclear waste, CO<sub>2</sub> sequestration, and the production of both conventional and unconventional hydrocarbons. The exploitation of shale formations that seal oil or gas reservoirs or form unconventional reservoirs can induce variations in the rock hydration, leading to changes in microstructure and elastic properties (e.g. Vales *et al.* 2004; Ferrari *et al.* 2014). The exploration and monitoring of shaly formations with seismic methods and interpretation of log data require an understanding of how changes in the hydration state affect the microstructure and elastic moduli of shales.

Shales usually contain clay, which is often responsible for structural changes with a varying hydration state. This effect of water on shales and clayey soils has been studied by a number of authors. For instance, Vales *et al.* (2004) examined the mechanical behaviour of Tournemire shale with drying and observed significant shrinkage of the samples (strain  $\sim 10^{-3}$ ). The authors also reported that variations in hydration in clay-containing rocks led to substantial modification of the pore space. Montes *et al.* (2004) used an environmental scanning electron microscope and showed that the hydration/dehydration of Callovo-Oxfordian argillites resulted in complex cracking, particle aggregation/desegregation, and the opening/closing of pores. Ferrari *et al.* (2014) reported a decrease in porosity with drying in shales from the Opalinus Clay formation and Brown Dogger formation. The decrease in porosity with drying was also shown on the Callovo-Oxfordian claystone (Gasc-Barbier and Tessier, 2007; Wan *et al.*, 2013; Menaceur *et al.*, 2016) and clayey soils (Romero *et al.*, 2011; Salager *et al.*, 2013). Another insight into the structural changes of clays

---

\* This chapter is an extended version of the paper Yurikov, A., M. Lebedev, M. Pervukhina, and B. Gurevich, 2018, Water retention effects on elastic properties of Opalinus shale: Geophysical Prospecting, Special Issue, doi: 10.1111/1365-2478.12673

subjected to varying hydration was gained with the use of mercury intrusion porosimetry (Romero *et al.*, 2011; Lima *et al.*, 2012). Romero *et al.* (2011) showed two types of porosity in clays: (1) macroporosity with characteristic pore size of  $\sim 10 \mu\text{m}$  constituting inter-aggregate pores and (2) microporosity with pore size of  $\sim 10 \text{ nm}$  constituting intra-aggregate pores, that is, contacts between clay platelets. The hydration of clays led to the closing of macropores and an increase in micropore space. All these studies show that variations in hydration result in significant structural changes in rocks containing clays. Namely, drying leads to a shrinkage of samples, desegregation of clay particles (often with the opening of inter-aggregate pores) and a reduction of total pore volume due to the closing of micropores.

These structural changes resulting from changes in hydration state must influence the elastic properties of shales. Shales are almost always strongly anisotropic. In many cases, they can be considered transversely isotropic media with their elastic properties determined by five independent elastic constants (e.g. Jones and Wang, 1981; Hornby *et al.*, 1994; Mavko *et al.*, 2009). These elastic constants are usually calculated from compressional (P) and shear (S) wave velocities measured along the directions normal, parallel and at  $45^\circ$  to the bedding plane (e.g. Vernik and Nur, 1992). The elastic moduli of shales have been measured at different hydration states (Ghorbani *et al.*, 2009; Vales *et al.*, 2004; Wild *et al.*, 2015; Szewczyk *et al.*, 2018). Vales *et al.* (2004) reported that the drying of Tournemire shale resulted in a decrease in ultrasonic P-wave velocity propagating perpendicular to the bedding plane,  $V_P(0^\circ)$ , and had no effect on the velocity of a P-wave propagating along the bedding,  $V_P(90^\circ)$ . Wild *et al.* (2015) reported similar P-wave velocity trends measured on Opalinus Clay samples. Szewczyk *et al.* (2018) examined Mancos and Pierre shales and observed a decrease in both  $V_P(0^\circ)$  and  $V_P(90^\circ)$  with dehydration. In contrast, Ghorbani *et al.* (2009) reported an increase in the P-wave velocity with drying in samples from Callovo-Oxfordian argillite formations. Moreover, they observed that S-wave velocities strongly depend on hydration state, exhibiting increasing trends with dehydration. Ghorbani *et al.* (2009) stated that changing the hydration state influences the textural structure of the clay matrix resulting in the consolidation and hardening of clay particles with drying.

Analysis of these studies suggests that the experimental observations of the effects of varying hydration on the elastic properties of shales are sparse and contradictory. The reasons for changes in elastic moduli with variations in hydration

are not fully understood. In this chapter, I extend the existing experimental data with the analysis of structural changes and measurements of the elastic properties of Opalinus shale at different hydration states. The measurements of elastic properties are conducted under varying hydrostatic confining pressure in a range from 2 to 50 MPa; hence, the stress dependency of the moduli is obtained. I observe a swelling of the shale with increasing hydration and a decrease in the total porosity with drying. Measured dependencies of ultrasonic P- and S-wave velocities on hydration are broadly similar to those reported by Ghorbani *et al.* (2009), except  $V_P(0^\circ)$ , which exhibits a decreasing trend with drying, similar to the results of Vales *et al.* (2004), Wild *et al.* (2015) and Szewczyk *et al.* (2018). This seeming discrepancy in the results obtained on different samples implies that variations in the elastic properties of shales with changing hydration states are driven by multiple competing phenomena. The experimental results reported in this chapter form a basis for further theoretical analysis of the effect of changing hydration on the microstructure and elastic properties of shales.

## 2.2 Experimental method

### 2.2.1 Studied samples

For this research, I select Opalinus shale, a well-known rock used for many experimental studies (e.g., Soe *et al.*, 2009; Monfared *et al.*, 2014; Minardi *et al.*, 2016). It contains ~80% of clay matrix with porosity of 10%–20%, which is mostly constituted by pores smaller than 1  $\mu\text{m}$  (Houben, 2013). The mineralogy of samples used for this work is determined by X-ray diffraction analysis as 16% kaolinite, 42% illite–smectite, 10% illite/mica, 4% chlorite, 14% quartz, 9% calcite, 1% pyrite, 1% siderite, 1% albite/anorthite, 1% anatase, <1% dolomite/ankerite and <1% rutile. The scanning electron microscope (SEM) image (Figure 15) shows the microstructure of Opalinus shale.

In this study, I use three sets of samples cut from the same core without the use of cooling/lubricating water in order to preserve the initial hydration state. The first set comprises one cylindrical sample of 5 mm in length and 3 mm in diameter. This sample is prepared for analysis of structural changes with the use of high-resolution X-ray micro-computed tomography ( $\mu\text{CT}$ ). The second set comprises three cylindrical samples with bulk volume  $\sim 15 \text{ cm}^3$  each. These samples are used to

estimate bulk and grain densities, porosity, mass fraction of water and saturation of the preserved shale. The third set contains two disc-shaped (~15 mm in length, 38 mm in diameter) samples cut normal and parallel to the bedding plane of the shale. These disc samples are used for ultrasonic measurements of P- and S-wave velocities at different hydration states. The third set also contains additional sister samples for characterisation of structural changes with varying hydration.

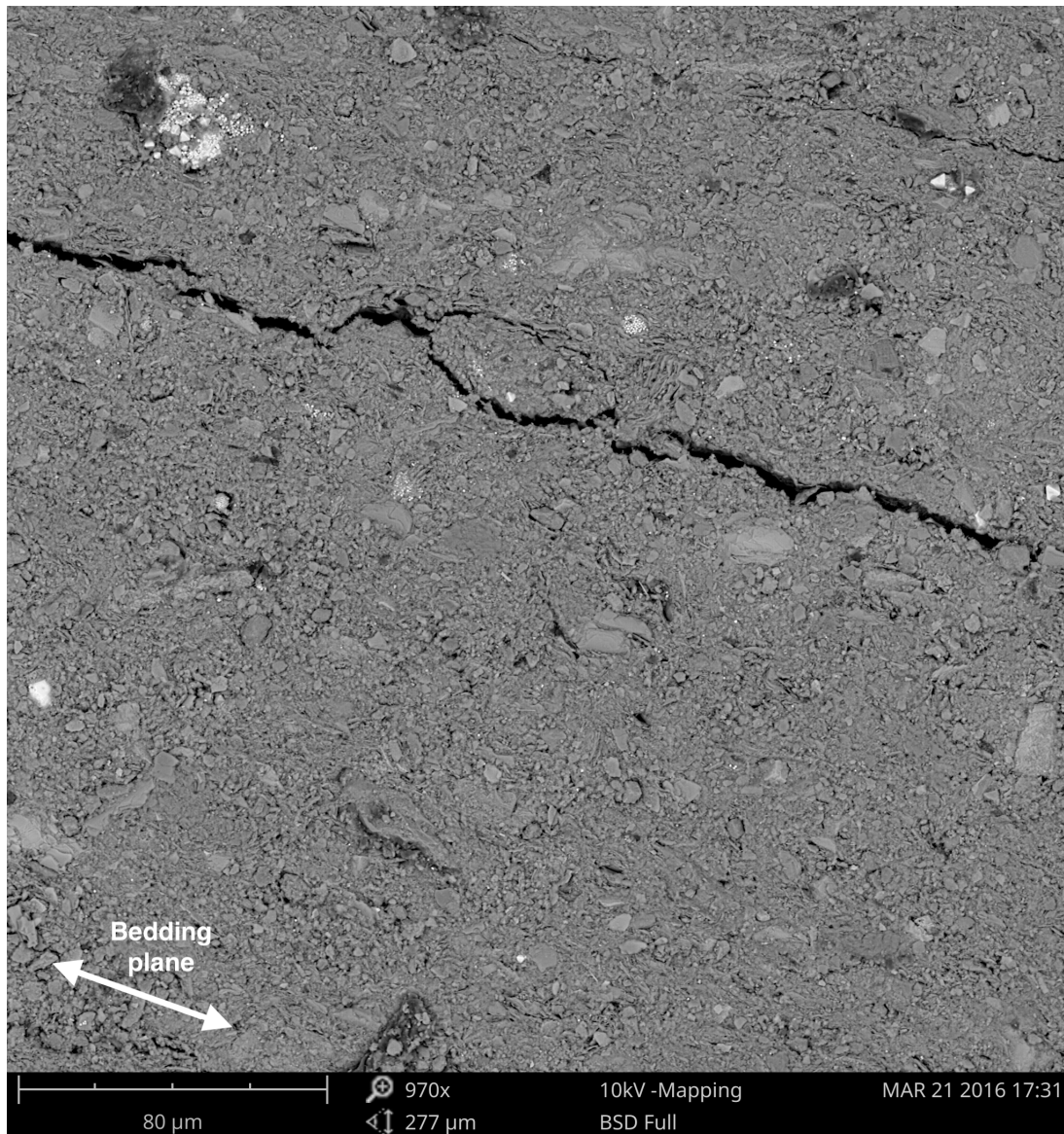


**Figure 15** Scanning electron microscope (SEM) image of the Opalinus shale. Black colour shows pores and fractures, dark grey denotes clay matrix, light grey and white colours show silt inclusions like quartz (light-grey) and calcite (white). The white arrows indicate the bedding plane.

### 2.2.2 Hydration procedure

I control the hydration state of the samples by changing the relative humidity (RH) of the surrounding atmosphere (e.g., Greenspan, 1977). The samples are kept inside enclosed glass chambers, so-called desiccators, with a presence of saline solutes at ambient temperature. The type of salt and the temperature define the RH inside the desiccators. Variations in RH induce adsorption or desorption of water in pores, thus drying or hydrating the samples. Equilibration of sorption processes can take from hours to months depending on the type of rock (e.g., Ferrari *et al.*, 2014; Pimienta *et al.*, 2014).

In this work, I test the Opalinus shale at five different hydration states. Starting with a preserved state, the samples from the third set are sequentially placed in desiccators with 52%, 31%, 13% and 97% RH (Figure 16). I continuously monitor the mass of the samples during the experiment to ensure stabilisation of the sorption processes when the RH is changed. For the tested disc samples, stabilisation of the mass (and, hence, sorption) takes up to three weeks.

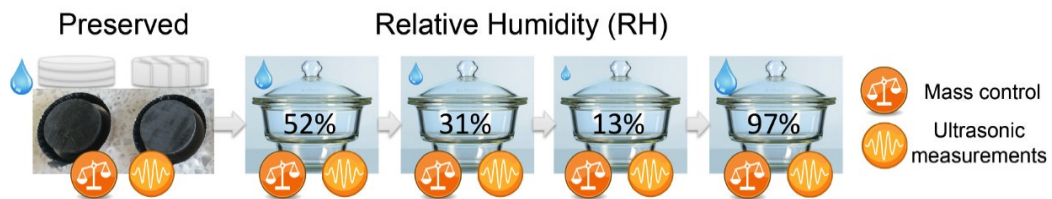


**Figure 16** The schematic of the drying/rehydration experiment. The desiccators are labelled with RH maintained inside. Continuous mass control is performed. Ultrasonic measurements are done after equilibration of sorption processes.

### 2.2.3 Characterisation of structural changes

First, I characterise the structural changes caused by variations in hydration state using  $\mu$ CT image analysis. The small cylindrical sample from the first set is scanned at two hydration states: dry and wet. The sample is glued to a vertical stainless steel rod attached to the supporting base (Figure 17). The assembly is first maintained in the desiccator with 13% RH to dry the sample. Then the scanning is done with the 3D X-ray Microscope VersaXRM 500 with X-ray energy of 60 keV, acquiring 5001 radiographic images. The total scanning time is eight hours. To maintain the sample at the same humidity during scanning, the assembly is covered by an enclosed plastic tube transparent for X-rays, and the solute ensuring 13% RH

is placed inside (Figure 17). Scanning is repeated after rehydration of the sample in the atmosphere with 97% RH, which is then sustained during scanning. The sample is firmly attached to a rod, which ensures that the same part of the sample is scanned each time. The radiographic images are reconstructed into 3D volumes with the internal Zeiss-XRada software. The raw datasets comprise  $988 \times 1012 \times 990$  voxels with a resolution of  $0.98 \mu\text{m}$ . Then, the 3D volumes are subjected to image analysis done with Avizo Fire 9.3 (FEI Thermo Fisher Scientific). First, I apply the 3D non-local mean filter to reduce noise and remove imaging artefacts. Then, contrasts of dry and wet datasets are matched and overlapping sub-volumes of  $600 \times 600 \times 600$  voxels are cropped. Finally, I use the watershed algorithm (Beucher and Lantuéjoul, 1979; Beucher and Meyer, 1993) to separate visible pores from the mineral matrix and collect statistics of pore shapes and sizes for both datasets. I analyse the obtained images and statistics to identify microstructural changes during transition of the shale from a dry to a wet state.

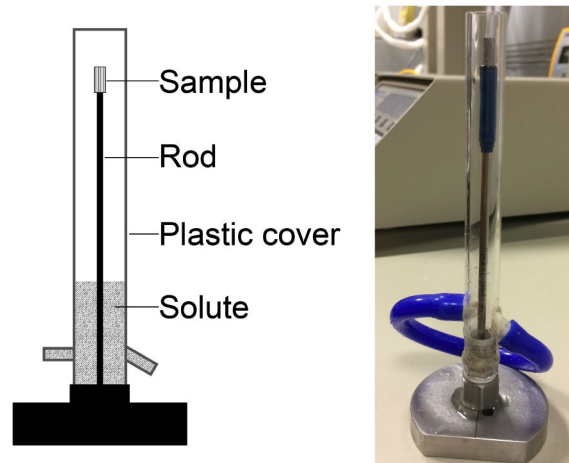


**Figure 17** The sample for micro computed tomography ( $\mu\text{CT}$ ) inside a mini-desiccator constructed to keep RH constant during scanning: schematic (left) and photo (right).

Second, I estimate the bulk density ( $\rho$ ), mass fraction of water ( $\omega$ ), porosity ( $\phi$ ) and the saturation ( $s$ ) of the rock at each hydration state. I start with the characterisation of the shale in the preserved state using the cylindrical samples from the second set. The samples are crushed into powder, weighed and dried in a vacuum chamber at  $105^\circ\text{C}$  to evaporate all removable water. Then the dry powders are weighed again to determine the mass of evaporated water, and a gas pycnometer is used to measure the volumes of the dry powders. From the measured masses and volumes of the dry powders I obtain the average grain density of the Opalinus

samples,  $\rho_{gr} = 2.66 \text{ g/cm}^3$ . The average water mass fraction in the preserved state is determined as

$$\omega = \left\langle \frac{m_{pr} - m_{dry}}{m_{pr}} \right\rangle, \quad (7)$$

where  $m_{pr}$  is the mass of a powder before drying,  $m_{dry}$  is the mass of a dried powder and brackets mean averaging.

Estimation of the mass fraction of water  $\omega$  at other hydration states (at 52%, 31%, 13% and 97% RH) is done using continuous monitoring of the mass of the samples from the third set. If the masses of a sample at the previous ( $m_{i-1}$ ) and current ( $m_i$ ) hydration states are known, and the water mass fraction in the previous hydration state ( $\omega_{i-1}$ ) is estimated, then one can recursively obtain the current water mass fraction:

$$\omega_i = 1 - \frac{m_{i-1}}{m_i} (1 - \omega_{i-1}). \quad (8)$$

The bulk density  $\rho$  of the samples is experimentally measured using the sister samples from the third set, which have undergone the same hydration path as the two primary disc samples. I weigh the duplicates immersed in oil, which does not penetrate into the shale due to high oil viscosity, low permeability and small pore size. Then  $\rho$  is calculated using the equation

$$\rho = \rho_{oil} \left(1 - \frac{W}{mg}\right)^{-1}, \quad (9)$$

where  $m$  is the mass of the sister sample,  $W$  is the weight of the same sample immersed in oil,  $\rho_{oil}$  is the density of oil and  $g$  is the gravitational acceleration.

The measured grain density, bulk density and water mass fraction are used to estimate the porosity and saturation of the samples at each hydration state:

$$\phi = 1 - \frac{\rho}{\rho_{gr}} (1 - \omega), \quad (10)$$

$$s = \frac{\rho_{gr} \phi^{-1} - 1}{\rho_w \omega^{-1} - 1}, \quad (11)$$

where  $\rho_w = 1.03 \text{ g/cm}^3$  is the density of the saturating water.

#### 2.2.4 Measurements of elastic properties

I measure ultrasonic P- and S-wave velocities in the disc samples at five hydration states (Preserved, 52%, 31%, 13% and 97% RH). A detailed description of the measurement technique can be found in Chapter 1 of this thesis. In this study, the measurements are done on two disc-shaped samples cut perpendicular and parallel to

the bedding plane of the shale. The ultrasonic waves propagate along the axes of rotation of the discs. When the measurements are conducted on a horizontally cut sample, the S-wave is polarised in the bedding plane. Thus, using the notation of Mavko *et al.* (2009), I measure  $V_P(90^\circ)$ ,  $V_{SH}(90^\circ)$  on the horizontally cut sample and  $V_P(0^\circ)$ ,  $V_{SV}(0^\circ)$  on the vertically cut sample. Assuming vertical transverse isotropy (VTI) of the Opalinus shale, I calculate components of the stiffness tensor as follows:

$$C_{11} = \rho V_P^2(90^\circ); C_{33} = \rho V_P^2(0^\circ); C_{44} = \rho V_{SV}^2(0^\circ); C_{66} = \rho V_{SH}^2(90^\circ). \quad (12)$$

The fifth independent modulus  $C_{13}$  is derived from the velocity of a P-wave propagating at  $45^\circ$  to the bedding plane of the sample. In this work, the  $C_{13}$  was not measured due to a lack of core material for preparation of a sample of the required disc shape.

Additionally, during the measurements, the samples are subjected to hydrostatic confining pressure varying from 2 to 50 MPa. Therefore, I obtain stress dependencies of the moduli in relation to the hydration state, which are used to analyse structural features.

## 2.3 Results

### 2.3.1 Structural changes with varying hydration state

Figure 18 shows two  $\mu$ CT images of the same part of the sample in a dry (13% RH) and wet (97% RH) state. The difference between the two images is subtle. No cracks or fractures induced by the change in hydration state can be seen. Yet, I observe an expansion of the sample with the transition from a dry to a wet state. I analyse the distance between the most prominent features on the scans, such as dense grains of quartz or calcite. This analysis shows that the size of the sample in the direction perpendicular to the bedding plane increases by an average of 1.8%, while there is no significant change of size along the bedding plane (the average increase is 0.2%). This indicates that hydration of the sample leads to swelling primarily in the direction perpendicular to the bedding plane.

Analysis of the pore space performed using the  $\mu$ CT 3D volumes shows that the segmented porosity visible on the scans is 0.55% for the dry sample and 0.57% for the wet sample. Because of the scanning resolution of  $0.98 \mu\text{m}$ , I am not able to analyse micropores  $<1 \mu\text{m}$ , which are known to constitute the majority of the total

porosity of the Opalinus shale (Houben, 2013). The shape and number of visible pores do not change much with varying hydration (Figure 19). Therefore, the macroporosity, visible on the scans, barely changes with the varying hydration state. This indicates that the observed swelling of the sample results from the expanding of micropores.

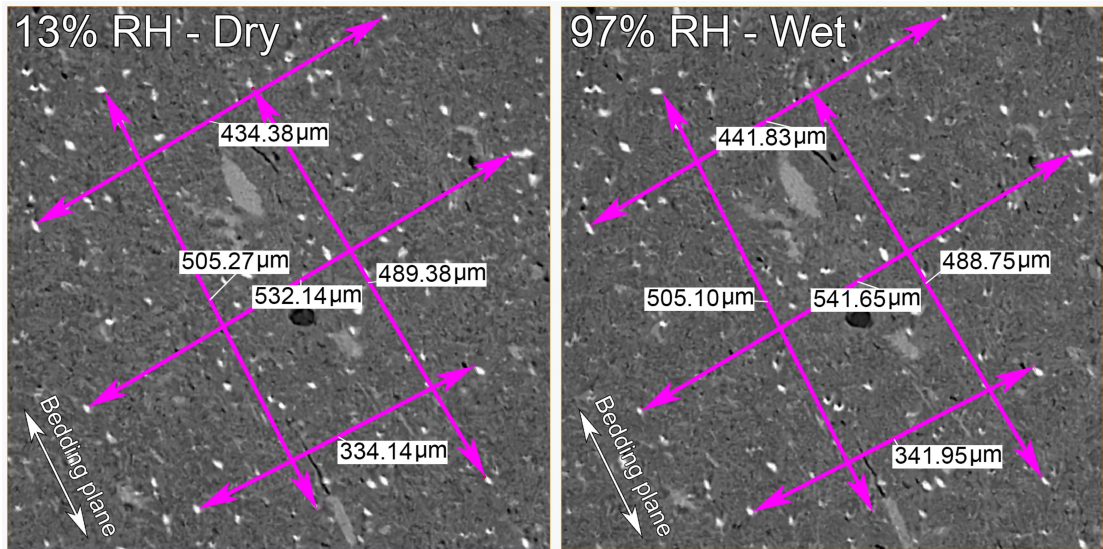


**Figure 18** Micro computed tomography ( $\mu$ CT) images of the same area of the Opalinus shale sample at dry state obtained in the atmosphere with 13% relative humidity (RH) (left) and wet state after 97% RH atmosphere (right). The images show 2D slices of the 3D volume cut perpendicular to the bedding plane (indicated by white arrows). The pink arrows indicate the distance between pairs of the most prominent features on the scans, such as dense grains of quartz or calcite. These features are clearly visible on the images as white spots. Thus it is convenient to use them as markers for the measurement of the distance.

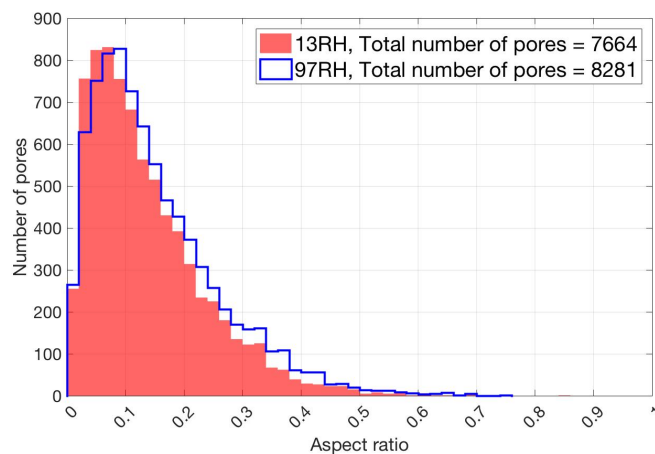


**Figure 19** Histograms showing distribution of pores by their shape. The pores are approximated with oblate ellipsoids. The aspect ratio is the ratio of the shortest to the longest axes of ellipsoids.

The estimated porosity of the preserved samples is 13.6%, which agrees with previously reported data for Opalinus shale (e.g., Soe *et al.*, 2009). I observe that dehydration of the samples leads to a decrease in the total porosity to 11.8% at the driest state at 13% RH. Again, similar decreasing porosity trends were reported for clay-containing rocks in earlier studies (Gasc-Barbier and Tessier, 2007; Romero *et al.*, 2011; Salager *et al.*, 2013; Wan *et al.*, 2013; Ferrari *et al.*, 2014).

Rehydration of the samples at the last experimental stage leads to swelling, an increase of  $\omega$  up to 6.5% and an increase of  $\phi$  up to 15%. The bulk density of the samples increased up to 2.42 g/cm<sup>3</sup> with rehydration. Unexpectedly, this value is smaller than the bulk density of the shale at the preserved state with less water content. This effect is a result of swelling of the shale at high RH, which dominates over water adsorption.

I also estimate the saturation of the samples using equation 11 and give the results in Table 3. Saturation, which is the volume of water over the volume of pores, is not measured directly. It depends on the measured grain density, mass fraction of water and porosity. Therefore, the error of estimation of saturation is high due to indirect measurements. Hence, I prefer to present the results of the experimental measurements of elastic properties in relation to  $\omega$ , which is measured from the mass change monitoring with higher accuracy. Moreover, using saturation as an indicator of the hydration state of samples may be misleading because the sorption of water is coupled with pore space deformations, which are two competing factors that have the opposite effect on saturation. Nevertheless, the reader can find saturation related to a particular RH or  $\omega$  in Table 3.

**Table 3** Characterisation of Opalinus shale at different hydration states. The table reports the mass fraction of water  $\omega$ , density  $\rho$ , porosity  $\phi$  and the saturation  $s$ .

Hydration state	$\omega$ , %	$\rho$ , g/cm <sup>3</sup>	$\phi$ , %	$s$ , %
Preserved	5.5 ± 0.4	2.44 ± 0.03	13.6 ± 2.5	95 ± 18
52% RH	2.5 ± 1.1	2.38 ± 0.01	13.1 ± 1.9	44 ± 22
31% RH	1.3 ± 0.7	2.37 ± 0.01	12.2 ± 1.7	24 ± 15
13% RH	0.3 ± 0.8	2.36 ± 0.01	11.8 ± 1.7	5 ± 15
97% RH	6.5 ± 2.0	2.42 ± 0.01	15.0 ± 2.4	100 ± 39

### 2.3.2 Variation of elastic properties with varying hydration state

The measured elastic properties of the Opalinus samples in terms of stiffness constants are shown in Figure 20 versus mass fraction of water indicating the hydration state. Colour coding represents the hydrostatic confining pressure applied to the samples.

The shear moduli  $C_{44}$  and  $C_{66}$  exhibit a gradual increase with dehydration. The behaviour of  $C_{11}$  and  $C_{33}$  differs from that of the shear moduli.  $C_{11}$  remains nearly constant until the last desiccation stage, when it shows a significant increase, while  $C_{33}$  shows a drastic decrease after the first desiccation stage and remains almost constant afterwards. The subsequent rehydration of the samples in the 97% RH atmosphere leads to significant changes in the elastic constants:  $C_{11}$ ,  $C_{44}$  and  $C_{66}$  decrease and become smaller than those in the preserved state, while  $C_{33}$  increases after dehydration without reaching the initial values corresponding to the preserved state.

Additionally, Figure 20 shows Thomsen's (1986) anisotropy parameters

$$\varepsilon = \frac{C_{11} - C_{33}}{2C_{33}}; \gamma = \frac{C_{66} - C_{44}}{2C_{44}}. \quad (13)$$

The parameter  $\varepsilon$  consistently rises with drying as  $C_{11}$  increases and  $C_{33}$  decreases. This indicates higher P-wave anisotropy in the dry shale with the anisotropy parameter in a range from 1 to 1.4 depending on the applied pressure. Rehydration of the samples leads to a decrease of  $\varepsilon$  back to the value exhibited at the initial preserved state. The parameter  $\gamma$  shows different dependency on the hydration state, decreasing in the first two drying stages and slightly increasing in the driest state. Rehydration leads to recovery of  $\gamma$  up to the value in a range from 0.85 to 0.93 depending on the applied stress. Unlike the P-wave anisotropy, the S-wave anisotropy is higher for wet shale. However, the variation of  $\gamma$  is smaller than that of  $\varepsilon$  as  $C_{44}$  and  $C_{66}$  exhibit similar dependencies on hydration.

The stress sensitivities of the stiffness constants and the anisotropy parameters are also shown in Figure 20 with colour coding. Higher confining stress applied to the samples results in lower anisotropy of both P- and S-waves. The elastic constants of the shale are stress-dependent as well. In order to analyse the stress dependency of the elastic moduli at different hydration states, I plot the variation in the moduli against the applied pressure with the colour-coded hydration

state (Figure 21). The variations in the moduli are normalised to the value at the maximum applied stress of 50 MPa:

$$\Delta C_{ij} = \frac{C_{ij} - C_{ij}|_{50 \text{ MPa}}}{C_{ij}|_{50 \text{ MPa}}} \quad (14)$$

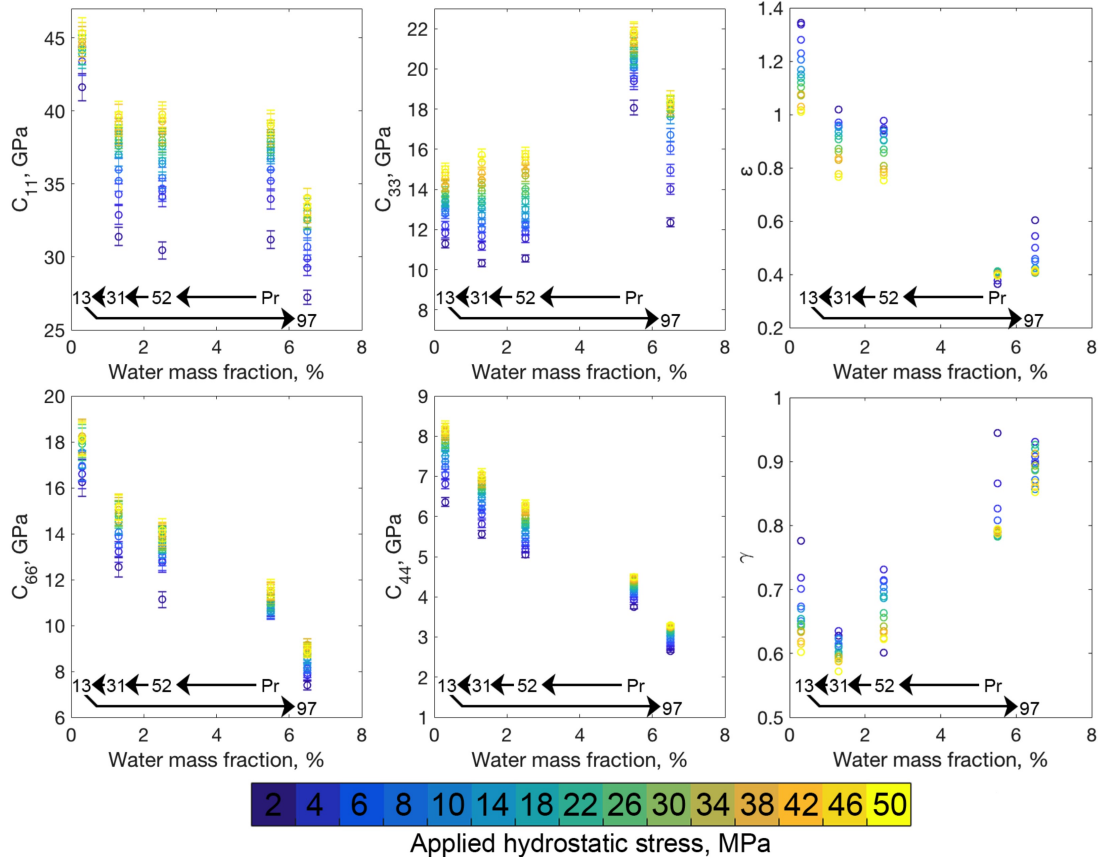


**Figure 20** The components of elastic stiffness tensor and Thomsen's (1986) anisotropy parameters measured in the Opalinus shale samples at different hydration states. Labels under the data points indicate the relative humidity (RH) corresponding to each hydration state (Pr indicates a shale in preserved state). The black arrows show the scheme of desiccation. The applied hydrostatic confining pressure is colour coded.

The shear modulus  $C_{44}$  exhibits similar dependencies on applied stress in all hydration states. The stress dependencies of  $C_{66}$  are also close to each other, but show some discrepancy at low confining pressures. The stress sensitivity of  $C_{11}$  is not influenced by variations in hydration either, except for the driest state ( $\omega = 0.3\%$ , RH = 13%), when the relative change of the modulus reaches only 8% compared to  $\sim 20\%$  in the other states. In contrast, the stress sensitivity of  $C_{33}$  is strongly affected by hydration: the magnitude and rate of the relative change differs depending on the hydration state. Generally, the stress sensitivity of elastic moduli indicates that the rock contains compliant pores, usually characterised by small aspect ratios (e.g.,

Walsh, 1965; Dewhurst and Siggins, 2006; Pervukhina *et al.*, 2009). In shales, the compliant porosity comprises 1) macrofractures, 2) contacts between the clay matrix and silt inclusions (e.g., Beloborodov *et al.*, 2016) and 3) contacts between clay particles (e.g., Sayers, 1999). Further, I investigate the influence of varying hydration on compliant porosity in Opalinus shale using experimentally measured stress sensitivities.

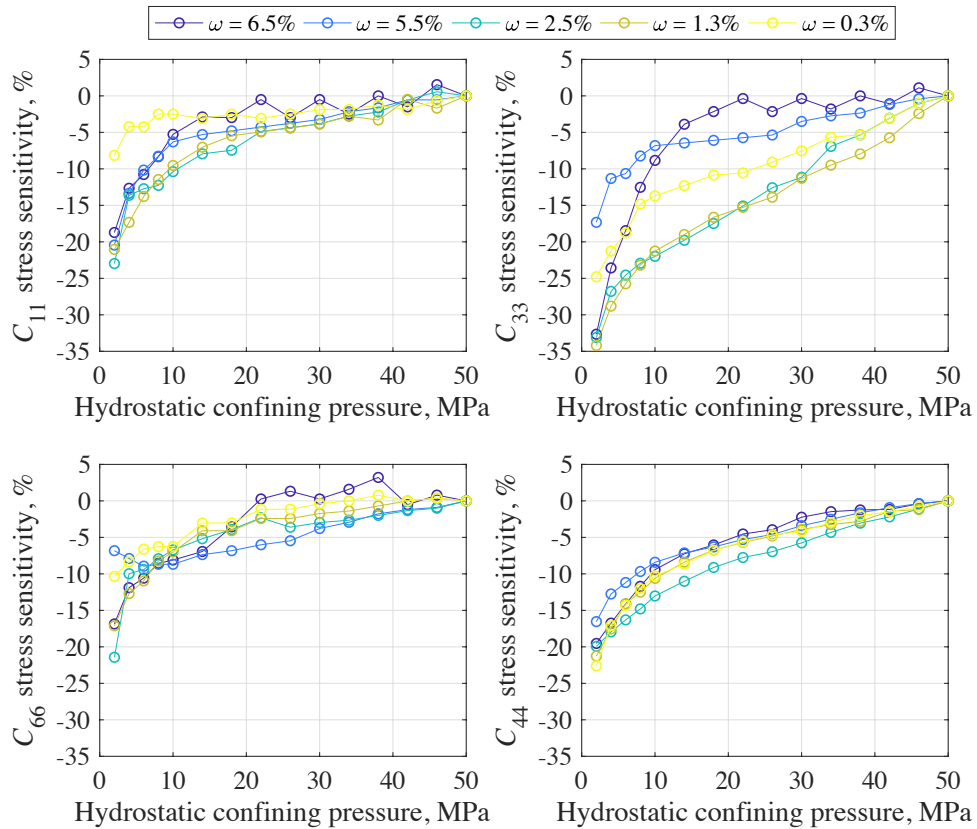


**Figure 21** Variations in the elastic moduli of the Opalinus shale samples at different hydration states normalised to the moduli values at the maximum applied pressure of 50 MPa. The water mass fraction is colour coded.

## 2.4 Conclusions

I have experimentally investigated the effect of drying/rehydration on the microstructure and elastic properties of Opalinus shale. Analysis of microtomographic images shows that the shale sample swells with saturation in the direction perpendicular to the bedding plane with no visible damage to the rock. The macroporosity (pore size >1 μm) constitutes less than 5% of the total porosity of the Opalinus shale and remains almost unchanged in different hydration states. The microporosity (the remaining part of the total porosity) varies with drying and

rehydration. The total porosity reduces with drying and increases with rehydration. The observed microstructural changes in the shale are broadly consistent with previous observations. The question as to whether any irreversible microstructural changes occur in shales with variation in hydration state is yet to be answered. The experimental results obtained in this work show no evidence of such changes. However, a new experimental study of the microstructure and elastic properties of shale done with several drying/rehydration cycles would further clarify the issue.

The variation in elastic properties of the Opalinus shale with changing hydration has been studied using ultrasonic velocity measurements at confining hydrostatic stress varying from 2 to 50 MPa applied to the samples. The observed stress dependency of the elastic moduli indicates the presence of compliant porosity in the shale samples. The compliant porosity in shales may be comprised of macrofractures, contacts between the clay matrix and silt inclusions, and contacts between clay particles. Variation of water content may significantly affect the stiffness of the compliant porosity, and hence the elastic properties of the rock. In the following chapter (Chapter 3), I perform quantitative analysis of the obtained experimental data in order to improve understanding of the effect of changing water saturation on the elastic properties of compliant pores in the shale.

I have measured four independent stiffness moduli ( $C_{11}$ ,  $C_{33}$ ,  $C_{44}$  and  $C_{66}$ ) of the shale at different hydration states. The fifth independent modulus,  $C_{13}$ , was not measured due to a lack of rock material for preparation of the sample of the required shape. The measured moduli show the following dependencies of the elastic properties on hydration. The S-wave moduli  $C_{44}$  and  $C_{66}$  continuously increase with drying up to values  $\sim 1.5$  times higher than in the initial preserved state. The in-plane P-wave modulus  $C_{11}$  remains constant with drying until the last drying stage, when significant increase of the modulus is observed. The cross-plane P-wave modulus  $C_{33}$  shows the opposite trend, decreasing after the first drying stage and remaining constant afterwards. The rehydration of the samples leads to a decrease of  $C_{11}$ ,  $C_{44}$  and  $C_{66}$  to values lower than in the preserved state. The  $C_{33}$ , on the contrary, increases with rehydration, but does not recover to the initial value exhibited at the preserved state. These dependencies of the elastic moduli on hydration are broadly similar to the results reported by Ghorbani *et al.* (2009) for Callovo-Oxfordian argillite formations, except  $C_{33}$ , which exhibits a decreasing trend with drying. Similar decreasing trends of  $C_{33}$  were reported for Tournemire shale by Vales *et al.*

(2004), for Opalinus Clay samples by Wild *et al.* (2015), and for Mancos and Pierre shales by Szewczyk *et al.* (2018).

The reported experimental results raise the following questions. 1) What is the reason for the observed discrepancies in the behaviour of elastic moduli in different shales? 2) Why do the compressional moduli  $C_{11}$  and  $C_{33}$  exhibit the opposite response to the changes in hydration? 3) What is the driving mechanism of a significant hardening of the shear elastic moduli in Opalinus shale with drying? Although the driving factors of the observed phenomena are not fully understood, the discrepancies in the experimental data measured on different shales imply that variations in the elastic properties of shales with changing hydration are driven by multiple competing phenomena. In Chapter 3, I perform qualitative and quantitative analysis of the obtained experimental data in order to highlight driving mechanisms of the effect of changes in hydration on the elastic properties of shales and to improve understanding of the phenomenon.

## Chapter 3. Theoretical study of the dependency of the elastic properties of shales on hydration\*

### 3.1 Introduction

The experimental results presented in Chapter 2 show that structural changes observed in Opalinus shale with drying/rehydration are characterised by shrinkage/swelling of the samples in the direction normal to the bedding plane and reduction/increase of the total porosity. The analysis also showed that changes in the total porosity are due to variations in the volume of micropores (pore size  $<1 \mu\text{m}$ ). These results are qualitatively consistent with data previously reported for other clay-containing rocks.

In contrast, I have found that there is no agreement between elastic moduli behaviour with variations in hydration reported for different shales (Vales *et al.*, 2004; Wild *et al.*, 2005; Ghorbani *et al.*, 2009; Szewczyk *et al.*, 2018; and this study). Table 4 summarises changes in the measured ultrasonic velocities with dehydration reported in these works. First, the discrepancy in the behaviour of P-wave velocities is yet to be explained. Second, conventional rock physics theories (e.g., Gassmann, 1951; Brown and Korringa, 1975; Smith *et al.*, 2003) state that changing saturation should not affect the shear moduli of rocks. However, the measurements reported in Ghorbani *et al.* (2009) and in this research show that both  $V_{SV}(0^\circ)$  and  $V_{SH}(90^\circ)$ , and the corresponding shear moduli, significantly increase with the dehydration of clay-containing rocks.

Therefore, in this chapter, I speculate about the possible reasons for the observed phenomena. I highlight four driving factors that could be responsible for the behaviour of the elastic properties in shales: 1) variations of the total porosity; 2) substitution of pore-filling fluid; 3) change of stiffness of contacts between clay particles; and 4) chemical hardening/softening of clay particles. I investigate the role of each factor with qualitative and quantitative evaluation of the experimental data

---

\* This chapter is an extended version of the paper Yurikov, A., M. Lebedev, M. Pervukhina, and B. Gurevich, 2018, Water retention effects on elastic properties of Opalinus shale: Geophysical Prospecting, Special Issue, 1–13, doi: 10.1111/1365-2478.12673

reported in the previous chapter and show that some of them might have an opposite effect.

**Table 4** Comparison of the experimentally measured behaviour of ultrasonic P- and S-wave velocities with dehydration in different clay-containing rocks. **Inc** indicates increase of the velocity; **Dec** indicates decrease of the velocity; **NoE** indicates no effect of changing hydration on the velocity. **N/A** means that measurements were not conducted.

<b>Data from</b>	<b>Rock</b>	$V_P(0^\circ)$	$V_P(90^\circ)$	$V_{SV}(0^\circ)$	$V_{SH}(90^\circ)$
Vales <i>et al.</i> (2004)	Tournemire shale	<b>Dec</b>	<b>NoE</b>	N/A	N/A
Wild <i>et al.</i> (2005)	Opalinus clay	<b>Dec</b>	<b>NoE</b>	N/A	N/A
Ghorbani <i>et al.</i> (2009)	Callovo-Oxfordian argillite	<b>Inc</b>	<b>Inc</b>	<b>Inc</b>	<b>Inc</b>
Szewczyk <i>et al.</i> (2018)	Mancos shale; Pierre shale	<b>Dec</b>	<b>Dec</b>	<b>Inc</b>	<b>Inc</b>
This research	Opalinus shale	<b>Dec</b>	<b>Inc</b>	<b>Inc</b>	<b>Inc</b>

### 3.2 The role of variation in the total porosity

Total porosity reduction with the drying of clay-containing rocks has been reported in earlier studies (e.g., Montes *et al.*, 2004; Gasc-Barbier and Tessier, 2007; Romero *et al.*, 2011; Ferrari *et al.*, 2014). The same effect was observed in this study (Table 3). The effect of a change in porosity on the elastic properties of a composite material (consisting of several phases, such as pores and grains) can be estimated using different methods. These methods include relatively simple bound estimations (e.g., Hashin and Shtrikman, 1963), and more complex effective medium models that require some knowledge about the geometry of the pore space (e.g., Nishizawa, 1982; Hornby *et al.*, 1994). Regardless of the model, reduction of the porosity as a stand-alone process leads to an increase in the stiffness of the rock.

I quantify the effect of a change in porosity on the elastic moduli using the differential effective medium (DEM) model (Nishizawa, 1982). This model assumes that pores have an oblate ellipsoidal shape characterised by the aspect ratio  $\alpha$ . This is a reasonable assumption for vertical transverse isotropy (VTI) shales with a dominant orientation of particles and pores in the bedding plane. The same DEM

model can be used to quantify the effect of fluid substitution on the elastic properties. I discuss the results of this quantitative analysis in the next subsection, where I combine the pore reduction and fluid substitution effects.

### 3.3 The fluid substitution effect

When the relative humidity (RH) changes, the adsorption or desorption of water in the samples results in a variation in saturation. Regardless of pore space transformation, pore-filling water is substituted by air in a process of drying and, vice versa, water fills the pores with hydration of the samples. Again, the effect of decreasing saturation, as a stand-alone process, on the elastic properties of porous rocks has been thoroughly studied (e.g., Brown and Korrington, 1975; Domenico, 1976). In the case of VTI medium, a decrease in saturation in a porous rock leads to a decrease of the P-wave moduli  $C_{11}$  and  $C_{33}$ , while the S-wave moduli  $C_{44}$  and  $C_{66}$  remain unchanged.

In order to quantify the effect of fluid substitution on the moduli of the Opalinus shale, I use the aforementioned DEM model. In this model, I combine the varying saturation effect with variations in the total porosity. For the modelling, I use the experimental data measured at hydrostatic confining pressure of 2 MPa. The properties of the samples at the preserved state are used as the initial point for the modelling. Then, using the estimations of the porosity and the saturation from Table 3, I predict the change of the elastic moduli with drying. The model accounts for the changing volume fraction of pores and the elastic properties of the pore-filling fluid, which is a mix of water and air. The elastic properties of such a water–air mix are calculated using the Wood equation (e.g., Mavko *et al.*, 2009):

$$K_{mix}^{-1} = sK_w^{-1} + (1 - s)K_{air}^{-1}, \quad (15)$$

where  $K_{mix}$  is the bulk modulus of the water–air mix,  $K_w = 2.2$  GPa is the bulk modulus of water,  $K_{air} = 0.1$  GPa is the bulk modulus of air and  $s$  is the estimated saturation.

The DEM model requires information about the aspect ratio of pores  $\alpha$ . Because of the small pore size in the shale and insufficient resolution of the micro-computed tomography ( $\mu$ CT) scans, the aspect ratio was not estimated directly. Additionally, the  $C_{13}$  modulus was not measured in the experiments, but it can be expressed through Thomsen's (1986) anisotropy parameter  $\delta$  and the measured moduli. Therefore, the model has two fitting parameters:  $\alpha$  and  $\delta$ . The anisotropy

parameter  $\delta$  is subjected to a set of physical constraints (e.g., Berryman *et al.*, 1999; Tsvankin, 2001; Spikes, 2014). In the preserved Opalinus shale, the upper bound is  $\delta = 0.36$ . I first run the model with  $\alpha$  varying from 0.1 to 1 and  $\delta = 0.35$ . Additionally, in order to estimate the sensitivity of the model to the parameter  $\delta$ , I run the model with  $\alpha = 0.1$  setting  $\delta = 0.20$  and  $\delta = 0.05$ .

The workflow of the modelling is shown in Figure 22. At the first step, I perform the inversion of the elastic moduli of the shale matrix. I exclude the effect of the porosity saturated with the water–air mix from the elastic moduli of the Opalinus shale in the initial preserved state. This is done using an inversion of the DEM scheme by minimising the functional

$$F = \|\mathbf{C}^{DEM}(\mathbf{C}^{matrix}, \mathbf{C}^{fluid}, \phi, \alpha) - \mathbf{C}^{exp}\|_{L_2}, \quad (16)$$

where  $\mathbf{C}^{matrix}$  is the target stiffness tensor of the shale matrix,  $\mathbf{C}^{fluid}$  is the stiffness tensor of the water–air mix calculated using equation 15,  $\phi$  is the total porosity, and  $\alpha$  is the aspect ratio of pores.  $\mathbf{C}^{DEM}$  denotes the stiffness tensor of the effective medium calculated using the DEM scheme from the aforementioned parameters.  $\mathbf{C}^{exp}$  is the experimentally measured stiffness tensor of the shale. Therefore, the equation 16 defines the  $L_2$ -norm of the difference between the forward modelling of the effective medium and the experimental data. The second step is the forward DEM modelling of the elastic properties of the effective media representing the shale in three hydration states (13%, 31% and 52% RH). I use the derived  $\mathbf{C}^{matrix}$  (see Appendices) and add the porosity saturated with the water–air mix corresponding to the given hydration state (see Table 3). The intermediate hydration states shown by the modelling curves are obtained using the interpolation of experimental data ( $\omega$ ,  $\phi$  and  $s$ ).

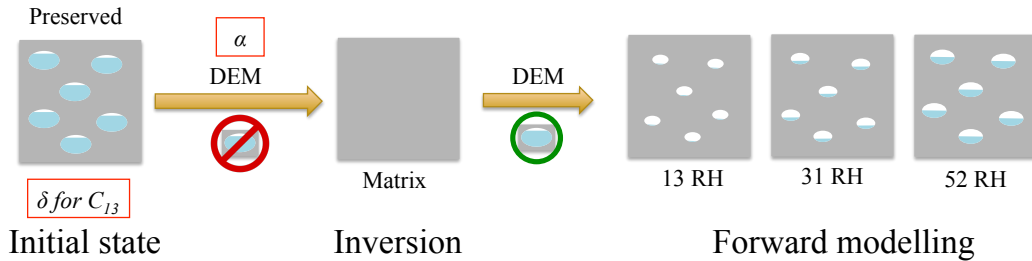


**Figure 22** The scheme of the modelling of the effect of changing porosity and fluid substitution on the elastic properties of Opalinus shale in different hydration states. The model has two fitting parameters  $\alpha$  and  $\delta$ .

The elastic properties versus water mass fraction  $\omega$  predicted by the model are shown in Figure 23, colour coded by the used aspect ratio. The values of  $\delta$  used for the modelling with  $\alpha = 0.1$  are shown by labels next to the corresponding curves at the figure. The elastic moduli are sensitive to the variations of  $\alpha$ , while the parameter  $\delta$  has no effect on the shear moduli, but influences  $C_{11}$  and  $C_{33}$ . As discussed earlier, reduction in porosity and the substitution of water with air have the opposite effects on the compressional moduli, which explains the concave shape of the prediction curves. These two factors combined might be able to explain the P-wave moduli variation observed in the experiment. However, the S-wave moduli are affected only by a reduction in the porosity. The increase of  $C_{44}$  and  $C_{66}$  by a factor of 1.5 with drying from the preserved to the driest state cannot be explained by the measured reduction in porosity of about 2% (from 13.6% to 11.8%). Such stiffening of the S-wave moduli with drying has to be explained by other factors.

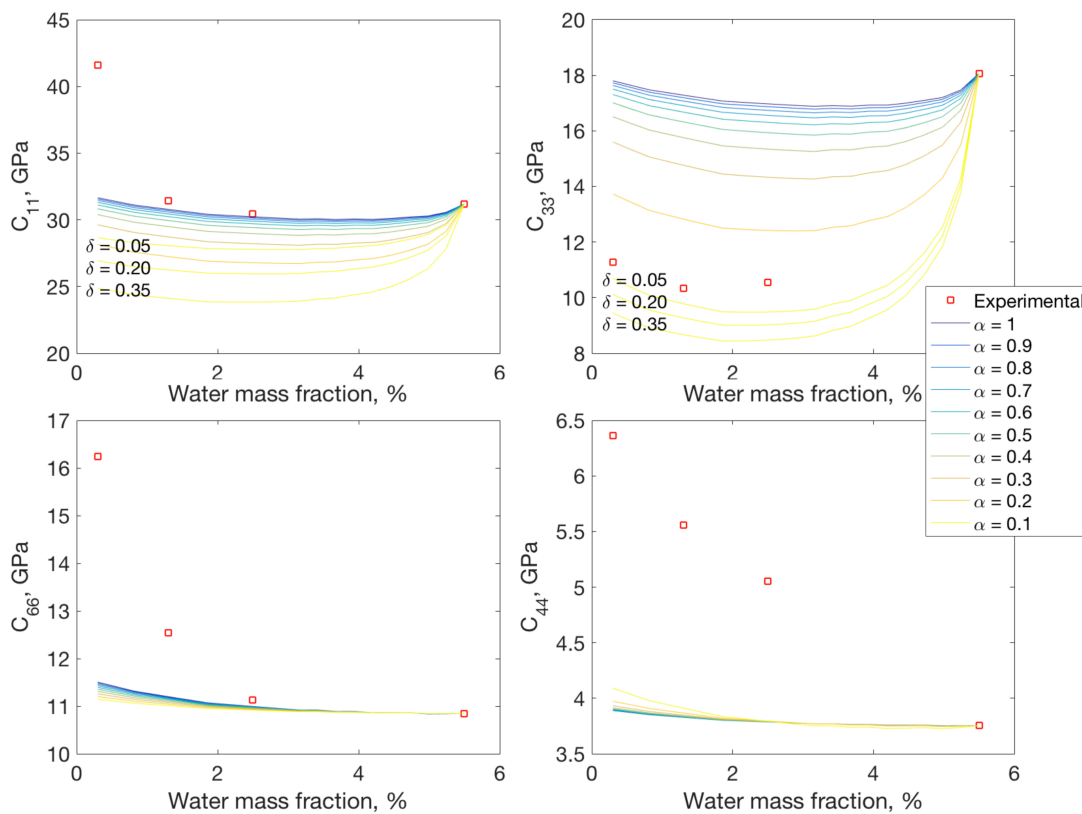


**Figure 23** Differential effective medium (DEM) modelling of drying-induced variations of the elastic properties caused by reduction of the total porosity and fluid substitution. Square red markers show the experimentally measured moduli at hydrostatic confining pressure of 2 MPa. The initial point for modelling is the moduli of the shale in the preserved state. The aspect ratio of pores is colour coded. The labels next to the modelling curves show used anisotropy parameter  $\delta$ . No label means  $\delta = 0.35$ .

### 3.4 Change of stiffness of contacts between clay particles

The factor that could be responsible for the significant increase in the S-wave moduli in the shale subjected to drying is increasing stiffness of contacts between clay particles. For example, Osipov *et al.* (2004) reported that there is a water film that lubricates the contacts between clay particles in shales. Drying of shales leads to thinning of the water film and, hence, to a stiffening of clay aggregates. I assume that the contacts between clay particles form part of the compliant porosity of shales. Further components of the compliant porosity are macrofractures and contacts between the clay matrix and silt inclusions. The presence of compliant porosity in the Opalinus shale is indicated by the measured stress dependencies of the elastic moduli (Shapiro, 2003; Shapiro and Kaselow, 2005; Ciz and Shapiro, 2009).

The behaviour of compliant porosity with changing hydration can be analysed using the experimental stress dependencies of the elastic moduli obtained at different hydration states (Figure 21). To this end, I use the parameterisation of elastic stress sensitivity in shales proposed by Pervukhina *et al.* (2011). This model simulates the response of the VTI rock containing compliant pores (discontinuities) to the applied pressure. Following Shapiro and Kaselow (2005), the model assumes that the surface area of compliant pores decreases with applied pressure exponentially:

$$A = A_0 \exp(-P/P_c), \quad (17)$$

where  $A$  is the specific surface area of an individual discontinuity,  $A_0$  is the specific surface area of an individual discontinuity at zero pressure,  $P$  is the effective pressure, and  $P_c$  is a characteristic discontinuity closing pressure. Therefore, a specific surface area of all discontinuities per unit volume is expressed as

$$s(P) = N_0 A = N_0 A_0 \exp(-P/P_c), \quad (18)$$

where  $N_0$  is the total number of discontinuities integrated over the volume.

The discontinuities are assumed to be oriented anisotropically with the probability density for a particular orientation expressed as

$$W(\theta, \varphi) = \frac{1 + \eta \cos^2 \theta}{\int_0^{2\pi} \int_0^\pi (1 + \eta \cos^2 \theta) \sin \theta \, d\theta \, d\varphi} = \frac{1 + \eta \cos^2 \theta}{4\pi(1 + \eta/3)}, \quad (19)$$

where  $\theta$  is an angle between the vertical axis and the normal to the surface of a compliant pore,  $\varphi$  is an angle of rotation about the vertical axis, and  $\eta$  is the

orientation anisotropy parameter. The value of  $\eta = 0$  corresponds to isotropic distribution, and large values of  $\eta$  indicate strong alignment of discontinuities.

When a compressive isotropic pressure is applied to the rock with such a distribution of discontinuities, the density of discontinuities along a certain plane is assumed to reduce exponentially with the normal pressure traction acting on that plane. If the orientation of discontinuities is anisotropic, their area will reduce differently in different directions. I model the effect of such variations in area of discontinuities on the elastic properties of the rock using the noninteractive approximation of Sayers and Kachanov (1995):

$$\Delta S_{ijkl} \equiv S_{ijkl} - S_{ijkl}^0 = \frac{1}{4} (\delta_{ik}\alpha_{jl} + \delta_{il}\alpha_{jk} + \delta_{jk}\alpha_{il} + \delta_{jl}\alpha_{ik}) + \beta_{ijkl}, \quad (20)$$

$$\alpha_{ij} = \frac{1}{V} \sum_r B_T^{(r)} n_i^{(r)} n_j^{(r)} A^{(r)}, \quad (21)$$

$$\beta_{ijkl} = \frac{1}{V} \sum_r (B_N^{(r)} - B_T^{(r)}) n_i^{(r)} n_j^{(r)} n_k^{(r)} n_l^{(r)} A^{(r)}, \quad (22)$$

where  $S_{ijkl}$  is an element of the compliance tensor, which can be derived by inverting the stiffness constants:

$$S = C^{-1}, \quad (23)$$

where  $S$  and  $C$  are the  $6 \times 6$  compliance and stiffness matrices in the Voigt notation (e.g., Mavko *et al.*, 2009).  $\Delta S_{ijkl}$  is the excess compliance caused by the presence of compliant pores,  $S_{ijkl}^0$  are compliances of the rock at high pressures, when all soft discontinuities are closed,  $\delta_{ij}$  is the Kronecker delta,  $r$  is the number of planar discontinuities with surface area  $A^{(r)}$ , and  $n_i^{(r)}$  is the  $i$ th component of the unit vector normal to the surface of the  $r$ th discontinuity in volume  $V$ . The elastic properties of discontinuities are parameterised by  $B_T^{(r)}$  and  $B_N^{(r)}$ , the tangential and normal compliances per unit of a specific surface area. The model operates with the effective properties of the discontinuities, thus I assume that all compliant pores have the same surface area and specific tangential and normal compliances. Therefore, the index ( $r$ ) in  $B_T$  and  $B_N$  is further omitted. Another assumption of the model is that  $B_T$  and  $B_N$  are independent of the orientation of discontinuities and do not change with pressure.

Substituting equations 18–19 into equations 20–22 gives the expressions for variation of compliances with applied pressure in VTI media:

$$\Delta S_{11} \equiv S_{11} - S_{11}^0 = \frac{s_n B_T \exp(-P/P_c)}{105} (14 + 4\eta + 21B + 3B\eta), \quad (24)$$

$$\Delta S_{33} \equiv S_{33} - S_{33}^0 = \frac{s_n B_T \exp(-P/P_c)}{105} (14 + 6\eta + 21B + 15B\eta), \quad (25)$$

$$\Delta S_{44} \equiv S_{44} - S_{44}^0 = \frac{s_n B_T \exp(-P/P_c)}{105} (42 + 16\eta + 28B + 12B\eta), \quad (26)$$

$$\Delta S_{66} \equiv S_{66} - S_{66}^0 = \frac{s_n B_T \exp(-P/P_c)}{105} (42 + 10\eta + 28B + 4B\eta), \quad (27)$$

$$\Delta S_{13} \equiv S_{13} - S_{13}^0 = \frac{s_n B_T \exp(-P/P_c)}{105} (-7 - 3\eta + 7B + 3B\eta), \quad (28)$$

Here,  $B = B_N/B_T$  and  $s_n = s_0 / [4\pi(1 + \eta/3)]$ , where  $s_0 = N_0 A_0$  is the specific surface area of discontinuities per unit volume. Therefore, the model uses four parameters ( $P_c$ ,  $\eta$ ,  $B_T$  and  $B$ ) to fit the experimental data Figure 20 represented in the form of compliance tensor, which is obtained from the stiffness tensor. Because the  $C_{13}$  modulus was not measured during the experiment, a simple elliptical model of TI medium was used to obtain all the components of the compliance tensor (Helbig, 1983).

The fitting of the experimental results with the parameterisation model of Pervukhina *et al.* (2011) is shown in Figure 24. The parameters of the model are reported in Table 5. One can see a close fit of the experimental data with low misfits between the measured elastic properties and the fitting curves. The derived parameters of the model provide information about compliant porosity in the Opalinus shale at different hydration states. First, the derived values of  $\eta \sim 10^5$  indicate that the compliant porosity in the Opalinus shale is strongly aligned. This results from the microstructure of the shale comprising clay aggregates aligned in the bedding plane. Second, the characteristic closing pressure  $P_c$  is  $\sim 13$  MPa for all hydration states except the one corresponding to 52% RH, where  $P_c = 17.7$  MPa. This parameter corresponds to the value of the applied hydrostatic pressure under which the stress dependencies of the elastic moduli reach the linear trend (Figure 21). Third, the ratio of normal to tangential compliance  $B$  increases with drying, which is in good agreement with the results reported for other shales (e.g. Sayers, 1999; Pervukhina *et al.*, 2011). Finally, the tangential compliance of discontinuities  $s_0 B_T$  decreases with drying of the shale. Such behaviour indicates that with drying, discontinuities become less compliant (stiffer) in the tangential direction. This means that the compliant porosity (including contacts between clay particles, contacts between clay and silt, and macrofractures) becomes stiffer and can result in the observed increase of S-wave stiffness moduli with dehydration of the shale.

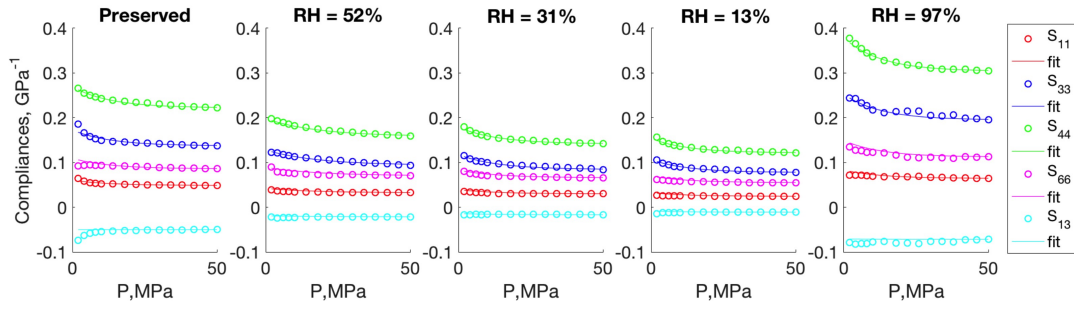


**Figure 24** The experimentally measured compliances (circles) and the results of the fitting (lines) using the model of Pervukhina *et al.* (2011) for Opalinus shale at different hydration states (shown by labels at the top).

**Table 5** Parameters of the model of Pervukhina *et al.* (2011) used to fit the obtained pressure-dependent elastic properties of the Opalinus shale at different hydration states.

Hydration state	$\omega$ , %	Misfits, $\text{GPa}^{-1}$	$P_c$ , MPa	$\eta$	$s_0 B T_5$ , $\text{GPa}^{-1}$	$B$
Preserved	5.5	$17.2 \times 10^{-4}$	13.0	$0.89 \times 10^5$	0.74	1.00
52% RH	2.5	$4.4 \times 10^{-4}$	17.7	$0.73 \times 10^5$	0.50	1.60
31% RH	1.3	$2.2 \times 10^{-4}$	13.7	$0.69 \times 10^5$	0.41	1.99
13% RH	0.3	$4.3 \times 10^{-4}$	12.5	$1.35 \times 10^5$	0.43	1.44
97% RH	6.5	$22.0 \times 10^{-4}$	12.8	$0.90 \times 10^5$	1.10	1.13

### 3.5 Chemical hardening/softening of clay particles

Another factor that can be responsible for the observed increase of the S-wave moduli with drying is a chemical hardening of clay particles. Recently, it has been shown that water desorption significantly affects the elastic properties of individual clay particles (e.g., Ebrahimi *et al.*, 2012; Carrier *et al.*, 2014). For example, Ebrahimi *et al.* (2012) used molecular dynamics simulations to calculate the full elastic tensor of Wyoming Na-montmorillonite, a member of the smectite group, over the range of hydration conditions. They simulated the molecular structure of Na-montmorillonite and reported the dependencies of the VTI stiffness tensor components on the layer basal spacing, the characteristic of the thickness of the water layer between two clay platelets. It was shown that a reduction in water content results in an increase in the stiffness constants of an individual Na-montmorillonite particle.

Natural shales are highly heterogeneous as these rocks are composed of many components, including fluid-saturated pores, silt inclusions, and clay particles spatially distributed at different angles to the bedding plane of a shale. I use the elastic properties of Na-montmorillonite clay particles reported in Ebrahimi *et al.* (2012) to quantify how the elastic properties of a clay composite comprised of oriented particles vary with water content and how these values are related to the elastic properties of natural shales.

The spatial distribution of particles can be described with an orientation distribution function (ODF),  $W(\theta, \varphi, \psi)$ , which is a function of the three Eulerian angles. An ODF gives a probability of a certain orientation and must satisfy the normalisation condition

$$\int_0^{2\pi} \int_0^{2\pi} \int_0^\pi W(\theta, \varphi, \psi) \sin \theta d\theta d\varphi d\psi = 1, \quad (29)$$

where integrals are taken over all possible orientations. In the case of VTI media, one can assume a random (homogeneous) distribution of particles relative to the angles  $\psi$  and  $\varphi$ . Thus, an ODF is a function of only one Eulerian angle  $\theta$ , the angle between the vertical axis and the normal vector to the surface of a clay particle,  $W(\theta)$ . Therefore, condition 29 becomes

$$4\pi^2 \int_0^\pi W(\theta) \sin \theta d\theta = 1. \quad (30)$$

The components of the elastic stiffness tensor of the composite medium comprised of particles, the distribution of which is described with an ODF  $W(\theta, \varphi, \psi)$ , can be expressed as

$$C_{ijkl} = \int_0^{2\pi} \int_0^{2\pi} \int_0^\pi W(\theta, \varphi, \psi) C_{ijkl}^0(\theta, \varphi, \psi) \sin \theta d\theta d\varphi d\psi, \quad (31)$$

where  $C_{ijkl}^0(\theta, \varphi, \psi)$  are the components of the stiffness tensor of a clay particle with a certain orientation  $\theta, \varphi, \psi$  in the laboratory coordinate system, which can be obtained from the elastic properties of a particle  $C_{ijkl}^p$  as

$$C_{ijkl}^0(\theta, \varphi, \psi) = \alpha_{ip} \alpha_{jq} \alpha_{kr} \alpha_{ls} C_{pqrs}^p, \quad (32)$$

$$\boldsymbol{\alpha} = \begin{pmatrix} c_2 c_3 - c_1 s_2 s_3 & -c_2 s_3 - c_1 s_2 s_3 & s_1 s_2 \\ s_2 c_3 + c_1 s_2 s_3 & -s_2 s_3 + c_1 s_2 s_3 & -s_1 c_2 \\ s_1 s_3 & s_1 c_3 & c_1 \end{pmatrix}, \quad (33)$$

$$\mathbf{c} = (\cos \theta \quad \cos \varphi \quad \cos \psi), \quad (34)$$

$$\mathbf{s} = (\sin \theta \quad \sin \varphi \quad \sin \psi). \quad (35)$$

I use equations 31–35 to calculate the elastic properties of such composite VTI clay comprised of oriented clay particles with elastic moduli  $C_{ijkl}^P$  reported in Ebrahimi *et al.* (2012). Figure 25 shows three realisations of such a composite medium: (1) with fully aligned particles; (2) with random distribution of particles; and (3) with an ODF of clay particles reported in Beloborodov *et al.* (2016). The elastic properties of the composites are shown in Figure 25 in terms of the components of the stiffness tensor in Voigt notation (e.g., Mavko *et al.*, 2009).

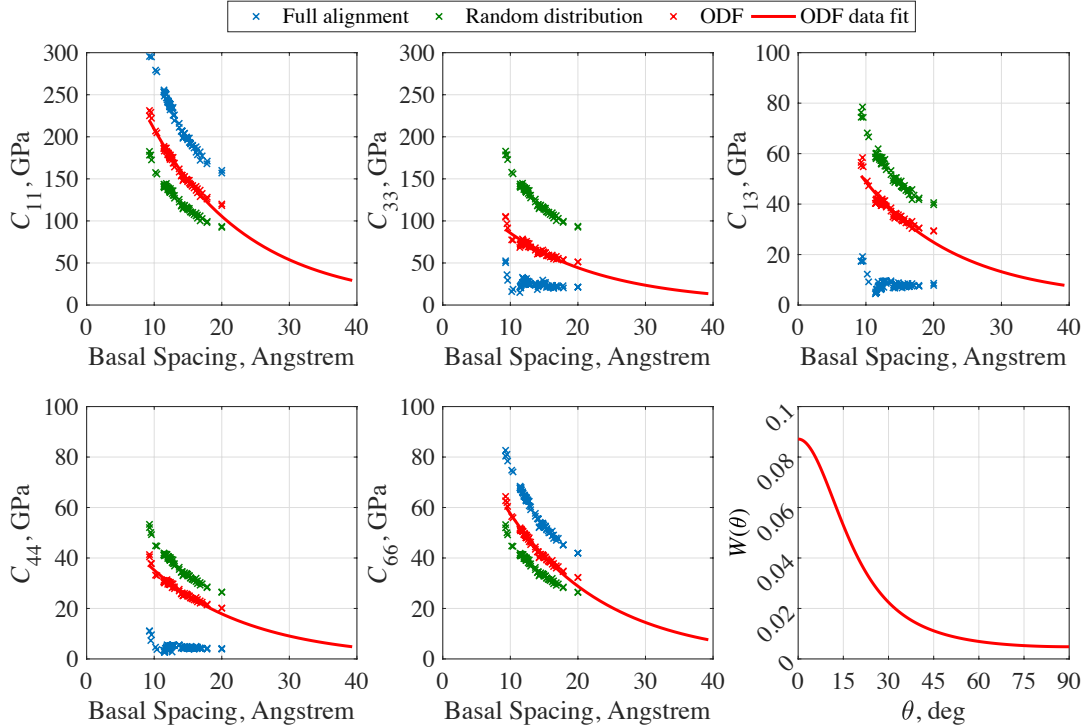


**Figure 25** Dependence of elastic moduli of clay composites comprised of Na-montmorillonite clay particles on the thickness of water layer between clay platelets (Basal Spacing). The blue data points represent the composite with fully aligned clay particles, of which the elastic properties are reported in Ebrahimi *et al.* (2011). The green data points represent the composite with random (isotropic) distribution of clay particles ( $C_{11} = C_{33}$ ,  $C_{44} = C_{66}$ ,  $C_{13} = C_{11} - 2C_{66}$ ). The red data points represent the composite comprised of clay particles oriented according to the orientation distribution function (ODF),  $W(\theta)$ , from Beloborodov *et al.* (2016), which is shown in the bottom right corner.

The realisation with fully aligned particles replicates the elastic properties of individual clay platelets from Ebrahimi *et al.* (2012). The random distribution of particles gives an isotropic composite medium. These two realisations give the bounds for the elastic properties of a composite comprised of the given clay platelets. Any VTI orientation of particles will give the medium with the elastic moduli

located between these bounds. For example, I take an orientation of clay particles measured with neutron diffraction in one of the compacted shales reported in Beloborodov *et al.* (2016). Red data points in Figure 25 show the elastic properties of the composite media comprised of such particles versus the basal spacing, i.e. the amount of water in the particles. The values of the moduli of the clay composite overestimate the elastic coefficients experimentally measured in Opalinus shale at different hydration states Figure 20. One can get the comparable values of the elastic moduli if the obtained dependencies are extrapolated to the higher basal spacing, hence a higher amount of water. However, it is challenging to correctly attribute the water content in natural shales to the basal spacing in clay particles. Moreover, such modelling does not take into account the changing elastic properties of compliant porosity in shales, of which the importance was demonstrated in the section 3.4 Nevertheless, the reported analysis shows that the hardening/softening of individual clay particles with drying/rehydration is an important mechanism that should be taken into account in study of the effect of hydration on the elastic properties of shales.

### 3.6 Conclusions

The measured dependencies of the elastic properties of Opalinus shale on hydration cannot be explained by one driving mechanism. I have highlighted and discussed four possible driving factors for such behaviour of the elastic moduli: (1) variation in the total porosity, (2) substitution of pore-filling fluid, (3) change in stiffness of the contacts between clay particles, and (4) chemical hardening/softening of clay particles. I have performed qualitative and quantitative analysis of the influence of these driving factors on the elastic moduli of the Opalinus shale. I have shown that the observed variation of the total porosity cannot explain the strong dependency of S-wave moduli on hydration. Such dependency most likely results from the changing stiffness of compliant pores in the shale, and chemical hardening/stiffening of individual clay particles. In addition to the factors influencing the S-wave moduli, the P-wave moduli are also affected by fluid saturation, which, contrary to other effects, leads to a decrease of the P-wave moduli with drying and an increase of the moduli with rehydration.

Therefore, the dependence of the elastic moduli on the hydration state of shales is a complex phenomenon driven by a number of competing factors. In certain

circumstances, some of these factors dominate over others to determine the overall variations of the elastic moduli. Thus, the dependence of the elastic moduli on hydration can be different in different shales depending on the composition and microstructure of the rock. Developing a comprehensive rock physics model that takes into account all the discussed factors will be a step towards better understanding of the phenomenon. Additionally, taking into account other factors, which were not discussed in this work (such as an effect of the bound water) will be beneficial to the understanding of the observed phenomenon.

According to the presented analysis, the stiffness of compliant porosity is significantly affected by changes in hydration in shales. This effect can be responsible for the observed drastic variations in the shear elastic moduli of shales and requires thorough investigation. The compliant porosity in shales is constituted by contacts between clay aggregates and clay particles – pores of nanoscale size. The study of the effect of changing the hydration of compliant pores on the elastic properties of shales as a stand-alone process is challenging because of the structural complexity of shales and the superposition of this effect with other effects caused by changing hydration. Therefore, in the following chapter (Chapter 4), I study the effect of changing hydration on the stiffness of compliant porosity in sandstone, an isotropic and less heterogeneous rock. At low water content, sandstones exhibit a weakening of elastic properties with hydration, similar to the observed behaviour of shales. The understanding of how the sorption of water in compliant pores of sandstones affects their elastic properties can contribute to better understanding of the physical effects of hydration on the elastic properties of shales.

# Chapter 4. The effect of varying hydration on the deformation and elastic properties of sandstones<sup>\*</sup>

## 4.1 Introduction

The effect of elastic weakening of granular porous rocks with adsorption of a small amount of water has been known for several decades. For example, Murphy (1982) showed significant increase of compressional and shear wave velocities (60% and 70% respectively) measured at seismic frequencies on Massillon sandstone dried to low saturations <1%. He also demonstrated the same effect of low water saturations on attenuation of the waves. A similar effect of small amounts of water on the elastic properties of sands and sandstones was reported by Wyllie *et al.* (1962), Hardin and Richart (1963), Clark *et al.* (1980), Knight and Dvorkin (1992), and Tutuncu (1992). Hossain (2017) reported elastic weakening of Bentheim sandstone samples with adsorption of water observed in static experiments. Pandit and King (1979), Clark *et al.* (1980) and Tittmann *et al.* (1980) studied attenuation in rocks with low saturations at seismic frequencies. Recently, Pimienta *et al.* (2014) studied dependency of ultrasonic elastic wave velocities in a limestone and a sandstone on variations in relative humidity (RH) at ambient temperature and pressure. They observed elastic weakening of both rocks with increasing RH (hence, adsorption of water in samples). The observed change in elastic properties and attenuation in the limestone was relatively small, but was much stronger in the sandstone.

The effect of RH on elastic properties is important for the application of conventional rock physics theories such as Gassmann theory (Gassmann, 1951; Brown and Korrington, 1975; Smith *et al.*, 2003). This theory requires an a priori knowledge of the bulk and shear moduli of the dry rock, generally obtained from laboratory measurements at room conditions. Although the standard sample preparation practice involves drying of the sample at high temperatures in a vacuum,

---

<sup>\*</sup> This chapter is an extended version of the paper Yurikov, A., M. Lebedev, G. Gor, and B. Gurevich, 2018, Sorption-induced deformation and elastic weakening of Bentheim sandstone: Journal of Geophysical Research – Solid Earth, **123**(10), 8589–8601, doi: 10.1029/2018JB016003

measurements of elastic properties are conducted at room RH. In the case of sandstones, the adsorption process is fast. Thus, even after proper preparation of the sample, one can obtain significantly different results depending on the RH in the laboratory. Therefore, understanding the effect of RH on the moduli is of high importance, particularly for measurements on sandstones.

Pimienta *et al.* (2014) and, earlier, Murphy *et al.* (1984) explained the elastic weakening phenomenon with the concept of changing free surface energy (Johnson *et al.*, 1971). The surface energy is a potential energy of creating a new surface. The higher the potential energy is, the stronger the cohesive forces between the grains are. Water adsorbed at a grain surface lowers the surface energy and reduces cohesion between grains. Thus, adsorption leads to elastic weakening in granular materials.

Additionally, adsorption of fluid is responsible for the deformation of rocks and porous materials. Following are the milestones of adsorption-induced deformation study summarised in a comprehensive review paper by Gor *et al.* (2017). McBain and Ferguson (1927) were the first to report the swelling of sandstone, limestone, and cement caused by an increase in air humidity, although they did not conduct any measurements of strain. Throughout the next several decades, studies of adsorption-induced deformation were focused on charcoal (Meehan, 1927; Bangham and Fakhoury, 1928; Bangham and Razouk, 1938; Briggs and Sinha, 1934), porous glasses (e.g., Amberg and McIntosh, 1952), and silica (e.g., Reichenauer and Scherer, 2000, 2001). The order of observed deformation in carbons and glasses was about  $10^{-3}$ , while measurements on high-porous silica aerogel showed huge strain of 30%. The observed adsorption-induced deformation was explained by a reduction of free surface energy leading to relaxation and expansion of a solid surface. This is known as Bangham's law, which states that the strain is proportional to the change in surface energy of the porous material. However, some experimental data contradict this statement (Haines and McIntosh, 1947; Dolino *et al.*, 1996; Boissiere *et al.*, 2005; Sharifi *et al.*, 2014). Thus, Gor and Bernstein (2016) revisited Bangham's law. They emphasised that the experimentally observed adsorption-induced strain is governed by the change in surface stress – that is, a stretch of existing surface – rather than by creation of a new surface. This concept is more general than Bangham's law, which is an approximation valid in most cases, although with some exceptions.

The elastic properties of rocks usually exhibit strong stress dependency, which is caused by compliant grain contacts and is reasonably well understood. Therefore, it is logical to explain the elastic weakening observed at low saturations in sandstones in terms of the change in the surface stress, rather than change in the surface energy. The surface stress change may happen due to the adsorption of water in small compliant pores at the grain contacts. The adsorption of fluid in nanopores results in elevated fluid pressure (e.g., Gor and Bernstein, 2016). Therefore, if the adsorption-induced pressure in compliant pores is indeed the cause of the weakening, then this pressure should cause tensile deformation of the samples. Thus, one way to check the validity of the proposed mechanism of sorption-induced weakening is to simultaneously measure the elastic properties and deformation of a sandstone as a function of humidity. To this end, I conduct measurements of deformation of Bentheim sandstone in an atmosphere with controlled RH. The deformation data are complemented with results of ultrasonic velocity measurements and estimation of saturation of the sample. I show that the elastic weakening effect in sandstones is accompanied by significant tensile deformation of the order of  $10^{-4}$ . From measurements of this deformation and the bulk modulus of the rock, I estimate the fluid pressure that causes the rock to expand. Finally, I verify the suggested hypothesis that sorption-induced elastic weakening of the sandstone can be caused by variations in the fluid pressure. This is done by comparing the changes in the measured elastic moduli related to the estimated fluid pressure with stress dependency of the moduli of the Bentheim sandstone measured in a triaxial cell at room conditions.

## 4.2 Materials and Methods

### 4.2.1 Studied sample

This study focuses on independent measurements of deformation and variations in the elastic properties in granular rocks caused by water sorption mechanisms. I conduct the experimental study on the outcrop Bentheim sandstone from the Gildenhäusen quarry, Germany. The outcrop is composed of 95% quartz, 3% kaolinite, and 2% orthoclase. This sandstone is nearly isotropic and homogeneous with round to subround quartz grains sized 50–500  $\mu\text{m}$  (Klein *et al.*, 2000). Some elastic anisotropy effects may exist, but they are likely to be of second

order compared to those considered in this study. The porosity of the outcrop is ~24%, measured from the mass difference between a fully water-saturated sample and the same sample dried in a vacuum chamber under 60 °C. Two samples are prepared for measurement. The primary sample, of a cubic shape with an edge size of approximately 5 cm, is used for deformation and ultrasonic measurements. The second sister sample of an arbitrary shape is used to estimate variation in the saturation with adsorption/desorption of water.

#### 4.2.2 Control of saturation

I regulate the sorption process by maintaining the samples in a surrounding atmosphere with controlled RH. The samples are placed into a desiccator, an enclosed container with a presence of various salt solutes called desiccants (e.g., Greenspan, 1977). The type of desiccant and temperature define the RH. To minimise the influence of variations in the temperature on the results of the experiment, I conduct the measurements in an air-conditioned room with temperature  $T = 24 \pm 1^\circ\text{C}$ . The desiccants used and the corresponding RH values at room temperature are summarised in Table 6. I continuously record variations in the temperature and humidity of the atmosphere around the samples with the data logger EL-USB-2-LCD+ (Lascar) placed inside the desiccator. The logger provides accuracy of temperature and RH measurements of  $\pm 0.5^\circ\text{C}$  and  $\pm 3\%$ .

**Table 6** The list of salts used for the sorption experiment with the corresponding range of relative humidity (RH) at room temperature.

Salt	Formula	RH at 24 °C
Potassium Sulfate	$\text{K}_2\text{SO}_4$	97–98 %
Potassium Chloride	KCl	86–88 %
Sodium Chloride	NaCl	76–78 %
Magnesium Nitrate	$\text{Mg}(\text{NO}_3)_2$	52–55 %
Potassium Carbonate	$\text{K}_2\text{CO}_3$	44–47 %
Calcium Chloride	$\text{CaCl}_2$	26–31 %
Potassium Acetate	$\text{KC}_2\text{H}_3\text{O}_2$	23–26 %
Lithium Chloride	LiCl	11–15 %

#### 4.2.3 Measurements of deformation

The schematic of the experimental set-up is shown in Figure 26. I have glued a semiconductor strain gauge (Type KSP-6-350-E4, Kyowa Ltd.) to a face of the primary sample to measure the deformation of the sandstone caused by sorption of water. The deformation of the sample leads to the deformation of the gauge. To precisely measure the following change in the resistance, the strain gauge is connected to the Wheatstone electrical bridge. Reading the voltage difference between two legs of the bridge allows accurate measurements of the changes in gauge resistance and calculation of deformation (e.g., Hoffmann, 1986). The acquisition system comprises a digital multimeter 34461A 6½ (Keysight Ltd.) and a PC, which enables continuous monitoring and recording of the strain gauge readings during the sorption process (Figure 27). In designing the experiment, I attempted to minimise the influence of any external factors on the strain gauge readings. I used the air conditioner to maintain the same temperature ( $\pm 0.5$  °C) in the area and covered a desiccator to prevent illumination by light (which can also affect strain gauge readings) and the influence of any unwanted air gusts.

#### 4.2.4 Ultrasonic measurements

Ultrasonic velocity measurements are conducted using the pulse transmission technique (e.g. Birch, 1960). Two piezoelectric shear transducers V153 1 MHz/0.5 in. (Olympus Panametrics-NDT™) are glued to the opposite faces of the primary sample. The acquisition system includes a rectangular form electrical pulser/receiver 5077PR (Olympus Ltd.) and a digital phosphor oscilloscope TDS 3034C (Tektronix Ltd.). A waveform of the ultrasonic pulse transmitted through the sample is recorded and processed to obtain P- and S-wave velocities (e.g., Lebedev *et al.*, 2013). The dead time of the electronics is taken into account during processing of the experimental data.

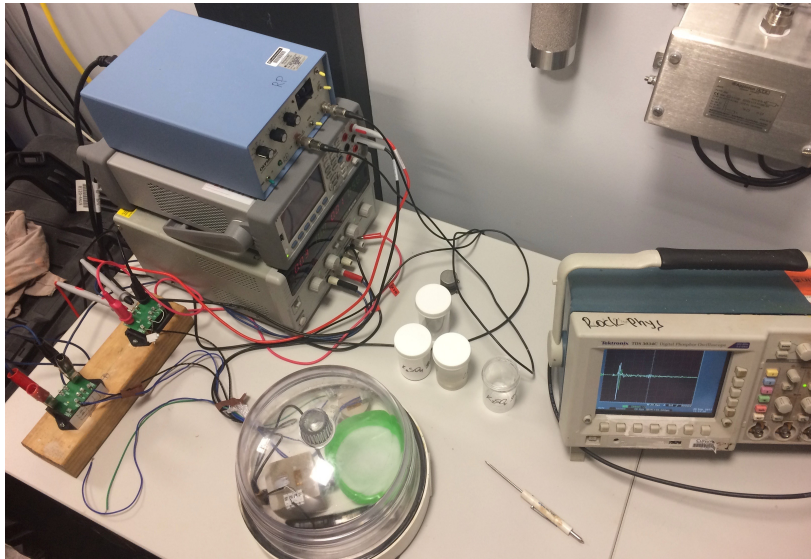
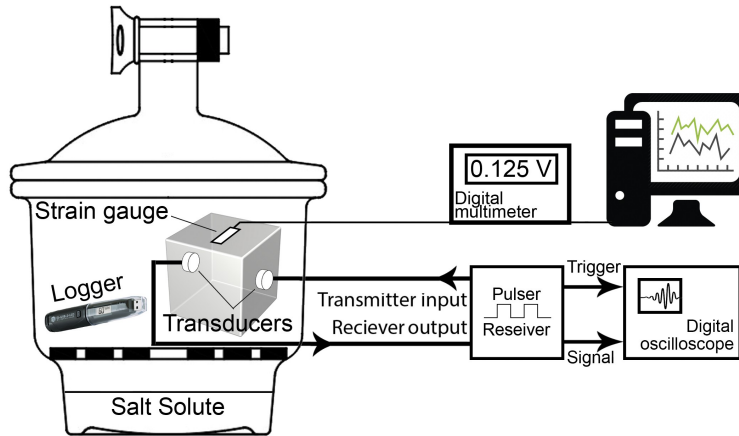


**Figure 26** Top: schematic of the experimental setup for measurements of sorption-induced deformation and variations in the elastic properties of rocks. Bottom: image of the experimental setup.

#### 4.2.5 Hydration procedure

The stabilisation of the RH inside the enclosed desiccator takes 3–7 days (Figure 27). Meanwhile, it is reported that the final saturation of high-porous sandstones due to the sorption process is reached within several hours after RH stabilisation (e.g., Pimienta *et al.*, 2014). The strain gauge readings show that the deformation caused by sorption generally follows a change in RH (Figure 27). Therefore, I conduct ultrasonic velocities measurements and proceed to the next desiccation stage only after strain gauge readings are stabilised, which usually takes up to one week.

The sorption process is started with the driest possible state. First, I keep the samples inside a vacuum chamber under a temperature of 60 °C for 24 hours. Then I

place the samples in the 13% RH atmosphere, the driest state that can be reached with the given set of desiccants. After stabilisation of strain gauge readings and conducting of velocity measurements, I change the desiccant to set 97% RH around the sample and measure the deformation and ultrasonic velocities again. Then, starting from this wet state, I follow the desorption path back to 13% RH through the intermediate humidity states (Figure 28a) measuring strain, and P- and S-wave velocities. Afterwards, desorption is followed by an adsorption path through the same stages.

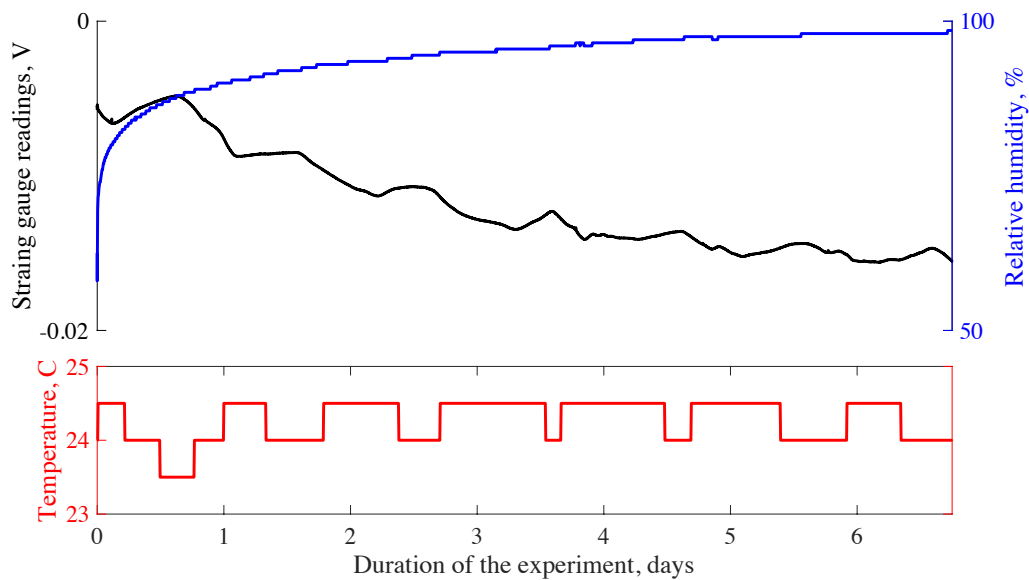


**Figure 27** Readings from the strain gauge and the data logger for the adsorption process with 97% RH potassium sulfate desiccant.

## 4.3 Results

### 4.3.1 Deformation and saturation

As an example, Figure 27 shows the strain gauge readings during the first adsorption stage with the recorded temperature and humidity logs. The voltage difference is negative because the adsorption of water in the sandstone leads to tensile deformation causing increase of the gauge resistance. The saw tooth patterns of the strain gauge readings in Figure 27 correspond to the recorded temperature change. The variation in the temperature by 0.5 °C affects the RH inside the desiccator, which leads to larger expansion or shrinkage of the sample as registered by the strain gauge. Because a small variation in the temperature noticeably

influences the strain gauge readings, I average the recorded data after RH stabilisation to calculate the corresponding strain of the sample.

Figure 28a shows the strain of the sample versus RH expressed as a ratio of the partial pressure of water vapour to the equilibrium vapour pressure of water. The values of RH at the adsorption and desorption points in Figure 28a are slightly different because concentrations of the solutes slightly differed, although I used the same salts. The first adsorption stage shows that with a change in the RH from the driest possible state of 13% to the wettest possible state of 97%, the observed deformation of the sample is of the order of  $10^{-4}$ . The following desorption path results in a gradual decrease of strain. However, at the end of the desiccation process, the sample did not restore its initial shape, and residual strain of  $\sim 5 \times 10^{-5}$  remained. The following adsorption stages result in an increase of strain of the sample. Therefore, I conduct one cycle of the measurements and observed a hysteresis in deformation. To ensure that the hysteresis is not a result of a drift in strain gauge readings, I run the measurements at a single RH state for an extended period of time ( $\sim 1$  month). The measurements show that strain gauge readings fluctuate over time (probably related to the temperature effect on RH) but do not drift. I cannot fully explain the origin of the observed hysteresis effect now but will investigate this in the future.

For the measurements I use the reference point at the hydration state of RH = 46%, which corresponds to the average room humidity. This means that the sample is assumed to have no strain at this state and deformation of the sample at other RH levels is calculated relative to the reference point.

Along with measurements of deformation I estimate the water saturation (volume of adsorbed water over the total pore volume) reached after RH stabilisation at different hydration states along the desorption and adsorption paths. The saturation was estimated by measuring the mass change of the sister sample  $\Delta m$ , knowing the porosity  $\phi$ , mass of the dry sample  $m_{dry}$ , and density of grains  $\rho_g = 2.65 \text{ g/cm}^3$ :

$$s = \frac{\Delta m}{m_{dry}} \frac{\rho_g}{\rho_w} \left( \frac{1}{\phi} - 1 \right) \cdot 100\%. \quad (36)$$

The results presented in Figure 28b show that saturation at the wettest hydration state is just over 2%. Additionally, a hysteresis of saturation is observed at humidity higher than 50%.

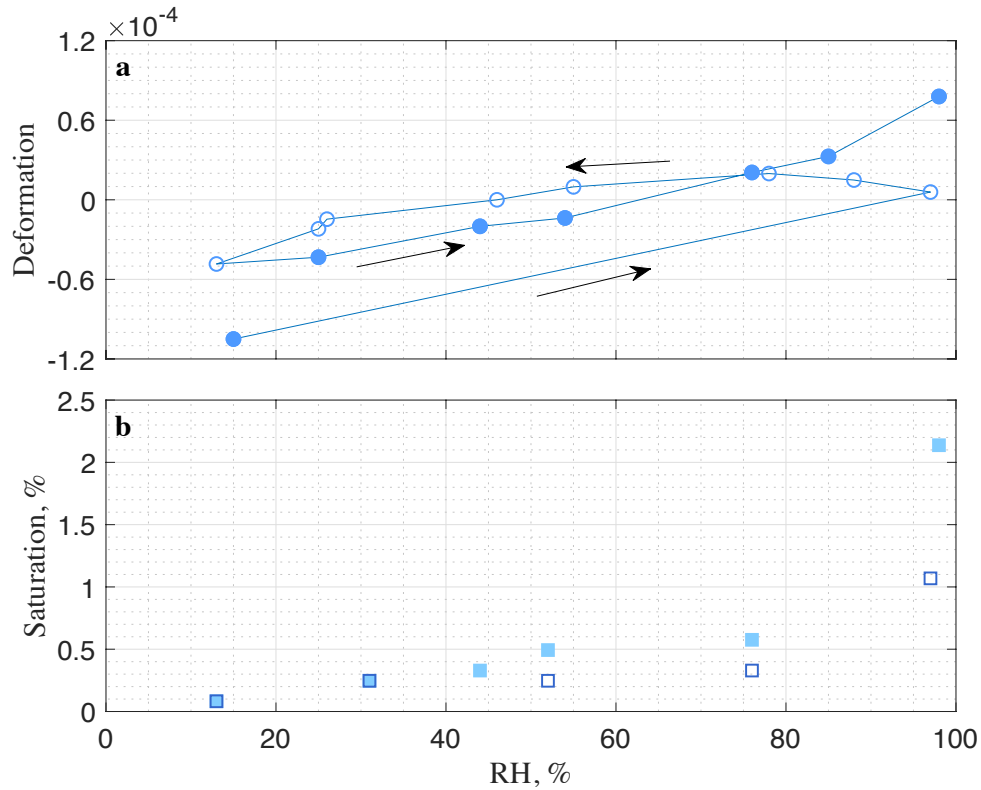


**Figure 28** a) Deformation of the primary sample versus relative humidity (RH). The black arrows show the direction of the sorption process. b) Estimation of saturation ( $V_{fluid} / V_{pore}$ ) versus RH done on the sister sample, where the size of the markers represents an experimental error. The filled markers represent adsorption data; the hollow markers represent desorption data.

#### 4.3.2 Analysis of ultrasonic measurements

The recorded waveforms of transmitted ultrasonic pulses at each stage of the sorption experiment are shown in Figure 29a-b. The traveltimes of P- and S-waves can be determined as the first onset of energy and arrival of high-amplitude signal, respectively. One can observe an increase of traveltimes of both P- and S-waves with an increase of RH inside the desiccator. This indicates a decrease in the elastic moduli of the sandstone sample with adsorption of water and the opposite effect with desorption. Additionally, attenuation of registered elastic waves is detected. Figure 29c shows the frequency spectra of the recorded waveforms. The reduction of spectra magnitudes with higher RH emphasises an increase of attenuation in the sample.

In order to quantify variations in the elastic properties with sorption, I determine the dependence of the elastic wave velocities on RH from the recorded

waveforms. I use a combination of an iterative cross-correlation-based workflow with the short- and long-time average ratio method (e.g., Akram and Eaton, 2016) for precise picking of traveltimes. This workflow is independently applied for the detection of P- and S-waves traveltimes. It ensures a systematic approach and reduces human factor errors during processing of the experimental data. The calculated velocities of P- and S-waves ( $V_P$  and  $V_S$ ) are shown in Figure 30a. Both  $V_P$  and  $V_S$  exhibit  $\sim 15\%$  increase with desorption. The adsorption of water leads to a decrease in velocities, given that the velocity variations as a function of RH with adsorption replicate those obtained on the desorption path. Then I use the measured ultrasonic velocities to calculate the dynamic bulk and shear moduli (Figure 30b). The moduli exhibit similar dependencies on RH, exhibiting the difference between the wettest and the driest states, which reaches 20%.

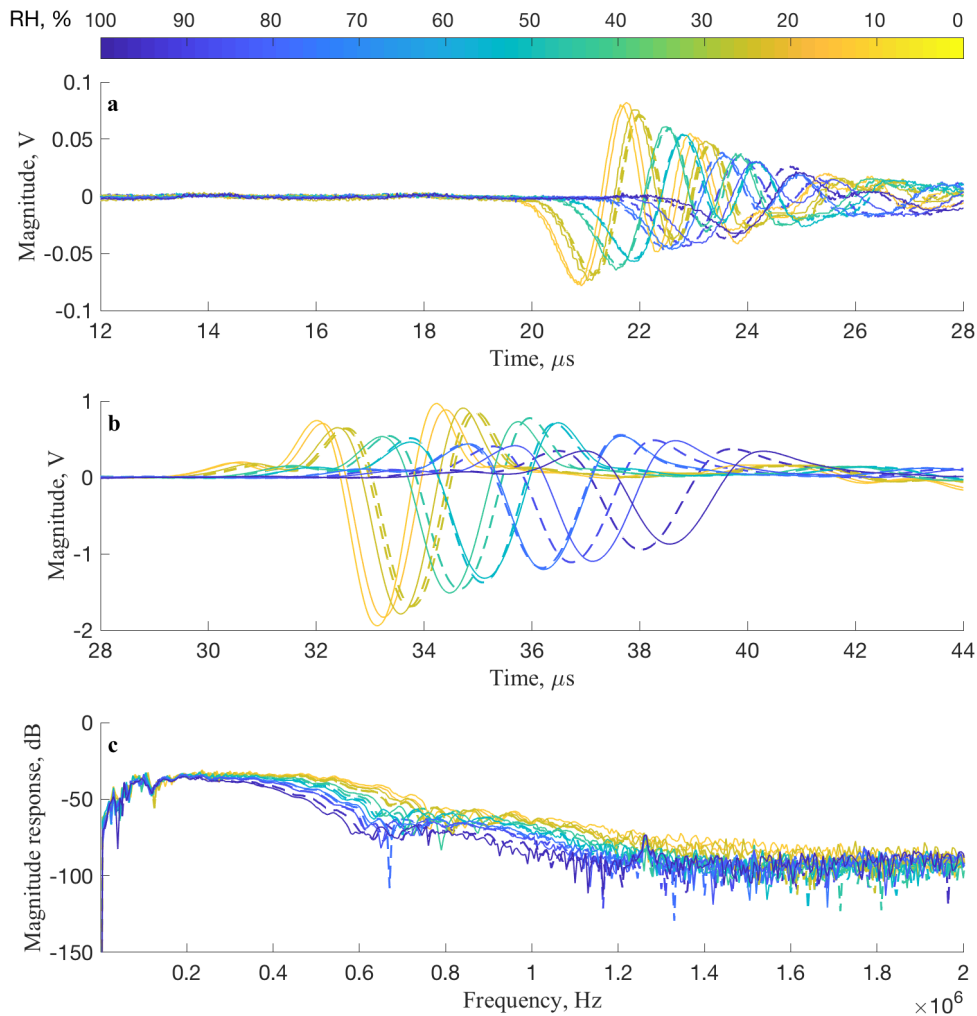


**Figure 29** Waveforms recorded at different relative humidity (RH) split into two parts: a) P-wave; b) S-wave. Note the change of vertical scale. c) Frequency spectra of transmitted

ultrasonic pulses at different RH. RH is colour-coded. Dashed lines represent waveforms recorded at desorption path; the solid lines represent an adsorption path.

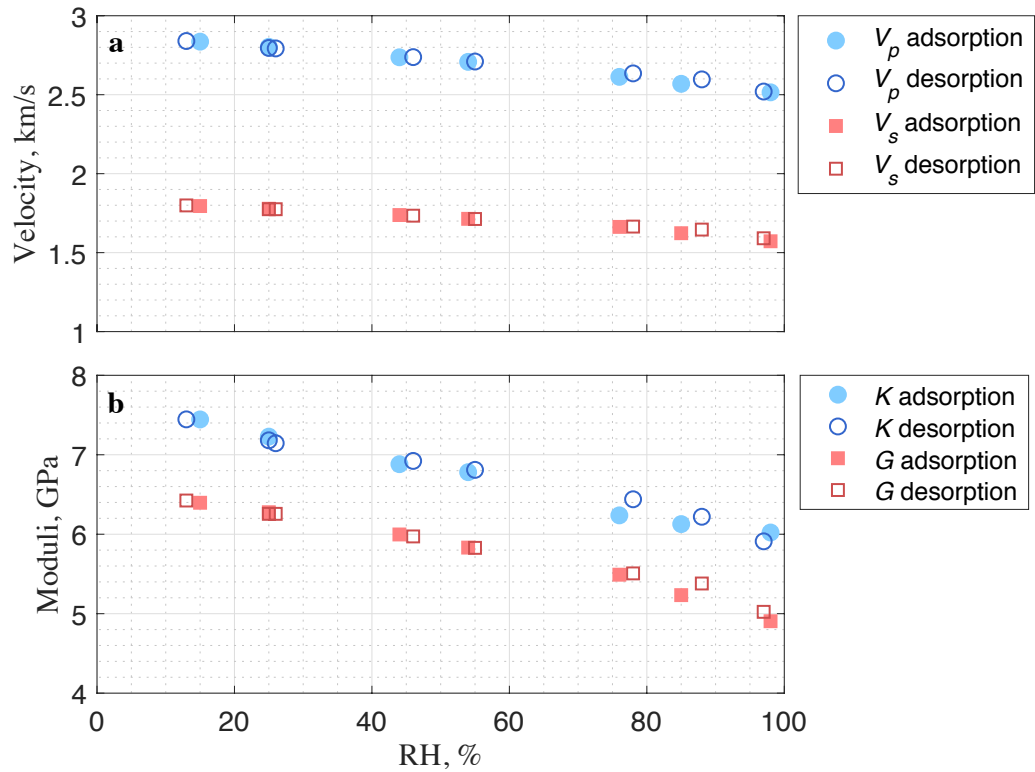


**Figure 30** a) Dependence of the P- and S-wave velocities on relative humidity (RH) at desorption and adsorption paths. b) Dependence of the bulk  $K$  and shear  $G$  moduli on RH at desorption and adsorption paths.

The attenuation of P- and S-waves is estimated using the centroid frequency shift method (e.g., Kuc *et al.*, 1976; Narayana and Ophir, 1983; Quan and Harris, 1997; Pevzner *et al.*, 2012). This method is often used to estimate the quality factor  $Q$  of seismic waves in the earth from the shift of the centroid frequency of a signal between a pair of receivers located along the raypath. A signal recorded at the first seismic receiver is treated as a source signal. A signal recorded at the second seismic receiver is considered the attenuated source signal, which has travelled a certain distance through the geological formation. The setup of the experiment described in this study is somewhat different. I have waveforms recorded after propagation through the rock at different RH, while the source signal is unknown. To overcome the issue with the unknown source signal, I use the waveform recorded at the driest hydration state (at 13% RH) as a reference signal and assume some  $Q = Q_{ref}$  of the rock in this state. Then I derive  $Q$  of the sample at the other hydration states by

applying the centroid frequency shift method to the corresponding waveforms with respect to the reference signal. This gives a series of  $Q$  values as a function of RH for a given value of  $Q_{ref}$ . This series can be extrapolated to estimate  $Q = Q_0$  at RH = 0. There may be some small attenuation at RH = 0 caused by factors other than presence of water in the rock. However, since I am interested in the attenuation caused by the presence of small amounts of water, it is reasonable to assume that this particular attenuation is zero at RH = 0. Thus I assume that at RH = 0 there is no attenuation and  $Q_0 = \infty$ . This suggests that the value of  $Q_{ref}$  should be chosen such that the extrapolation to RH = 0 yields  $Q_0 = \infty$ . The corresponding value of  $Q_{ref} = 300$ .

Attenuations of P-waves and S-waves in the sandstone sample are independently analysed. To do so, I separate P- and S-wave oscillations from the rest of each recorded waveform. Frequency spectra of these signals are shown in Figure 31. The spectra are close to the Gaussian type. Therefore, there is no need to introduce any additional scaling factor (e.g., Pevzner *et al*, 2012). Figure 32 shows variation in  $Q^{-1}$  related to RH change for the assumed  $Q_{ref}$ . First, the quality factor of the rock correlates with the elastic properties in their dependence on RH. Second, attenuation of an S-wave is consistently higher than attenuation of a P-wave. Finally, the quality factors of the rock for P-waves and S-waves decrease with adsorption to the values of 50 and 40 relating to the assumed  $Q_{ref} = 300$ .

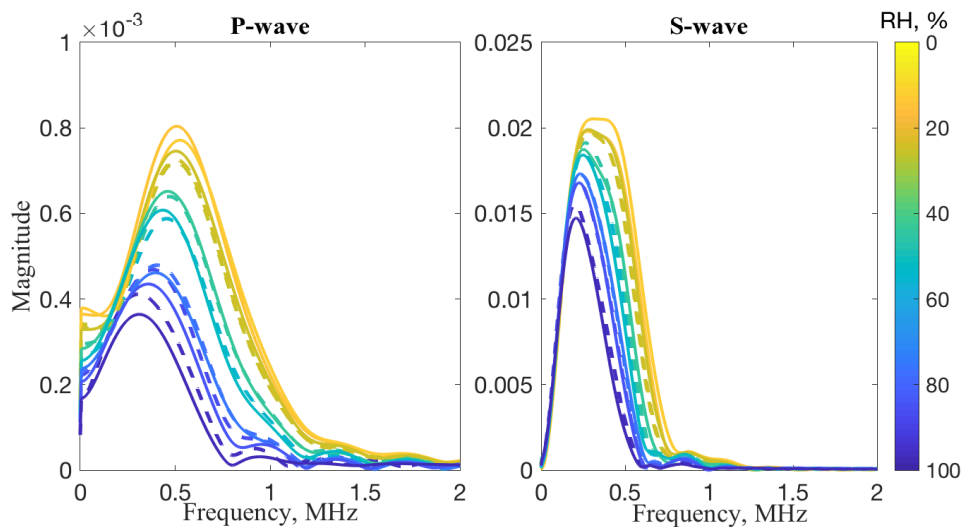


**Figure 31** Frequency spectra of P-wave and S-wave signals at different hydration states. Relative humidity (RH) is colour-coded. The dashed lines represent the desorption path; the solid lines represent the adsorption path.

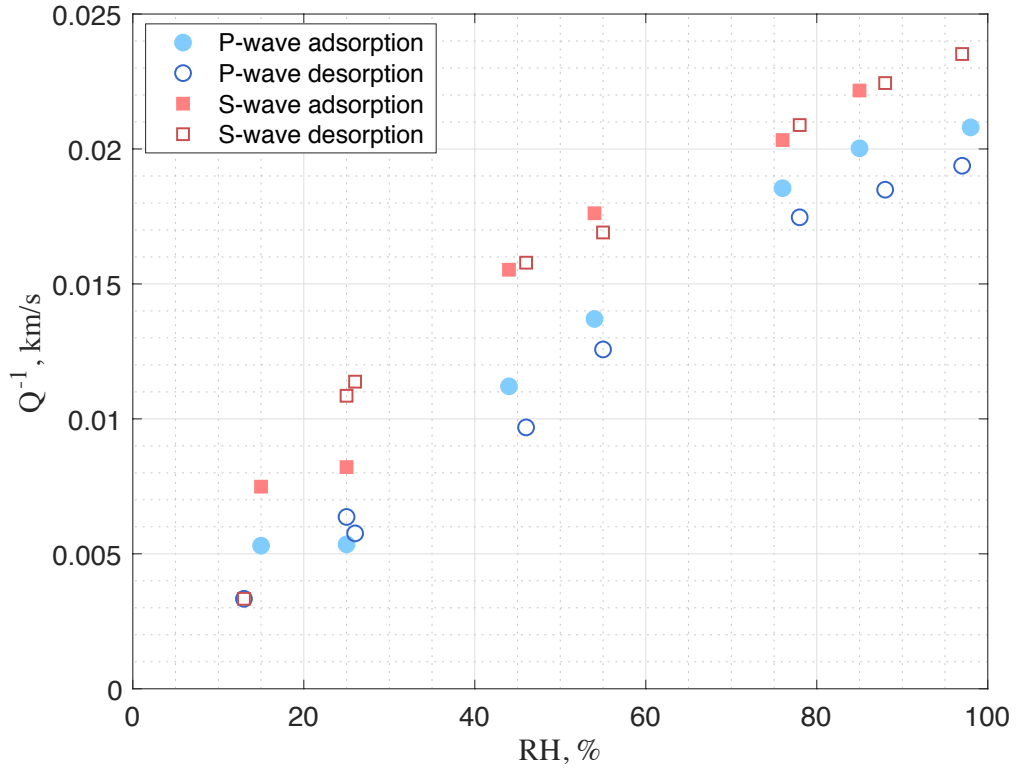


**Figure 32** Variation in attenuation in the sandstone versus relative humidity (RH),  $Q_{ref} = 300$  at RH = 13%.

#### 4.4 Analysis of results

I have observed that elastic weakening of the Bentheim sandstone is accompanied by tensile deformation of the sample of the order of  $10^{-4}$ . Such deformation may be caused by change in the surface stress due to the solid–fluid interactions (Vandamme *et al.*, 2010; Gor and Bernstein, 2016). This effect can be described as an additional term in the pressure of the adsorbed fluid, called adsorption stress or solvation pressure (e.g., Gor and Neimark, 2010; Gor and Gurevich, 2018). One can estimate the magnitude of the change in the solvation pressure from the measured linear deformation  $\varepsilon$  using the equation:

$$\Delta p_f = M_{pl}\varepsilon, \quad (37)$$

where  $M_{pl}$  is the so-called pore load modulus (Prass *et al.*, 2009).  $M_{pl}$  is related to the bulk pore compressibility  $C_{bp}$  (Zimmerman *et al.*, 1986) as

$$M_{pl} = 3/C_{bp}, \quad (38)$$

with factor 3 accounting for the fact that the pore load modulus is defined for linear strain, whereas the pore compressibility is for volumetric strain. The bulk pore

compressibility  $C_{bp}$  can be related to the elastic moduli of the rock using Biot's theory of poroelasticity, assuming that the rock is isotropic and consists of a single isotropic solid material (Zimmerman *et al.*, 1986):

$$C_{bp} = \frac{3}{M_{pl}} = \frac{1}{K} - \frac{1}{K_s}, \quad (39)$$

where  $K$  is the drained bulk modulus of the rock and  $K_s$  is the bulk modulus of the solid. Using the bulk modulus of quartz  $K_s = 38$  GPa, and  $K = 6.9$  GPa gives  $M_{pl} = 25.3$  GPa. Here I use the dynamic modulus  $K = 6.9$  GPa instead of the static modulus, although the difference between static and dynamic moduli can be 5–20% (e.g., Cheng and Johnston, 1981; Jizba *et al.*, 1990; Fjær, 2009). However, since I am seeking an estimation of the magnitude of change in the solvation pressure and a qualitative agreement with other experimental data, this effect can be neglected. The reader can find measurements of the effects of humidity on static moduli of sandstones, for example, in Hossain (2017). It will be interesting in the future to add measurements of static moduli to my experiment and discuss the potential application of the observed effects to field data.

From equation 37, I obtain the variation in the solvation pressure with changing RH. The result is shown in Figure 33. Here, the reference hydration state, where  $\Delta p_f = 0$ , is the state with room RH = 46%. This state is chosen as reference because I need to compare these results with the measurements of stress dependency of the elastic properties of the Bentheim sandstone done at room RH.

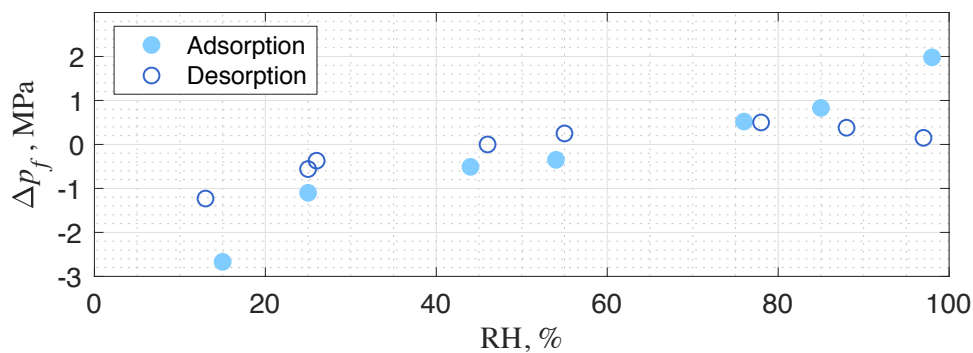


**Figure 33** Variations in the solvation pressure as a function of relative humidity (RH) estimated from equation 37. The reference state, where  $\Delta p_f = 0$ , is the state with room RH.

The elastic moduli of the Bentheim sandstone are pressure-dependent (e.g., Benson *et al.*, 2005; Saenger *et al.*, 2016). Thus the change in the solvation pressure by 2–3 MPa should produce changes in the elastic moduli of the rock. If reduction of the moduli with increasing RH is caused by changing solvation pressure, then this

change in the moduli should be consistent with the variations in the moduli obtained from ultrasonic measurements. To predict variations in the elastic moduli resulting from the change in the solvation pressure, I use the dependence of the elastic moduli of the Bentheim sandstone on the effective pressure measured on a sister sample at room humidity, RH = 46% (Figure 34). The effective pressure for elastic moduli is a linear combination of the hydrostatic confining pressure  $p_c$ , and the pore pressure  $p_p$ :

$$p_{eff} = p_c - np_p, \quad (40)$$

where  $n$  is the effective pressure coefficient. For elastic moduli of a monomineralic isotropic rock,  $n = 1$  (Berryman, 1992; Gurevich, 2004). The elastic moduli as functions of the effective pressure are measured in a triaxial cell using ultrasonic transducers (e.g., Lebedev *et al.*, 2013) with  $p_p = 0$  and  $p_c$  varying from 1 to 60 MPa. In Figure 34, these moduli are plotted against the effective pressure  $p_{eff} = p_c$ . On the same plot, I show moduli measured during the sorption experiments at ambient pressure versus the effective pressure calculated using an equation,

$$p_{eff} = -\Delta p_f, \quad (41)$$

where  $\Delta p_f$  as a function of RH (obtained from adsorption-induced deformation using equation (17)) is shown in Figure 33, and  $p_c = 0$ . As mentioned before, I have chosen the measurements at RH = 46% as the reference state for the sorption experiments. This ensures that at  $p_{eff} = 0$ , the samples in both the adsorption and the triaxial experiments have the same absolute magnitude of solvation pressure corresponding to RH = 46%.

Figure 34 shows two sets of moduli obtained from ultrasonic measurements. The empty symbols show moduli measured as a function of confining pressure at constant humidity, while the solid symbols show moduli measured against RH at zero confining pressure, and the corresponding effective pressure is obtained from the solvation pressure, which is in turn estimated from adsorption-induced deformation measured as a function of RH. Both bulk and shear moduli obtained from triaxial and sorption experiments show broadly similar trends at low effective pressures. The broad consistency between the two sets of measurements confirms that the variations in the moduli with RH can be explained by changes in the solvation pressure.

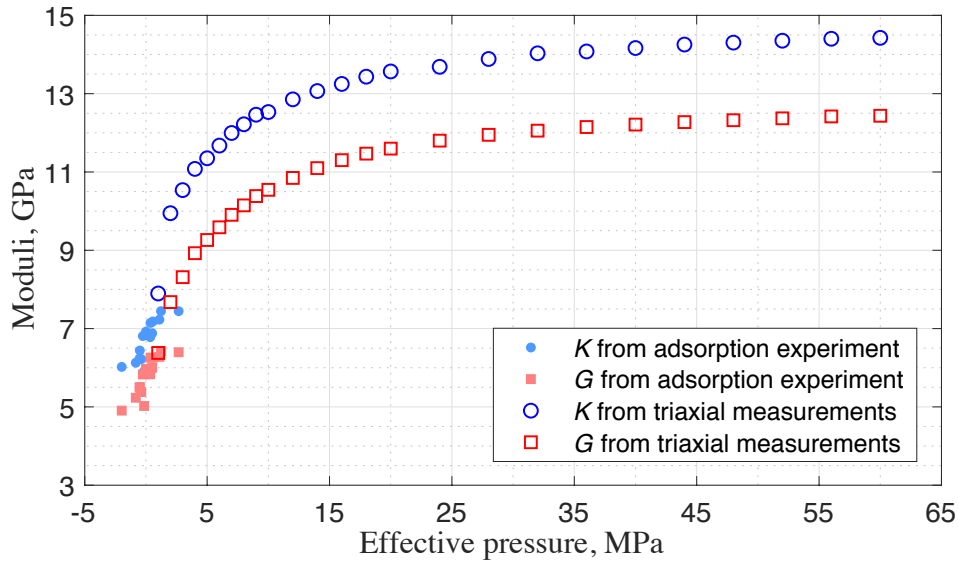


**Figure 34** Dependence of the bulk  $K$  and shear  $G$  moduli on applied effective pressure for Bentheim sandstone measured in this study from the sorption experiment and ultrasonic measurements in a triaxial cell.

The two trends are broadly consistent but not precisely. The discrepancy is greater for the bulk than for the shear modulus. I suggest two possible reasons for the mismatch: 1) influence of the squirt effect (Mavko and Jizba, 1991; Gurevich *et al.*, 2010) on elastic moduli with RH variation and 2) calculation of the effective pressure using equations 37 and 41.

In order to explain how these issues can influence the results and interpretation of the experiments, I first discuss the role of the microstructure of the sandstone sample in adsorption-induced deformation and weakening. An understanding of this role can be gained by comparing the behaviour of the elastic moduli of the Bentheim sandstone versus RH against the behaviour of a Vycor glass exhibiting adsorption-induced deformation of a similar order of magnitude. The results reported in this study qualitatively differ from those reported for nanoporous Vycor glass (Page *et al.*, 1995; Schappert and Pelster, 2014). Pores in Vycor have a worm-like structure, 6–8 nm in diameter. The shear modulus of Vycor glass is independent of RH in the entire range of RH between 0 and 100%. The bulk modulus is independent of RH until the capillary condensation point, where the fluid fully saturates the capillary. This suggests that the adsorbed fluid film on the surface of the pores has no effect on its moduli until the fluid completely fills the nanopores.

In contrast, the response of the elastic properties of a porous granular rock, such as Bentheim sandstone, to changing humidity is different. As observed in the experiment, both the bulk and shear elastic moduli of sandstones decrease with adsorption of small amounts of water. As in Vycor, a film of water adsorbed on the surface of stiff macropores in a sandstone cannot have a significant effect on the elastic moduli. However, sandstones are known to also contain highly compliant crack-like pores at grain-to-grain contacts, with diameters of the order of 0.1 mm and aspect ratios of the order of  $10^{-4} - 10^{-3}$  (and, hence, with nano-scale thickness). Furthermore, these compliant pores are known to control the stress dependency of elastic moduli (Walsh, 1965; Zimmerman 1991; Shapiro, 2003). Adsorption of water in these nanopores creates the solvation pressure, which in turn has a drastic effect on the stiffness of these contacts and hence the overall moduli of the rock.

Another possible cause of the water weakening is the swelling of clays. It has been previously reported that the presence of clay in sandstones can also lead to elastic weakening with an increase of RH. For example, Clark *et al.* (1980) attributed the elastic weakening effect to the hydration and swelling of clay, which led to a decrease in the stiffness of the rock. However, for this study I selected very clean Bentheim sandstone that contains only 3% of kaolinite, which does not tend to swell with hydration. Moreover, Hardin and Richart (1963) observed a similar weakening effect of the same order of magnitude in unconsolidated Ottawa sand, which has no clay. This issue was discussed by Murphy (1982), who has questioned the mechanism of elastic weakening caused by swelling clay and suggested that another more general mechanism must be sought. Therefore, I suggest that the observed phenomenon is the result of the adsorption of water in nano-scale compliant pores at grain contacts.

The presence of water in compliant pores means that the elastic moduli can also be affected by so-called squirt flow. Indeed, all the measurements reported in this paper are made at ultrasonic frequencies. At these frequencies there is usually not enough time for the fluid pressure to equilibrate between stiff and compliant pores, which means that wet inter-granular contacts (compliant pores) are much stiffer than in a vacuum-dry state; this effect is known as squirt flow. Arguably, the higher the RH, the higher the increase of the moduli due to the squirt effect. This effect of RH on the moduli is the opposite to that of the solvation pressure, and may be one reason for a reduction of the slope of the dependency of the moduli on the

changes in the solvation pressure. This hypothesis is consistent with the behaviour of the attenuation estimates (Figure 32), which show a nearly linear increase with increasing RH. However, stiffening of grain contacts due to the squirt flow tends to drastically reduce the stress dependency of the moduli. Our measurements show that at room RH this dependency is quite strong (Figure 34). This suggests that only a fraction of compliant pores are fully saturated with water.

If this is true, then equations 37 and 41 can give an inaccurate estimation of the effective pressure, because they imply full saturation of the pores and equilibrated fluid pressure in the pore space. In real rocks, the compliant pores usually exhibit a broad distribution of sizes. An adsorbing fluid fills smaller pores first, thus the situation where only a fraction of compliant pores is fully saturated is likely. Moreover, even in fully saturated compliant pores, the solvation pressure can be spatially variable, because its magnitude depends on the size of the pore (Gor and Bernstein, 2016). Therefore, using equations 37 and 41, I do not translate the observed deformation into the effective pressure precisely, but I estimate the order of magnitude of the solvation pressure and effective pressure, which seem reasonable.

#### **4.5 Conclusions**

I have designed an experimental setup for simultaneous measurements of the deformation and ultrasonic velocities of rocks in different hydration states. I measured variations in the elastic properties of a Bentheim sandstone sample with changing RH at adsorption and desorption. The measurements were complemented with estimation of the saturation of the sample. The experimental results showed that adsorption of water leads to elastic weakening of the sandstone, and both P- and S-waves were affected by RH variations. Additionally, I observed an increase in the attenuation of elastic waves and a stretching of the sample with strain of the order of  $10^{-4}$ . Desorption of water led to an increase in the elastic moduli, decrease of attenuation, and shrinkage of the sample. I observed a significant change in the elastic moduli with RH variations from 13 to 97%. This result is important for laboratory measurements of the elastic properties of dry rocks, which are usually done at room conditions. For example, variations in the RH in a room can be from 30 to 60%. For the Bentheim sandstone, such RH variations correspond to changes in the bulk and shear moduli of 0.5 and 0.75 GPa, respectively. These changes can

noticeably affect the predictions of rock physics theories and have to be taken into account.

The results obtained on the Bentheim sandstone sample in this study were compared to dependencies of the deformation and elastic moduli on RH previously reported for nanoporous Vycor glass. The qualitative difference between these results indicates that the microstructure of the material plays a crucial role in the changes in the elastic properties with sorption. I have proposed and tested a hypothesis that adsorption-induced elastic weakening and deformation of the Bentheim sandstone are governed by the increasing pressure of the fluid confined in compliant nanopores at grain contacts.

From the measured sorption-induced deformation, I have estimated that the magnitude of the fluid pressure in such pores is of several megapascals. Further, I have measured the dependencies of the elastic moduli of the Bentheim sandstone on confining pressure in a triaxial cell at room humidity. I compared the results of the triaxial measurements with variations in the elastic properties caused by RH change. The broad agreement between the two sets of measurements and the reasonable magnitude of the estimated fluid pressure in compliant pores confirm that the moduli variations with RH can be explained by changes in the solvation pressure.

The outcomes of the performed analysis can be translated to the elastic behaviour of compliant porosity with changes in hydration in other, structurally more complicated rocks, like shales.

## Chapter 5. Thesis conclusions

The main objective of this project is to study the effect of changing water content on the elastic properties of shales and sandstones. The project comprises development of an experimental setup, obtaining new experimental data and analysis of these data. The experimental part of the project involved ultrasonic measurements of the elastic properties of shales and sandstones in different hydration states. Hydration of the samples was controlled by maintaining the samples in an atmosphere with constant relative humidity (RH). The mechanism of changing hydration of the samples is based on sorption phenomenon, which was invoked by a change in RH. A decrease in RH leads to the desorption of water from samples, and an increase in RH leads to adsorption. This process is usually fast for sandstones, but extremely time-consuming for shales due to their low permeability and small pore size. The larger the sample, the more time is needed for the stabilisation of sorption processes in shales. For example, stabilisation of sorption processes takes several months for samples of a standard cylindrical shape (38 mm in diameter and ~50 mm in length), which are conventionally used for ultrasonic measurements. Therefore, in the first stage of the project, I designed and validated the experimental technique of measuring the ultrasonic velocities of samples of ~15 mm thickness under stress. Developing this technique significantly reduced the duration of the experiments on shales and allowed me to collect comprehensive experimental data.

The elastic properties of shales were measured on Opalinus shale samples under hydrostatic confining pressure in a range from 2 to 50 MPa. These data were complemented with analysis of microstructural variations caused by changing the hydration in the shale. I observed that drying of the shale led to shrinkage of the samples in the direction normal to the bedding plane, while only a subtle change in shape in the in-plane direction was observed. I also studied the pore structure of the Opalinus shale at different hydration states using laboratory measurements of mass and densities as well as X-ray micro computed tomography analysis. The X-ray imaging showed that macroporosity (size  $>1 \mu\text{m}$ ) constituted less than 5% of the total porosity and barely changed with drying or rehydration. In contrast, the total porosity in the Opalinus shale reduced with drying from 13.6% in the preserved state to

11.8% in the driest state (obtained with RH = 13%). The observed microstructural changes were broadly consistent with the data reported in previous studies.

Conversely, the results of ultrasonic measurements showed no agreement with data reported in previous studies. I observed that the in-plane compressional modulus  $C_{11}$  increases with drying, while the cross-plane compressional modulus  $C_{33}$  decreases. Both shear moduli  $C_{44}$  and  $C_{66}$  exhibited a strong increase by a factor of 1.5–2 with drying from preserved to the driest state. The rehydration of the samples in the atmosphere with RH = 97% led to decrease of  $C_{11}$ ,  $C_{44}$  and  $C_{66}$  to values lower than in the preserved state. The  $C_{33}$ , on the contrary, increased with rehydration, but did not recover to the initial value exhibited in the preserved state. Moreover, measurements under confining pressure showed that the moduli are stress-dependent, which indicated the presence of compliant porosity in the shale. The characteristics of this compliant porosity were analysed later in Chapter 3 with the use of a theoretical rock physics model. The obtained unique set of experimental data combined with the results of previous studies formed a basis for the analysis of the reasons and driving mechanisms for the observed behaviour.

I identified four possible driving mechanisms for the observed behaviour of the elastic properties of shales with changing hydration: 1) variation in the total porosity, which was clearly observed in the experiments; 2) substitution of pore-filling fluid as a result of the adsorption or desorption of water in pores; 3) change in stiffness of the contacts between clay particles indicated by the measured stress-dependency of elastic moduli; and 4) chemical hardening/softening of clay particles. I used differential effective medium theory to estimate how the observed change in porosity and fluid substitution could affect the elastic moduli of the shale. The results of the modelling demonstrate that these two processes have the opposite effect on the moduli and could result in the opposite trends for  $C_{11}$  and  $C_{33}$  with hydration. However, these two effects cannot explain the drastic increase of the shear moduli with drying. The behaviour of  $C_{44}$  and  $C_{66}$  with changing hydration could be a result of a changing stiffness of compliant porosity constituted by microfractures and contacts between clay aggregates or clay particles. The measured stress sensitivity of the elastic moduli in the shale samples at different hydration states indicated that compliant pores became softer with the adsorption of water. Additionally, chemical hardening/softening of clay particles with the desorption/adsorption of water could also affect the elastic properties of clay-containing rocks. This effect was

demonstrated in a set of recent studies on molecular dynamics simulations of the elastic behaviour of clays at an atomic scale. These results provided an important insight into the effect of changing the hydration of clay-containing rocks. A thorough investigation of how these data can be upscaled and implemented in rock physics models is needed.

The theoretical analysis of the experimental data revealed the importance of the effect of changing hydration on the stiffness of compliant porosity, and hence the elastic properties of the rock. In sandstones, the hydration (saturation) effect on elastic properties is reasonably well understood, except the case of low saturations, when adsorption of a small amount of water leads to a decrease of both P- and S-wave velocities. I assumed that the reasons for the observed elastic weakening of sandstones could be similar to those that led to a drastic decrease of S-wave velocities with the hydration of shales. Therefore, in order to improve our understanding of this phenomenon I have explored the effect of low saturation (controlled by air humidity) on the elastic properties of Bentheim sandstones. The measurements of the dependencies of sandstone's elastic properties on changing hydration were complemented with measurements of concurrent deformation of the rock. I observed ~15% change in the P- and S-wave velocities with the transition of the sample from the driest (13% RH,  $s = 0.1\%$ ) to the wettest state (97% RH,  $s = 1.5\text{--}2\%$ ). Additionally, I observed an increase of the attenuation of elastic waves and a stretching of the sample with the strain of the order of  $10^{-4}$ . Desorption of water led to an increase of the elastic moduli, decrease of attenuation and shrinkage of the sample.

I considered the hypothesis that water adsorbed as a thin film on the surface of grains saturates fully only nano-scale compliant pores or grain-to-grain contacts and leads to an increase of pressure in fluid in such compliant pores, resulting in deformation and a decrease of elastic properties of the rock. I have estimated that the magnitude of fluid pressure (solvation pressure), which can cause deformation of the order of  $10^{-4}$  should be of several MPa. I compared the measured elastic moduli related to the estimated solvation pressure with the stress dependency of the elastic properties of the Bentheim sandstone measured in a triaxial cell. The broad agreement of the two sets of data confirmed that variations of the elastic properties with changing RH could be explained by changes in the solvation pressure (i.e. stiffness) of compliant pores.

This research project provided a unique set of experimental data. The analysis of these data contributed to an improved understanding of the effects of changing hydration on the elastic properties and microstructure of shales and sandstones. I presented and discussed discrepancies in the experimental data reported in this project and in previous studies for different shales. The discrepancies implied that the effect of hydration on elastic properties is a complex phenomenon involving different and counteracting driving mechanisms for variation of the elastic properties of shales. Depending on the microstructure and composition of rocks, the superposed impact of the various driving factors can result in different trends for the elastic moduli with changing hydration in different samples.

One of the crucial driving factors affecting the elastic properties of rocks with variations in hydration is a changing stiffness of compliant porosity. This was confirmed by analysis of the experimental data obtained on Opalinus shale. Additionally, a similar effect was observed in Bentheim sandstone. The elastic properties of the sandstone strongly depend on the amount of water adsorbed in nano-scale compliant porosity located at the contacts between grains. In Opalinus shale, the amount of nano-scale porosity is higher as it comprises 95% of the total porosity. Thus, for example, the effects of the elastic weakening of S-wave velocities are stronger than those in the Bentheim sandstone. Therefore, the elastic weakening phenomenon in shales and sandstones seems to be of a similar nature, caused by the changing stiffness of compliant pores.

The reported results can potentially be combined in a comprehensive rock physics model describing the observed phenomena with high accuracy. Eventually, this work has the potential to improve seismic and well-log interpretation and reservoir characterisation.

## List of figures

Figure 1 PMMA, Berea sandstone, Bentheim sandstone, and Opalinus shale samples. Standard samples, 60 mm long, were used for experimental measurements first. Then 15 mm long thin-disc samples were cut out of the standard plugs. The Opalinus shale sample shown in the figure is before cutting..... 23

Figure 2 Left: schematic of the arrangement of the experimental equipment: T, transducer; P, PEEK piston; and S, sample. Setups 1 and 2 at the top right corner show the standard and thin disc samples, respectively, placed between short and long PEEK pistons. Right: image of the apparatus: the Hoek cell (1), the steel frame of the rig (2), the hydraulic actuator (3), the transducers (4), and the PEEK pistons (5)..... 23

Figure 3 The example of experimentally obtained waveforms on a setup with a standard dry Berea sandstone. The red vertical lines show the determined arrivals of the P- and S-waves. .... 25

Figure 4 a) A cross-section of the 3D model of the standard aluminium sample. b) The input pulse. c) An example of meshing..... 27

Figure 5 The results of FEM modelling of the propagation of elastic waves through the standard aluminium sample. The figure shows the cross-section of the sample made through its vertical axis of symmetry in the XY plane, the plane of the shear transducers polarity. Two components of the displacement of nodes and their total magnitude are shown in the first, second and third rows, respectively. Three vertical columns show these parameters at three sequential moments in time. The fronts of the P-wave dipole and the S-wave are highlighted. .... 28

Figure 6 Example of the displacement field at the bottom part of the standard aluminium sample when the compressional dipole reaches the receiver transducer. 29

Figure 7 Experimental (blue) and simulated (red) waveforms of the ultrasonic signal passed through the standard aluminium sample. Primary (V) and secondary (nm) vertical axes are used for experimental and simulated waveforms, respectively. The amplitude of the simulated waveform relates to the average shear displacement of the nodes in the area of the receiver. At the right: magnified section of the waveforms corresponding to the first arrivals. .... 30

Figure 8 Measured  $V_P$  and  $V_S$  on the set of standard and thin samples made of four different materials. Experimental errors are shown for measurements on thin

samples. Shear velocity  $V_s$  of the Opalinus shale is the velocity of the S-wave propagating and polarised in the bedding plane. .... 33

Figure 9 The Abaqus models built for static stress distribution modelling. The models are full 3D copies of the experimental setups. Figure shows half of the models cut by vertical plane along the main axis. The PEEK pistons are green, the tested samples are grey. The areas with applied boundary conditions are highlighted with red colour.  $S_a^{top}$  is the area, where the axial stress  $P_{axial}$  is applied;  $S_r$  is the area, where the radial stress  $P_{radial}$  is applied;  $S_a^{bot}$  is the fixed area, where the motion of particles in a vertical direction is restricted, simulating a rigid surface underneath the setup. All dimensions are in millimetres. a) The setup with a standard sample. b) The setup with a thin sample. c) Hexahedral meshing of the models..... 34

Figure 10 Modelling of the static stress distribution inside the experimental setups. The applied hydrostatic pressure is equal to 50 MPa. Equivalent pressure stress  $p = -(\sigma_{11} + \sigma_{22} + \sigma_{33}) / 3$  is colour-coded,  $\sigma_{11}$ ,  $\sigma_{22}$ ,  $\sigma_{33}$  are the diagonal components of the stress tensor. a) The setup with a standard Berea sandstone sample. b) The setup with a thin Berea sandstone sample. c) Rescaled stress fields inside the thin and standard samples..... 37

Figure 11 Relative differences between applied pressure and averaged stress in a central part of the samples, calculated from data reported in Table 2. .... 39

Figure 12  $V_p$  and  $V_s$  measured on the standard Berea and Bentheim sandstone samples versus corrected  $V_p$  and  $V_s$  obtained on thin samples. Experimental errors are shown for measurements on thin samples. Solid lines represent velocities measured on thin disc samples before introduced correction. .... 39

Figure 13 Results of the numerical modelling of stress redistribution inside Berea sandstone samples of different lengths. Equivalent pressure stress  $p = -(\sigma_{11} + \sigma_{22} + \sigma_{33}) / 3$  is colour-coded;  $\sigma_{11}$ ,  $\sigma_{22}$ ,  $\sigma_{33}$  are diagonal components of the stress tensor..... 40

Figure 14 Modelling of static stress distribution inside the experimental setups with aluminium pistons instead of PEEK parts. The applied hydrostatic pressure is equal to 50 MPa. Equivalent pressure stress  $p = -(\sigma_{11} + \sigma_{22} + \sigma_{33}) / 3$  is colour-coded;  $\sigma_{11}$ ,  $\sigma_{22}$ ,  $\sigma_{33}$  are diagonal components of the stress tensor. a) The setup with a standard Berea sandstone sample. b) The setup with a thin Berea sandstone sample. c) Rescaled stress fields inside the thin and standard samples..... 42

Figure 15 Scanning electron microscope (SEM) image of the Opalinus shale. Black colour shows pores and fractures, dark grey denotes clay matrix, light grey and white colours show silt inclusions like quartz (light-grey) and calcite (white). The white arrows indicate the bedding plane..... 48

Figure 16 The schematic of the drying/rehydration experiment. The desiccators are labelled with RH maintained inside. Continuous mass control is performed. Ultrasonic measurements are done after equilibration of sorption processes. .... 49

Figure 17 The sample for micro computed tomography ( $\mu$ CT) inside a mini-desiccator constructed to keep RH constant during scanning: schematic (left) and photo (right). .... 50

Figure 18 Micro computed tomography ( $\mu$ CT) images of the same area of the Opalinus shale sample at dry state obtained in the atmosphere with 13% relative humidity (RH) (left) and wet state after 97% RH atmosphere (right). The images show 2D slices of the 3D volume cut perpendicular to the bedding plane (indicated by white arrows). The pink arrows indicate the distance between pairs of the most prominent features on the scans, such as dense grains of quartz or calcite. These features are clearly visible on the images as white spots. Thus it is convenient to use them as markers for the measurement of the distance. .... 53

Figure 19 Histograms showing distribution of pores by their shape. The pores are approximated with oblate ellipsoids. The aspect ratio is the ratio of the shortest to the longest axes of ellipsoids. .... 53

Figure 20 The components of elastic stiffness tensor and Thomsen's (1986) anisotropy parameters measured in the Opalinus shale samples at different hydration states. Labels under the data points indicate the relative humidity (RH) corresponding to each hydration state (Pr indicates a shale in preserved state). The black arrows show the scheme of desiccation. The applied hydrostatic confining pressure is colour coded..... 56

Figure 21 Variations in the elastic moduli of the Opalinus shale samples at different hydration states normalised to the moduli values at the maximum applied pressure of 50 MPa. The water mass fraction is colour coded. .... 57

Figure 22 The scheme of the modelling of the effect of changing porosity and fluid substitution on the elastic properties of Opalinus shale in different hydration states. The model has two fitting parameters  $\alpha$  and  $\delta$ . .... 63

Figure 23 Differential effective medium (DEM) modelling of drying-induced variations of the elastic properties caused by reduction of the total porosity and fluid substitution. Square red markers show the experimentally measured moduli at hydrostatic confining pressure of 2 MPa. The initial point for modelling is the moduli of the shale in the preserved state. The aspect ratio of pores is colour coded. The labels next to the modelling curves show used anisotropy parameter $\delta$ . No label means $\delta = 0.35$ .	64
Figure 24 The experimentally measured compliances (circles) and the results of the fitting (lines) using the model of Pervukhina <i>et al.</i> (2011) for Opalinus shale at different hydration states (shown by labels at the top).	68
Figure 25 Dependence of elastic moduli of clay composites comprised of Na-montmorillonite clay particles on the thickness of water layer between clay platelets (Basal Spacing). The blue data points represent the composite with fully aligned clay particles, of which the elastic properties are reported in Ebrahimi <i>et al.</i> (2011). The green data points represent the composite with random (isotropic) distribution of clay particles ( $C_{11} = C_{33}$ , $C_{44} = C_{66}$ , $C_{13} = C_{11} - 2C_{66}$ ). The red data points represent the composite comprised of clay particles oriented according to the orientation distribution function (ODF), $W(\theta)$ , from Beloborodov <i>et al.</i> (2016), which is shown in the bottom right corner.	70
Figure 26 Top: schematic of the experimental setup for measurements of sorption-induced deformation and variations in the elastic properties of rocks. Bottom: image of the experimental setup.	78
Figure 27 Readings from the strain gauge and the data logger for the adsorption process with 97% RH potassium sulfate desiccant.	79
Figure 28 a) Deformation of the primary sample versus relative humidity (RH). The black arrows show the direction of the sorption process. b) Estimation of saturation ( $V_{fluid} / V_{pore}$ ) versus RH done on the sister sample, where the size of the markers represents an experimental error. The filled markers represent adsorption data; the hollow markers represent desorption data.	81
Figure 29 Waveforms recorded at different relative humidity (RH) split into two parts: a) P-wave; b) S-wave. Note the change of vertical scale. c) Frequency spectra of transmitted ultrasonic pulses at different RH. RH is colour-coded. Dashed lines represent waveforms recorded at desorption path; the solid lines represent an adsorption path.	82

Figure 30 a) Dependence of the P- and S-wave velocities on relative humidity (RH) at desorption and adsorption paths. b) Dependence of the bulk $K$ and shear $G$ moduli on RH at desorption and adsorption paths.....	83
Figure 31 Frequency spectra of P-wave and S-wave signals at different hydration states. Relative humidity (RH) is colour-coded. The dashed lines represent the desorption path; the solid lines represent the adsorption path. ....	84
Figure 32 Variation in attenuation in the sandstone versus relative humidity (RH), $Q_{ref} = 300$ at RH = 13%. ....	85
Figure 33 Variations in the solvation pressure as a function of relative humidity (RH) estimated from equation 37. The reference state, where $\Delta p_f = 0$ , is the state with room RH. ....	86
Figure 34 Dependence of the bulk $K$ and shear $G$ moduli on applied effective pressure for Bentheim sandstone measured in this study from the sorption experiment and ultrasonic measurements in a triaxial cell. ....	88

## List of tables

Table 1 Stress-dependent properties of rocks and materials used for modelling. ....	35
Table 2 The average values of $p$ , the first invariant of the stress tensor, in the middle parts of Bentheim and Berea sandstone samples of different lengths. Stress values are in MPa. The standard samples are 60 mm long; the thin samples are 15 mm long. ....	38
Table 3 Characterisation of Opalinus shale at different hydration states. The table reports the mass fraction of water $\omega$ , density $\rho$ , porosity $\phi$ and the saturation $s$ . ....	54
Table 4 Comparison of the experimentally measured behaviour of ultrasonic P- and S-wave velocities with dehydration in different clay-containing rocks. <b>Inc</b> indicates increase of the velocity; <b>Dec</b> indicates decrease of the velocity; <b>NoE</b> indicates no effect of changing hydration on the velocity. N/A means that measurements were not conducted. ....	61
Table 5 Parameters of the model of Pervukhina <i>et al.</i> (2011) used to fit the obtained pressure-dependent elastic properties of the Opalinus shale at different hydration states. ....	68
Table 6 The list of salts used for the sorption experiment with the corresponding range of relative humidity (RH) at room temperature. ....	76
Table 7 Measured velocities of ultrasonic P- and S-waves ( $V_P$ and $V_S$ ) in standard and thin disc samples of PMMA and Berea sandstone. ....	119
Table 8 Measured velocities of ultrasonic P- and S-waves ( $V_P$ and $V_S$ ) in standard and thin disc samples of Bentheim sandstone and Opalinus shale. In the case of Opalinus shale, $V_P$ and $V_S$ are the velocities of elastic waves propagating and polarised along the bedding plane. ....	120
Table 9 Measured elastic properties of the Opalinus shale in the preserved state. ....	121
Table 10 Measured elastic properties of the Opalinus shale in the hydration state obtained in the atmosphere with 52% relative humidity. ....	121
Table 11 Measured elastic properties of the Opalinus shale in the hydration state obtained in the atmosphere with 31% relative humidity. ....	122

Table 12 Measured elastic properties of the Opalinus shale in the hydration state obtained in the atmosphere with 13% relative humidity. .... 122

Table 13 Measured elastic properties of the Opalinus shale in the hydration state obtained in the atmosphere with 97% relative humidity. .... 123

Table 14 The components of the stiffness tensor  $C^{matrix}$  obtained at the first step of the modelling (section 3.3) depending on the used parameters  $\alpha$  and  $\delta$ ..... 123

## References

Akram, J., and D. W. Eaton, 2016, A review and appraisal of arrival-time picking methods for downhole microseismic data: *Geophysics*, **81**(5), KS67–KS87, <https://doi.org/10.1190/geo2015-0261.1>.

Amberg, C. H., and R. McIntosh, 1952, A study of adsorption hysteresis by means of length changes of a rod of porous glass: *Canadian Journal of Chemistry*, **30**(12), 1012–1032, <https://doi.org/10.1139/v52-121>.

ASTM International, 2008, D 2845-08 standard test method for laboratory determination of pulse velocities and ultrasonic elastic constants of rock, <http://www.astm.org/Standards/D2845.htm>, accessed 2 October 2017.

ASTM International, 2014, D 7012-14 standard test methods for compressive strength and elastic moduli of intact rock core specimens under varying states of stress and temperatures, <http://www.astm.org/Standards/D7012.htm>, accessed 2 October 2017.

Bangham, D. H., and N. Fakhoury, 1928, The expansion of charcoal accompanying sorption of gases and vapours: *Nature*, **122**(3079), 681–682, <https://doi.org/10.1038/122681b0>.

Bangham, D. H., and R. I. Razouk, 1938, The saturation and immersion expansions and the heat of wetting: *Proceedings of the Royal Society. Series A, Mathematical and Physical Sciences*, **166**, 572, <https://doi.org/10.1098/rspa.1938.0112>.

Batzle, M., and Z. Wang, 1992, Seismic properties of pore fluids: *Geophysics*, **57**(11), 1396–1408, <https://doi.org/10.1190/1.1443207>.

Bauer, A., M. H. Bhuiyan, E. Fjær, R. M. Holt, S. Lozovyi, M. Pohl, and D. Szcwcyk, 2016, Frequency-dependent wave velocities in sediments and sedimentary rocks/laboratory measurements and evidences: *The Leading Edge*, **35**(6), 490–494, <https://doi.org/10.1190/tle35060490.1>.

Beloborodov, R., M. Pervukhina, V. Luzin, C. Delle Piane, M. B. Clennell, S. Zandi, and M. Lebedev, 2016, Compaction of quartz-kaolinite mixtures: the influence of the pore fluid composition on the development of their microstructure and elastic anisotropy: *Marine and Petroleum Geology*, **78**, 426–438, <https://doi.org/10.1016/j.marpetgeo.2016.09.030>.

Benson, P. M., P. G. Meredith, E. S. Platzman, and R. E. White, 2005, Pore fabric shape anisotropy in porous sandstones and its relation to elastic wave velocity and permeability anisotropy under hydrostatic pressure: *International Journal of Rock Mechanics and Mining Sciences*, **42**(7–8), 890–899, <https://doi.org/10.1016/j.ijrmms.2005.05.003>.

Berryman, J. G., 1980, Confirmation of Biot's theory: *Applied Physics Letters*, **37**(4), 382–384, <https://doi.org/10.1063/1.91951>.

Berryman, J. G., 1992, Effective stress for transport properties of inhomogeneous porous rock: *Journal of Geophysical Research*, **97**(B12), 17409–17424, <https://doi.org/10.1029/92JB01593>.

Berryman, J. G., 1999, Origin of Gassmann's equations: *Geophysics*, **64**(5), 1627–1629, <https://doi.org/10.1190/1.1444667>.

Berryman, J. G., V. Y. Grechka, and P. A. Berge, 1999, Analysis of Thomsen parameters for finely layered VTI media: *Geophysical Prospecting*, **47**(6), 959–978, <https://doi.org/10.1046/j.1365-2478.1999.00163.x>.

Berryman, J. G., and G. W. Milton, 1991, Exact results for generalized Gassmann's equation in composite porous media with two constituents: *Geophysics*, **56**(12), 1950–1960, <https://doi.org/10.1190/1.1443006>.

Beucher, S., and C. Lantuéjoul, 1979, Use of watersheds in contour detection: *Proceedings of International Workshop on Image Processing, Real-Time Edge and Motion Detection/Estimation*, Rennes, France.

Beucher, S., and F. Meyer, 1993, The morphological approach to segmentation: the watershed transformation, *in* E. R. Dougherty, ed., *Mathematical Morphology in Image Processing*, Marcel Dekker, Inc., 433–481.

Biot, M. A., 1956a, Theory of propagation of elastic waves in a fluid-saturated porous solid. I. Low-frequency range: *The Journal of the Acoustical Society of America*, **28**(2), 168–178, <https://doi.org/10.1121/1.1908239>.

Biot, M. A., 1956b, Theory of propagation of elastic waves in a fluid-saturated porous solid. II. Higher frequency range: *The Journal of the Acoustical Society of America*, **28**(2), 179–191, <https://doi.org/10.1121/1.1908241>.

Biot, M. A., 1962, Mechanics of deformation and acoustic propagation in porous media: *Journal of Applied Physics*, **33**(4), 1482–1498, <https://doi.org/10.1063/1.1728759>.

Birch, F., 1960, The velocity of compressional waves in rocks to 10 kilobars, part 1: *Journal of Geophysical Research*, **65**(4), 1083–1102, <https://doi.org/10.1029/JZ065i004p01083>.

Blake, O. O., D. R. Faulkner, and A. Rietbrock, 2012, The effect of varying damage history in crystalline rocks on the P- and S-wave velocity under hydrostatic confining pressure: *Pure and Applied Geophysics*, **170**(4), 493–505, <https://doi.org/10.1007/s00024-012-0550-0>.

Boissiere, C., D. Grosso, S. Lepoutre, L. Nicole, A. B. Bruneau, and C. Sanchez, 2005, Porosity and mechanical properties of mesoporous thin films assessed by environmental ellipsometric porosimetry: *Langmuir*, **21**(26), 12362–12371, <https://doi.org/10.1021/la050981z>.

Briggs, H., and R. Sinha, 1934, V.–Expansion and contraction of coal caused respectively by the sorption and discharge of gas: *Proceedings of the Royal Society of Edinburgh*, **53**, 48–53, <https://doi.org/10.1017/S0370164600015480>.

Brown, R. J. S., and J. Korringa, 1975, On the dependence of the elastic properties of a porous rock on the compressibility of the pore fluid: *Geophysics*, **40**(4), 608–616, <https://doi.org/10.1190/1.1440551>.

Cadoret, T., 1993, Effet de la saturation eau/gaz sur les propriétés acoustiques des roches: Ph.D. dissertation, University of Paris, VII.

Carrier, B., M. Vandamme, R. J.-M. Pellenq, and H. Van Damme, 2014, Elastic properties of swelling clay particles at finite temperature upon hydration: *The Journal of Physical Chemistry*, **118**(17), 8933–8943, <https://doi.org/10.1021/jp412160e>.

Charlez, P. A., 1991, *Rock mechanics: Theoretical fundamentals*: Éditions Technip, 163.

Cheng, C. H., and D. V. Johnston, 1981, Dynamic and static moduli: *Geophysical Research Letters*, **8**(1), 39–42, <https://doi.org/10.1029/GL008i001p00039>.

Christensen, N. I., and H. F. Wang, 1985, The influence of pore pressure and confining pressure on dynamic elastic properties of Berea sandstone: *Geophysics*, **50**(2), 207–213, <https://doi.org/10.1190/1.1441910>.

Ciz, R., and S. A. Shapiro, 2009, Stress-dependent anisotropy in transversely isotropic rocks: Comparison between theory and laboratory experiment on shale: *Geophysics*, **74**(1), D7–D12, <https://doi.org/10.1190/1.3008546>.

Clark, V. A., B. R. Tittmann, and T. W. Spencer, 1980, Effect of volatiles on attenuation ( $Q^{-1}$ ) and velocity in sedimentary rocks: *Journal of Geophysical Research: Solid Earth*, **85**(B10), 5190–5198, <https://doi.org/10.1029/JB085iB10p05190>.

Coyner, K. B., 1984, Effects of stress, pore pressure, and pore fluids on bulkstrain, velocity, and permeability in rocks: Ph.D. thesis, Massachusetts Institute of Technology.

Dell Piane, C., J. Sarout, C. Madonna, E. H. Saenger, D. N. Dewurst, and M. Raven, 2014, Frequency-dependent seismic attenuation in shales: Experimental results and theoretical analysis: *Geophysical Journal International*, **198**(1), 504–515, <https://doi.org/10.1093/gji/ggu148>.

Dellinger, J., and L. Vernik, 1994, Short note: Do traveltimes in pulse-transmission experiments yield anisotropic group or phase velocities?: *Geophysics*, **59**(11), 1774–1779, <https://doi.org/10.1190/1.1443564>.

De Meersman, K., M. Kendall, and M. Van der Baan, 2009, The 1998 Valhall microseismic data set: An integrated study of relocated sources, seismic multiplets, and S-wave splitting: *Geophysics*, **74**(5), B183–B195, <https://doi.org/10.1190/1.3205028>.

De Paula, O., M. Pervukhina, D. Makarynska, and B. Gurevich, 2012, Modeling squirt dispersion and attenuation in fluid-saturated rocks using pressure dependency of dry ultrasonic velocities: *Geophysics*, **77**(3), WA157–WA168, <https://doi.org/10.1190/geo2011-0253.1>.

Dewhurst, D. N., and A. F. Siggins, 2006, Impact of fabric, microcracks and stress field on shale anisotropy: *Geophysical Journal International*, **165**(1), 135–148, <https://doi.org/10.1111/j.1365-246X.2006.02834.x>.

Dolino, G., D. Bellet, and C. Faivre, 1996, Adsorption strains in porous silicon: *Physical Review B*, **54**(24), 17919–17929, <https://doi.org/10.1103/>

Domenico, S. N., 1976, Effect of brine-gas mixture on velocity in an unconsolidated sand reservoir: *Geophysics*, **41**(5), 882–894, <https://doi.org/10.1190/1.1440670>.

Dvorkin, J. and A. Nur, 1993, Dynamic poroelasticity: a unified model with the squirt and the Biot mechanisms: *Geophysics*, **58**(4), 524–533, <https://doi.org/10.1190/1.1443435>.

Dvorkin, J., R. Nolen-Hoeksema, and A. Nur, 1994, The squirt-flow mechanism: Macroscopic description: *Geophysics*, **59**(3), 428–438, <https://doi.org/10.1190/1.1443605>.

Ebrahimi, D., R. J.-M. Pellenq, and A. J. Whittle, 2012, Nanoscale elastic properties of montmorillonite upon water adsorption: *Langmuir*, **28**(49), 16855–16863, <https://doi.org/10.1021/la302997g>.

Ferrari, A., V. Favero, P. Marschall, and L. Laloui, 2014, Experimental analysis of the water retention behaviour of shales: *International Journal of Rock Mechanics and Mining Sciences*, **72**, 61–70, <https://doi.org/10.1016/j.ijrmms.2014.08.011>.

Fjær, E., 2009, Static and dynamic moduli of a weak sandstone: *Geophysics*, **74**(2), WA103–WA112, <https://doi.org/10.1190/1.3052113>.

Fortin, J., Y. Guéguen, and A. Schubnel, 2007, Effects of pore collapse and grain crushing on ultrasonic velocities and  $V_P/V_S$ : *Journal of Geophysical Research*, **112**, B08207, <https://doi.org/10.1029/2005JB004005>.

Fujii, I., and K. Kawashima, 1995, Digital measurement of ultrasonic velocity, *in* D. O. Thompson and D. E. Chimenti, eds, *Review of progress in quantitative nondestructive evaluation*: Springer, 203–209.

Garrouch, A. A., and M. M. Sharma, 1994, The influence of clay content, salinity, stress, and wettability on the dielectric properties of brine-saturated rocks: 10 Hz to 10 MHz: *Geophysics*, **59**(6), 909–917, <https://doi.org/10.1190/1.1443650>.

Gasc-Barbier, M., and D. Tessier, 2007, Structural modifications of a hard deep clayey rock due to hygro-mechanical solicitations: *International Journal of Geomechanics*, **7**(3), 227–235, [https://doi.org/10.1061/\(ASCE\)1532-3641\(2007\)7:3\(227\)](https://doi.org/10.1061/(ASCE)1532-3641(2007)7:3(227)).

Gassmann, F., 1951, Über die elastizität poröser medien: *Vierteljahrsschrift der Naturforschenden Gesellschaft in Zürich*, **96**, 1–23.

Geertsma, J., and D. C. Smit, 1961, Some aspects of elastic wave propagation in fluid-saturated porous solids: *Geophysics*, **26**(2), 169–181, <https://doi.org/10.1190/1.1438855>.

Ghorbani, A., M. Zamora, and P. Cosenza, 2009, Effects of desiccation on the elastic wave velocities of clay-rocks: *International Journal of Rock Mechanics and Mining Sciences*, **46**(8), 1267–1272, <https://doi.org/10.1016/j.ijrmms.2009.01.009>.

Gor, G. Y., and N. Bernstein, 2016, Revisiting Bangham's law of adsorption-induced deformation: Changes of surface energy and surface stress: *Physical Chemistry Chemical Physics*, **18**(14), 9788–9798. <https://doi.org/10.1039/C6CP00051G>.

Gor, G. Y., and B. Gurevich, 2018, Gassmann theory applies to nanoporous media: *Geophysical Research Letters*, **45**(1), 146–155, <https://doi.org/10.1002/2017GL075321>.

Gor, G. Y., P. Huber, and N. Bernstein, 2017, Adsorption-induced deformation of nanoporous materials – A review: *Applied Physics Reviews*, **4**(1), 011303, <https://doi.org/10.1063/1.4975001>.

Gor, G. Y., and A. V. Neimark, 2010, Adsorption-induced deformation of mesoporous solids: *Langmuir*, **26**(16), 13021–13027, <https://doi.org/10.1021/la1019247>.

Greenspan, L., 1977, Humidity fixed points of binary saturated aqueous solutions: *Journal of Research of the National Bureau of Standards, Section A: Physics and Chemistry*, **81A**(1), 89–96, <https://doi.org/10.6028/jres.081A.011>.

Gurevich, B., 2018, A simple derivation of the effective stress coefficient for seismic velocities in porous rocks: *Geophysics*, **69**(2), 393–397, <https://doi.org/10.1190/1.1707058>.

Gurevich, B., D. Makarynska, O. B. de Paula, and M. Pervukhina, 2010, A simple model for squirt-flow dispersion and attenuation in fluid-saturated granular rocks: *Geophysics*, **75**(6), N109–N120, <https://doi.org/10.1190/1.3509782>.

Haines, R. S., and R. McIntosh, 1947, Length changes of activated carbon rods caused by adsorption of vapors: *The Journal of Chemical Physics*, **15**(1), 28–38. <https://doi.org/10.1063/1.1746282>.

Han, D., and M. L. Batzle, 2004, Gassmann's equation and fluid-saturation effects on seismic velocities: *Geophysics*, **69**(2), 398–405. <https://doi.org/10.1190/1.1707059>.

Hardin, B. O., and F. E. Richart Jr., 1963, Elastic wave velocities in granular soils: *Journal of the Soil Mechanics and Foundations Division*, **89**(1), 33–66.

Hashin, Z., and S. Shtrikman, 1963, A variational approach to the elastic behaviour of multiphase materials: *Journal of the Mechanics and Physics of Solids*, **11**(2), 127–140, [https://doi.org/10.1016/0022-5096\(63\)90060-7](https://doi.org/10.1016/0022-5096(63)90060-7).

Helbig, K., 1983, Elliptical anisotropy – its significance and meaning: *Geophysics*, **48**(7), 825–832, <https://doi.org/10.1190/1.1441514>.

Hill, R., 1963, Elastic properties of reinforced solids: some theoretical principles: *Journal of the Mechanics and Physics of Solids*, **11**(5), 357–372, [https://doi.org/10.1016/0022-5096\(63\)90036-X](https://doi.org/10.1016/0022-5096(63)90036-X).

Hoffmann, K., 1986, Applying the Wheatstone Bridge Circuit: Hottinger Baldwin Messtechnik, Darmstadt, Germany.

Hornby, B. E., L. M. Schwartz, and J. A. Hudson, 1994, Anisotropic effective-medium modeling of the elastic properties of shales: *Geophysics*, **59**(10), 1570–1583, <https://doi.org/10.1190/1.1443546>.

Hossain, M. M., 2017, Experimental and modelling approaches to determine the effect of moisture contents, grain contact and confining pressure on effective elastic properties of rock: Ph.D. dissertation, University of New South Wales.

Houben, M. E., 2013, In situ characterization of the microstructure and porosity of Opalinus Clay (Mont Terri Rock Laboratory, Switzerland): M.Sc. thesis, RWTH-Aachen University, Aachen, Germany.

Hughes, D. S., and J. H. Cross, 1951, Elastic wave velocities at high pressures and temperatures: *Geophysics*, **16**(4), 577–593, <https://doi.org/10.1190/1.1437706>.

Jizba, D., G. Mavko, and A. Nur, 1990, Static and dynamic moduli of tight gas sandstones: *SEG Technical Program Expanded Abstracts*, 827–829.

Johnson, K. L., K. Kendall, and A. D. Roberts, 1971, Surface energy and the contact of elastic solids: *Proceedings of the Royal Society. Series A, Mathematical, Physical and Engineering Sciences*, **324**(1558), 301–313, <https://doi.org/10.1098/rspa.1971.0141>.

Jones, L. E. A., and Wang H. F., 1981, Ultrasonic velocities in Cretaceous shales from the Williston Basin: *Geophysics*, **46**(3), 288–297, <https://doi.org/10.1190/1.1441199>.

Jones, S. B., and S. P. Friedman, 2000, Particle shape effects on the effective permittivity of anisotropic or isotropic media consisting of aligned or randomly oriented ellipsoidal particles: *Water Resources Research*, **36**(10), 2821–2833, <https://doi.org/10.1029/2000WR900198>.

Josh, M., 2014, Dielectric permittivity: A petrophysical parameter for shales: *Petrophysics*, **55**(4), 319–332, <https://doi.org/>

Josh, M., L. Esteban, C. Delle Piane, J. Sarout, D. N. Dewhurst, and M. B. Clennell, 2012, Laboratory characterization of shale properties: *Journal of Petroleum Science and Engineering*, **88–89**, 107–124, <https://doi.org/10.1016/j.petrol.2012.01.023>.

Kitamura, K., M. Ishikawa, and M. Arima, 2003, Petrological model of the northern Izu-Bonin-Mariana arc crust: Constraints from high-pressure measurements of elastic wave velocities of the Tanzawa plutonic rocks, central Japan: *Tectonophysics*, **371**(1–4), 213–221, [https://doi.org/10.1016/S0040-1951\(03\)00229-4](https://doi.org/10.1016/S0040-1951(03)00229-4).

Klein, B., P. Baud, T. Reuschlé, and T.-F. Wong, 2000, Mechanical behaviour and failure mode of Bentheim sandstone under triaxial compression: *Physics and Chemistry of the Earth, Part A: Solid Earth and Geodesy*, **26**(1–2), 21–25, [https://doi.org/10.1016/S1464-1895\(01\)00017-5](https://doi.org/10.1016/S1464-1895(01)00017-5).

Knight, R., and J. Dvorkin, 1992, Seismic and electrical properties of sandstones at low saturations: *Journal of Geophysical Research*, **97**(B12), 17425–17432, <https://doi.org/10.1029/92JB01794>.

Knight, R., and R. Nolen-Hoeksema, 1990, A laboratory study of the dependence of elastic wave velocities on pore scale fluid distribution: *Geophysical Research Letters*, **17**(10), 1529–1532, <https://doi.org/10.1029/GL017i010p01529>.

Kono, Y., M. Ishikawa, M. Harigane, K. Michibayashi, and M. Arima, 2009, P- and S-wave velocities of the lowermost crustal rocks from the Kohistan arc: Implications for seismic Moho discontinuity attributed to abundant garnet: *Tectonophysics*, **467**(1–4), 44–54, <https://doi.org/10.1016/j.tecto.2008.12.010>.

Kuc, R., M. Schwartz, and L. von Micsky, 1976, Parametric estimation of the acoustic attenuation coefficient slope for soft tissue: *Ultrasonic Symposium Proceedings*, **76**, 44–47.

Lebedev, M., M. Pervukhina, V. Mikhaltsevitch, T. Dance, O. Bilenko, and B. Gurevich, 2013, An experimental study of acoustic responses on the injection of supercritical CO<sub>2</sub> into sandstones from the Otway Basin: *Geophysics*, **78**(4), D293–D306, <https://doi.org/10.1190/geo2012-0528.1>.

Lima, A., E. Romero, Y. Piña, A. Gens, and X. Li, 2012, Water retention properties of two Deep Belgian clay formations, *in* C. Mancuso, C. Jommi, and F. D’Onza, eds., *Unsaturated Soils: Research and Applications*, Springer, 179–184.

Mah, M., and D. R. Schmitt, 2001, Experimental determination of the elastic coefficients of an orthorhombic material: *Geophysics*, **66**(4), 1217–1225, <https://doi.org/10.1190/1.1487068>.

Mavko, G., and D. Jizba, 1991, Estimating grain-scale fluid effects on velocity dispersion in rocks: *Geophysics*, **56**(12), 1940–1949, <https://doi.org/10.1190/1.1443005>.

Mavko, G., and R. Nolen-Hoeksema, 1994, Estimating seismic velocities in partially saturated rocks: *Geophysics*, **59**(2), 252–258, <https://doi.org/10.1190/1.1443587>.

Mavko G., T. Mukerji, and J. Dvorkin, 2009, *The rock physics handbook: 2nd edn.* Cambridge University Press.

McBain, J. W., and J. Ferguson, 1927, On the nature of the influence of humidity changes upon the composition of building materials: *The Journal of Physical Chemistry*, **31**(4), 564–590, <https://doi.org/10.1021/j150274a010>.

Meehan, F. T., 1927, The expansion of charcoal on sorption of carbon dioxide: *Proceedings of the Royal Society. Series A, Mathematical, Physical and Engineering Sciences*, **115**(770), 199–207, <https://doi.org/10.1098/rspa.1927.0085>

Menaceur, H., P. Delage, A. Minh Tang, J. Talandier, 2016, The status of water in swelling shales: an insight from the water retention properties of the Callovo-Oxfordian claystone: *Rock Mechanics and Rock Engineering*, **49**(12), 4571–4586, <https://doi.org/10.1007/s00603-016-1065-2>.

Mikhailtsevich, V., M. Lebedev, and B. Gurevich, 2016, Laboratory measurements of the effect of fluid saturation on elastic properties of carbonates at seismic frequencies: *Geophysical Prospecting*, **64**(4), 799–809, <https://doi.org/10.1111/1365-2478.12404>.

Mikhailtsevich, V., M. Lebedev, and B. Gurevich, 2017, Effect of water saturation on P-wave anisotropy in the Mancos Shale at seismic frequencies, 79th EAGE Conference and Exhibition, France, Extended Abstracts, Tu P3 11, <https://doi.org/10.3997/2214-4609.201701042>.

Minardi, A., E. Crisci, A. Ferrari, and L. Laloui, 2016, Anisotropic volumetric behaviour of Opalinus Clay shale upon suction variation: *Géotechnique Letters*, **6**(2), 144–148, <https://doi.org/10.1680/jgele.16.00023>.

Molyneux, J. B., and D. R. Schmitt, 2000, Compressional-wave velocities in attenuating media: A laboratory physical model study: *Geophysics*, **65**(4), 1162–1167, <https://doi.org/10.1190/1.1444809>.

Monfared, M., J. Sulem, P. Delage, and M. Mohajerani, 2014, Temperature and damage impact on the permeability of Opalinus Clay: *Rock Mechanics and Rock Engineering*, **47**(1), 101–110, <https://doi.org/10.1007/s00603-013-0459-7>.

Montes, H. G., J. Duplay, L. Martinez, S. Escoffier, and D. Rousset, 2004, Structural modifications of Callovo-Oxfordian Argillite under hydration/dehydration conditions: *Applied Clay Science*, **25**(3–4), 187–194, <https://doi.org/10.1016/j.clay.2003.10.004>.

Mukerji, T., and G. Mavko, 1994, Pore fluid effects on seismic velocity in anisotropic rocks: *Geophysics*, **59**(2), 233–244, <https://doi.org/10.1190/1.1443585>.

Müller, T. M., B. Gurevich, and M. Lebedev, 2010, Seismic wave attenuation and dispersion due to wave-induced flow in porous rocks – a review: *Geophysics*, **75**(5), A147–A164, <https://doi.org/10.1190/1.3463417>.

Murphy, W. F., 1982, Effect of microstructure and pore fluids on the acoustic properties of granular sedimentary materials: Ph.D. dissertation, Stanford University.

Murphy, W. F., 1984, Acoustic measures of partial gas saturation in tight sandstones: *Journal of Geophysical Research*, **89**(B13), 11549–11559, <https://doi.org/10.1029/JB089iB13p11549>.

Murphy, W. F., K. W. Winkler, and R. L. Kleinberg, 1984, Frame modulus reduction in sedimentary rocks: The effect of adsorption on grain contacts: *Geophysical Research Letters*, **11**(9), 805–808, <https://doi.org/10.1029/GL011i009p00805>.

Nakagawa, S., K. T. Nihei, and L. R. Myer, 2002, Elastic wave propagation along a set of parallel fractures: *Geophysical Research Letters*, **29**(16), 31-1–31-4, <https://doi.org/10.1029/2002GL014925>.

Narayana, P. A., and J. Ophir, 1983, A closed form method for the measurement of attenuation in nonlinearly dispersive media: *Ultrasonic Imaging*, **5**(1), 17–21, [https://doi.org/10.1016/0161-7346\(83\)90097-4](https://doi.org/10.1016/0161-7346(83)90097-4).

Nishizawa, O., 1982, Seismic velocity anisotropy in a medium containing oriented cracks – transversely isotropic case: *Journal of Physics of the Earth*, **30**(4), 331–347, <https://doi.org/10.4294/jpe1952.30.331>.

Osipov, V., V. Sokolov, and V. Eremeev, 2004, *Clay Seals of Oil and Gas Deposits*, A. A. Balkema Publishers.

Ougier-Simonin, A., Y. Guéguen, J. Fortin, A. Schubnel, and F. Bouyer, 2011, Permeability and elastic properties of cracked glass under pressure: *Journal of Geophysical Research*, **116**(B7), B07203, <https://doi.org/10.1029/2010JB008077>.

Özcan, D. M., A. Bayraktar, A. Şbahin, T. Haktanir, and T. Türker, 2009, Experimental and finite element analysis on the steel fiber-reinforced concrete (SFRC) beams ultimate behaviour: *Construction and Building Materials*, **23**(2), 1064–1077, <https://doi.org/10.1016/j.conbuildmat.2008.05.010>.

Page, J. H., J. Liu, B. Abeles, E. Herbolzheimer, H. W. Deckman, and D. A. Weitz, 1995, Adsorption and desorption of a wetting fluid in Vycor studied by acoustic and optical techniques: *Physical Review E*, **52**(3), 2763–2777, <https://doi.org/10.1103/PhysRevE.52.2763>.

Pandit, B. I., and M. S. King, 1979, The variation of elastic wave velocities and quality factor Q of a sandstone with moisture content: *Canadian Journal of Earth Sciences*, **16**(12), 2187–2195, <https://doi.org/10.1139/e79-206>.

Pervukhina, M., B. Gurevich, D. N. Dewhurst, and A. F. Siggins, 2009, Experimental verification of the physical nature of velocity–stress relationship for isotropic porous rocks: *SEG International Exposition and Annual Meeting, SEG Technical Program Extended Abstracts*, 2010–2014.

Pervukhina, M., B. Gurevich, D. N. Dewhurst, and A. F. Siggins, 2010, Applicability of velocity-stress relationships based on the dual porosity concept to isotropic porous rocks: *Geophysical Journal International*, **181**(3), 1473–1479, <https://doi.org/10.1111/j.1365-246X.2010.04535.x>.

Pervukhina, M., B. Gurevich, P. Golodoniuc, and D. N. Dewhurst, 2011, Parameterization of elastic stress sensitivity in shales: *Geophysics*, **76**(3), WA147–WA155, <https://doi.org/10.1190/1.3554401>.

Pevzner, R., T. M. Müller, R. J. Galvin, and B. Gurevich, 2012, Estimation of attenuation from zero-offset VSP data: CO2CRC Otway Project casestudy: *SEG Technical Program Expanded Abstracts 2012*, 1–6. <https://doi.org/https://doi.org/10.1190/segam2012-0950.1>.

Pimienta, L., J. Fortin, and Y. Guéguen, 2014, Investigation of elastic weakening in limestone and sandstone samples from moisture adsorption:

Geophysical Journal International, **199**(1), 335–347,  
<https://doi.org/10.1093/gji/ggu257>.

Prasad, M., 2002, Acoustic measurements in unconsolidated sands at low effective pressure and overpressure detection: *Geophysics*, **67**(2), 405–412,  
<https://doi.org/10.1190/1.1468600>.

Prass, J., D. Mütter, P. Fratzl, and O. Paris, 2009, Capillarity-driven deformation of ordered nanoporous silica: *Applied Physics Letters*, **95**(8), 083121,  
<https://doi.org/10.1063/1.3213564>.

Quan, Y. L., and J. M. Harris, 1997, Seismic attenuation tomography using the frequency shift method: *Geophysics*, **62**(3), 895–905,  
<https://doi.org/10.1190/1.1444197>.

Raper, R. L., and D. C. Erbach, 1990, Prediction of soil stresses using the finite element method: *Transactions of the ASAE*, **33**(3), 725–730,  
<https://doi.org/10.13031/2013.31392>.

Rasolofosaon, P., and B. Zinszner, 2004, Laboratory petroacoustics for seismic monitoring feasibility study: *The Leading Edge*, **23**(3), 252–258,  
<https://doi.org/10.1190/1.1690898>.

Reichenauer, G., and G. W. Scherer, 2000, Nitrogen adsorption in compliant materials: *Journal of Non-Crystalline Solids*, **277**(2–3), 162–172,  
[https://doi.org/10.1016/S0022-3093\(00\)00304-5](https://doi.org/10.1016/S0022-3093(00)00304-5).

Reichenauer, G., and G. W. Scherer, 2001, Nitrogen sorption in aerogels: *Journal of Non-Crystalline Solids*, **285**(1-3), 167–174,  
[https://doi.org/10.1016/S0022-3093\(01\)00449-5](https://doi.org/10.1016/S0022-3093(01)00449-5).

Reuss, A., 1929. Berechnung der fließgrenzen von mischkristallen auf grund der plastizitätsbedingung für einkristalle: *Journal of Applied Mathematics and Mechanics*, **9**(1), 49–58, <https://doi.org/10.1002/zamm.19290090104>.

Romero, E., G. Della Vecchia, and C. Jommi, 2011, An insight into the water retention properties of compacted clayey soils: *Géotechnique*, **61**(4), 313–328,  
<https://doi.org/10.1680/geot.2011.61.4.313>.

Saenger, E. H., O. S. Krüger, and S. A. Shapiro, 2006, Effective elastic properties of fractured rocks: Dynamic vs. static considerations: *International Journal of Fracture*, **139**(3–4), 569–576, <https://doi.org/10.1007/s10704-006-0105-4>.

Saenger, E. H., M. Lebedev, D. Uribe, M. Osorno, S. Vialle, M. Duda, S. Iglauer, and H. Steeb, 2016, Analysis of high-resolution X-ray computed

tomography images of Bentheim sandstone under elevated confining pressures: *Geophysical Prospecting*, **64**(4), 848–859, <https://doi.org/10.1111/1365-2478.12400>.

Saenger, E. H., C. Madonna, M. Frehner, and B. S. G. Almqvist, 2014, Numerical support of laboratory experiments: Attenuation and velocity estimations: *Acta Geophysica*, **62**(1), 1–11, <https://doi.org/10.2478/s11600-013-0162-9>.

Saito, T., 1981, Variation of physical properties of igneous rock in weathering: *Proceedings of the International Symposium on Weak Rock*, Tokyo, 191–196.

Saksala, T., M. Hokka, V.-T. Kuokkala, and J. Mäkinen, 2013, Numerical modeling and experimentation of dynamic Brazilian disc test on Kuru granite: *International Journal of Rock Mechanics & Mining Sciences*, **59**, 128–138, <https://doi.org/10.1016/j.ijrmms.2012.12.018>.

Salager, S., M. Nuth, A. Ferrari, and L. Laloui, 2013, Investigation into water retention behaviour of deformable soils: *Canadian Geotechnical Journal*, **50**(2), 200–208, <https://doi.org/10.1139/cgj-2011-0409>.

Sarout, J., L. Esteban, C. Delle Piane, B. Maney, and D. N. Dewhurst, 2014, Elastic anisotropy of Opalinus clay under variable saturation and triaxial stress: *Geophysical Journal International*, **198**(3), 1662–1682, <https://doi.org/10.1093/gji/ggu231>.

Sayers, C. M., 1999, Stress-dependent seismic anisotropy of shales: *Geophysics*, **64**(1), 93–98, <https://doi.org/10.1190/1.1444535>.

Sayers, C. M., and M. Kachanov, 1995, Microcrack-induced elastic wave anisotropy of brittle rock: *Journal of Geophysical Research*, **100**(B3), 4149–4156, <https://doi.org/10.1029/94JB03134>.

Schubnel, A., O. Nishizawa, K. Masuda, X. J. Lei, Z. Xue, and Y. Guéguen, 2003, Velocity measurements and crack density determination during wet triaxial experiments on Oshima and Toki granites: *Pure Applied Geophysics*, **160**(5–6), 869–887, <https://doi.org/10.1007/PL00012570>.

Scott, T. E., Q. Ma, and J.-C. Roegiers, 1993, Acoustic velocity changes during shear enhanced compaction of sandstone: *International Journal of Rock Mechanics and Mining Sciences*, **30**(7), 763–769, [https://doi.org/10.1016/0148-9062\(93\)90020-E](https://doi.org/10.1016/0148-9062(93)90020-E).

Schappert, K., and R. Pelster, 2014, Unexpected sorption-induced deformation of nanoporous glass: Evidence for spatial rearrangement of adsorbed argon: *Langmuir*, **30**(46), 14004–14013, <https://doi.org/10.1021/la502974w>.

Shapiro, S. A., 2003, Elastic piezosensitivity of porous and fractured rocks: *Geophysics*, **68**(2), 482–486, <https://doi.org/10.1190/1.1567215>.

Shapiro, S. A., and A. Kaselow, 2005, Porosity and elastic anisotropy of rocks under tectonic-stress and pore-pressure changes: *Geophysics*, **70**(5), N27–N38, <https://doi.org/10.1190/1.2073884>.

Sharifi, P., B. Marmiroli, B. Sartori, F. Cacho-Nerin, J. Keckes, H. Amenitsch, and O. Paris, 2014, Humidity-driven deformation of ordered mesoporous silica films: *Bioinspired, Biomimetic Nanobiomater*, **3**(3), 183–190, <https://doi.org/10.1680/bbn.14.00017>.

Smith, T. M., C. H. Sondergeld, and C. S. Rai, 2003, Gassmann fluid substitutions: A tutorial: *Geophysics*, **68**(2), 430–440, <https://doi.org/10.1190/1.1567211>.

Soe, A. K. K., M. Osada, M. Takahashi, and T. Sasaki, 2009, Characterization of drying-induced deformation behaviour of Opalinus Clay and tuff in no-stress regime: *Environmental Geology*, **58**(6), 1215–1225, <https://doi.org/10.1007/s00254-008-1616-2>.

Spencer, J. W., 1981, Stress relaxations at low frequencies in fluid-saturated rocks: Attenuation and modulus dispersion: *Journal of Geophysical Research: Solid Earth*, **86**(B3), 1803–1812, <https://doi.org/10.1029/JB086iB03p01803>.

Spikes, K. T., 2014, Error estimates of elastic components in stress-dependent VTI media: *Journal of Applied Geophysics*, **108**, 110–123, <https://doi.org/10.1016/j.jappgeo.2014.06.015>.

Steward, R., and L. Peselnick, 1977, Velocity of compressional waves in dry Franciscan rocks to 8 kbar and 300°C: *Journal of Geophysical Research*, **82**(14), 2027–2039, <https://doi.org/10.1029/JB082i014p02027>.

Stoll, R. D., 1977, Acoustic waves in ocean sediments: *Geophysics*, **42**(4), 715–725, <https://doi.org/10.1190/1.1440741>.

Szewczyk, D., R. M. Holt, and A. Bauer, 2018, The impact of saturation on seismic dispersion in shales – laboratory measurements: *Geophysics*, **83**(1), MR15–MR34, <https://doi.org/10.1190/geo2017-0169.1>.

Thomsen, L., 1986, Weak elastic anisotropy: *Geophysics*, **51**(10), 1954–1966, <https://library.seg.org/doi/10.1190/1.1442051>.

Tittmann, B. R., V. A. Clark, J. M. Richardson, and T. W. Spencer, 1980, Possible mechanisms for seismic attenuation in rocks containing small amounts of volatiles: *Journal of Geophysical Research*, **85**(B10), 5199–5208, <https://doi.org/10.1029/JB085iB10p05199>.

Tsvankin, I., 2001, *Seismic Signatures and Analysis of Reflection Data in Anisotropic Media*, Pergamon, New York.

Trnkoczy, A., 2002, Understanding and parameter setting of STA/LTA trigger algorithm, *in* P. Bormann, ed., *New manual of seismological observatory practice*: Deutsches GeoForschungsZentrum GFZ, 1–20.

Tutuncu, A. N., 1992, *Velocity Dispersion and Attenuation of Acoustic Waves in Granular Sedimentary Media*: Ph.D. dissertation, University of Texas.

Vales, F., D. Nguyen Minh, H. Gharbi, and A. Rejeb, 2004, Experimental study of the influence of the degree of saturation on physical and mechanical properties in Tournemire shale (France): *Applied Clay Science*, **26**(1–4), 197–207, <https://doi.org/10.1016/j.clay.2003.12.032>.

Vandamme, M., L. Brochard, B. Lecampion, and O. Coussy, 2010, Adsorption and strain: The CO<sub>2</sub>-induced swelling of coal: *Journal of the Mechanics and Physics of Solids*, **58**(10), 1489–1505, <https://doi.org/10.1016/j.jmps.2010.07.014>.

Vernik, L., and A. Nur, 1992, Ultrasonic velocity and anisotropy of hydrocarbon source rocks: *Geophysics*, **57**(5), 727–735, <https://doi.org/10.1190/1.1443286>.

Walsh, J. B., 1965, The effect of cracks on the compressibility of rocks: *Journal of Geophysical Research*, **70**(2), 381–389, <https://doi.org/10.1029/JZ070i002p00381>.

Wan, M., P. Delage, A. Minh Tang, and J. Talandier, 2013, Water retention properties of the Callovo-Oxfordian claystone: *International Journal of Rock Mechanics and Mining Science*, **64**, 96–104, <https://doi.org/10.1016/j.ijrmms.2013.08.020>.

Wild, K. M., L. P. Wymann, S. Zimmer, R. Thoeny, and F. Amann, 2015, Water retention characteristics and state-dependent mechanical and petro-physical

properties of a clay shale: *Rock Mechanics and Rock Engineering*, **48**(2), 427–439, <https://doi.org/10.1007/s00603-014-0565-1>.

Wyllie, M. R. J., A. R. Gregory, and L. W. Gardner, 1956, Elastic wave velocities in heterogeneous and porous media: *Geophysics*, **21**(1), 41–70, <https://doi.org/10.1190/1.1438217>.

Wyllie, M. R. J., A. R. Gregory, and G. H. F. Gardner, 1962, Studies of elastic wave attenuation in porous media: *Geophysics*, **27**(5), 569–589, <https://doi.org/10.1190/1.1439063>.

Winkler, K. W., and W. F. Murphy, 1995, Acoustic velocity and attenuation in porous rocks, *in* T. J. Ahrens, ed., *Rock Physics and phase relations: a handbook of physical constants*, 20–34.

Winkler, K. W., and A. Nur, 1979, Pore fluids and seismic attenuation in rocks: *Geophysical Research Letters*, **6**(1), 1–4, <https://doi.org/10.1029/GL006i001p00001>.

Yoshikawa, S., and K. Mogi, 1989, Experimental studies on the effect of stress history on acoustic emission activity: A possibility for estimation of rock stress: *Journal of Acoustic Emission*, **8**, 113–123.

Zimmermann, R. W., 1991, *Compressibility of Sandstones*: New York: Elsevier.

Zimmerman, R. W., W. H. Somerton, and M. S. King, 1986, Compressibility of porous rocks: *Journal of Geophysical Research*, **91**(B12), 12765–12777, <https://doi.org/10.1029/JB091iB12p12765>.

Every reasonable effort has been made to acknowledge the owners of copyright material. I would be pleased to hear from any copyright owner who has been omitted or incorrectly acknowledged.

# Appendices

## Data and scripts

### Chapter 1

The experimental data reported in Chapter 1 (Figure 8) is summarised in the tables below.

**Table 7** Measured velocities of ultrasonic P- and S-waves ( $V_P$  and  $V_S$ ) in standard and thin disc samples of PMMA and Berea sandstone.

Material	PMMA				Berea sandstone			
	Type	Standard		Disc		Standard		Disc
Pressure, MPa	$V_P$ , km/s	$V_S$ , km/s	$V_P$ , km/s	$V_S$ , km/s	$V_P$ , km/s	$V_S$ , km/s	$V_P$ , km/s	$V_S$ , km/s
2	2.782	1.400	2.848	1.387	3.545	2.119	3.512	2.153
4	2.776	1.403	2.792	1.387	3.666	2.258	3.582	2.233
6	2.776	1.403	2.819	1.394	3.748	2.325	3.655	2.276
8	2.770	1.405	2.764	1.394	3.784	2.371	3.731	2.335
10	2.770	1.407	2.792	1.394	3.833	2.405	3.770	2.350
14	2.770	1.408	2.848	1.401	3.871	2.445	3.810	2.414
18	2.770	1.412	2.819	1.401	3.910	2.481	3.851	2.430
22	2.776	1.415	2.848	1.401	3.936	2.503	3.935	2.446
26	2.789	1.420	2.848	1.408	3.962	2.524	3.979	2.463
30	2.795	1.425	2.848	1.415	3.976	2.540	3.979	2.498
34	2.801	1.428	2.877	1.415	3.976	2.551	4.024	2.515
38	2.814	1.433	2.877	1.415	4.003	2.563	4.024	2.515
42	2.821	1.435	2.906	1.422	4.003	2.568	4.069	2.533
46	2.834	1.440	2.877	1.429	4.017	2.579	4.069	2.551
50	2.834	1.443	2.906	1.436	4.017	2.585	4.116	2.569

**Table 8** Measured velocities of ultrasonic P- and S-waves ( $V_P$  and  $V_S$ ) in standard and thin disc samples of Bentheim sandstone and Opalinus shale. In the case of Opalinus shale,  $V_P$  and  $V_S$  are the velocities of elastic waves propagating and polarised along the bedding plane.

<b>Material</b>	Bentheim sandstone				Opalinus shale			
	Standard		Disc		Standard		Disc	
<b>Type</b>	$V_P$ , km/s	$V_S$ , km/s	$V_P$ , km/s	$V_S$ , km/s	$V_P$ , km/s	$V_S$ , km/s	$V_P$ , km/s	$V_S$ , km/s
2	3.118	2.166	3.297	2.172	3.515	1.875	3.291	1.981
4	3.423	2.339	3.361	2.286	3.551	1.928	3.447	1.986
6	3.577	2.409	3.532	2.381	3.581	1.941	3.513	1.992
8	3.631	2.459	3.568	2.448	3.588	1.943	3.513	1.992
10	3.687	2.491	3.643	2.465	3.618	1.990	3.565	1.997
14	3.728	2.518	3.803	2.537	3.626	1.985	3.565	2.008
18	3.769	2.544	3.888	2.575	3.634	1.994	3.600	2.025
22	3.795	2.564	3.933	2.614	3.649	2.013	3.600	2.036
26	3.830	2.580	3.978	2.634	3.664	2.013	3.618	2.048
30	3.847	2.596	4.024	2.674	3.672	2.008	3.636	2.059
34	3.856	2.600	4.071	2.695	3.680	2.006	3.673	2.077
38	3.874	2.608	4.119	2.695	3.696	2.008	3.691	2.095
42	3.883	2.612	4.169	2.716	3.696	2.008	3.710	2.101
46	3.892	2.616	4.169	2.738	3.711	2.001	3.729	2.107
50	3.901	2.624	4.169	2.759	3.711	2.011	3.729	2.119

## Chapter 2

The experimental data reported in Chapter 2 (Figure 20) is summarised in the tables below.

**Table 9** Measured elastic properties of the Opalinus shale in the preserved state.

<b>Pressure, MPa</b>	<b><math>C_{11}</math>, GPa</b>	<b><math>C_{33}</math>, GPa</b>	<b><math>C_{44}</math>, GPa</b>	<b><math>C_{66}</math>, GPa</b>
2	31.19	18.07	3.75	10.85
4	33.97	19.39	3.92	10.72
6	35.22	19.53	4.00	10.60
8	35.96	20.06	4.06	10.63
10	36.73	20.37	4.12	10.63
14	37.13	20.45	4.18	10.78
18	37.33	20.53	4.21	10.85
22	37.53	20.61	4.26	10.94
26	37.73	20.69	4.29	11.01
30	37.94	21.10	4.35	11.20
34	38.35	21.26	4.38	11.30
38	38.56	21.35	4.42	11.44
42	38.99	21.60	4.46	11.50
46	38.99	21.77	4.48	11.54
50	39.21	21.86	4.50	11.64

**Table 10** Measured elastic properties of the Opalinus shale in the hydration state obtained in the atmosphere with 52% relative humidity.

<b>Pressure, MPa</b>	<b><math>C_{11}</math>, GPa</b>	<b><math>C_{33}</math>, GPa</b>	<b><math>C_{44}</math>, GPa</b>	<b><math>C_{66}</math>, GPa</b>
2	30.44	10.56	5.05	11.13
4	34.14	11.56	5.18	12.75
6	34.50	11.91	5.28	12.83
8	34.68	12.16	5.38	13.04
10	35.42	12.31	5.49	13.21
14	36.38	12.66	5.61	13.43
18	36.58	13.02	5.73	13.61
22	37.59	13.40	5.82	13.84
26	37.80	13.80	5.87	13.65
30	38.01	14.02	5.95	13.74
34	38.43	14.69	6.04	13.79
38	38.65	14.94	6.12	13.88
42	39.30	15.30	6.17	13.98
46	39.75	15.62	6.24	14.02
50	39.52	15.78	6.31	14.16

**Table 11** Measured elastic properties of the Opalinus shale in the hydration state obtained in the atmosphere with 31% relative humidity.

<b>Pressure, MPa</b>	<b>C<sub>11</sub>, GPa</b>	<b>C<sub>33</sub>, GPa</b>	<b>C<sub>44</sub>, GPa</b>	<b>C<sub>66</sub>, GPa</b>
2	31.41	10.33	5.56	12.54
4	32.88	11.18	5.82	13.21
6	34.30	11.66	6.06	13.47
8	35.22	12.06	6.18	13.89
10	35.98	12.37	6.31	14.07
14	36.98	12.72	6.47	14.51
18	37.60	13.09	6.58	14.51
22	37.81	13.31	6.66	14.77
26	38.02	13.52	6.72	14.77
30	38.24	13.93	6.78	14.87
34	38.67	14.21	6.83	14.92
38	38.46	14.46	6.86	15.03
42	39.58	14.80	6.96	15.13
46	39.10	15.32	6.98	15.19
50	39.78	15.70	7.06	15.13

**Table 12** Measured elastic properties of the Opalinus shale in the hydration state obtained in the atmosphere with 13% relative humidity.

<b>Pressure, MPa</b>	<b>C<sub>11</sub>, GPa</b>	<b>C<sub>33</sub>, GPa</b>	<b>C<sub>44</sub>, GPa</b>	<b>C<sub>66</sub>, GPa</b>
2	41.62	11.29	6.36	16.23
4	43.41	11.81	6.81	16.60
6	43.40	12.19	7.04	16.91
8	44.19	12.78	7.23	16.97
10	44.19	12.95	7.37	16.97
14	43.91	13.16	7.51	17.56
18	44.18	13.38	7.66	17.56
22	43.92	13.42	7.76	17.90
26	44.19	13.64	7.83	17.90
30	44.46	13.87	7.87	18.04
34	44.47	14.15	7.97	18.11
38	44.74	14.20	8.05	18.25
42	44.47	14.54	8.09	18.11
46	45.02	14.85	8.15	18.18
50	45.32	15.00	8.22	18.11

**Table 13** Measured elastic properties of the Opalinus shale in the hydration state obtained in the atmosphere with 97% relative humidity.

Pressure, MPa	$C_{11}$ , GPa	$C_{33}$ , GPa	$C_{44}$ , GPa	$C_{66}$ , GPa
2	27.24	12.35	2.65	7.39
4	29.27	14.02	2.74	7.83
6	29.90	14.96	2.82	7.95
8	30.72	16.05	2.90	8.13
10	31.75	16.72	2.98	8.17
14	32.55	17.63	3.05	8.27
18	32.51	17.95	3.09	8.57
22	33.34	18.28	3.14	8.91
26	32.51	17.95	3.16	9.00
30	33.34	18.28	3.21	8.91
34	32.68	18.01	3.24	9.03
38	33.51	18.34	3.25	9.17
42	33.01	18.14	3.25	8.84
46	34.03	18.55	3.27	8.96
50	33.51	18.34	3.29	8.89

### Chapter 3

The scripts used for the effective medium modelling are available via the link: <http://crgc.org.au/?p=531>

**Table 14** The components of the stiffness tensor  $C^{matrix}$  obtained at the first step of the modelling (section 3.3 ) depending on the used parameters  $\alpha$  and  $\delta$ .

$\alpha$	$\delta$	$C_{11}$ , GPa	$C_{33}$ , GPa	$C_{44}$ , GPa	$C_{66}$ , GPa	$C_{13}$ , GPa
1.0	0.35	46.23	26.90	4.72	16.22	24.47
0.9	0.35	46.32	27.43	4.73	15.99	24.88
0.8	0.35	46.48	28.11	4.74	15.73	25.43
0.7	0.35	46.75	29.03	4.76	15.43	26.17
0.6	0.35	47.25	30.33	4.80	15.09	27.24
0.5	0.35	48.17	32.29	4.85	14.70	28.85
0.4	0.35	49.97	35.52	4.95	14.29	31.56
0.3	0.35	53.96	41.77	5.14	13.84	36.86
0.2	0.35	65.67	58.42	5.59	13.38	51.14
0.1	0.35	188.59	223.13	7.50	12.91	193.75
0.1	0.20	101.49	140.91	7.31	12.89	104.21
0.1	0.05	66.65	109.40	7.17	12.88	64.69

## **Chapter 4**

The experimental data reported in Chapter 4 is available via repository: DOI: [10.6084/m9.figshare.7056653](https://doi.org/10.6084/m9.figshare.7056653).

## Attribution tables

The research papers that form the basis of this thesis, are an outcome of my collaborative work with other researchers. The following attribution tables explicitly declare the contribution of each co-author in each paper.

1. Paper: “Ultrasonic velocity measurements on thin rock samples: experiment and numerical modelling”, 2018, Geophysics, **83**(2), MR47–MR56, doi: 10.1190/GEO2016-0685.1

Authors: Mr. Alexey Yurikov (Curtin University, Australia)  
 Prof. Maxim Lebedev (Curtin University, Australia)  
 Dr. Marina Pervukhina (CSIRO Energy, Australia)

Co-author	Conception and design	Experimental methods and data acquisition	Design of numerical models	Analysis of results and discussion	Paper writing and editing
Mr. Alexey Yurikov	60%	80%	70%	60%	65%
I acknowledge that these represent my contribution to the above research output.					
Signature: 					
Prof. Maxim Lebedev	20%	20%	–	20%	5%
I acknowledge that these represent my contribution to the above research output.					
Signature: <b>Maxim Lebedev</b>  <small>Digitally signed by Maxim Lebedev        Date: 2018.12.19 06:53:32 +08'00'</small>					
Dr. Marina Pervukhina	20%	–	30%	20%	30%
I acknowledge that these represent my contribution to the above research output.					
Signature: 					

2. Paper: “Water retention effects on elastic properties of Opalinus shale”, 2018, Geophysical Prospecting, Special Issue, 1–13, doi: 10.1111/1365-2478.12673

Authors: Mr. Alexey Yurikov (Curtin University, Australia)  
 Prof. Maxim Lebedev (Curtin University, Australia)  
 Dr. Marina Pervukhina (CSIRO Energy, Australia)  
 Prof. Boris Gurevich (Curtin University, CSIRO, Australia)

Co-author	Conception and design	Experimental methods and data acquisition	Rock physics modelling	Analysis of results and discussion	Paper writing and editing
Mr. Alexey Yurikov	50%	80%	60%	60%	70%
I acknowledge that these represent my contribution to the above research output.					
Signature: 					
Prof. Maxim Lebedev	25%	20%	–	15%	5%
I acknowledge that these represent my contribution to the above research output.					
Signature: <b>Maxim Lebedev</b>  Digitally signed by Maxim Lebedev Date: 2018.12.19 06:54:24 +08'00'					
Dr. Marina Pervukhina	25%	–	35%	15%	20%
I acknowledge that these represent my contribution to the above research output.					
Signature: 					
Prof. Boris Gurevich	–	–	5%	10%	5%
I acknowledge that these represent my contribution to the above research output.					
Signature: <b>Boris Gurevich</b>  Digitally signed by Boris Gurevich Date: 2018.12.19 00:50:53 +08'00'					

3. Paper: “Sorption-induced deformation and elastic weakening of Bentheim sandstone”, 2018, Journal of Geophysical Research – Solid Earth, **123**(10), 8589–8601, doi: 10.1029/2018JB016003

Authors: Mr. Alexey Yurikov (Curtin University, Australia)  
 Prof. Maxim Lebedev (Curtin University, Australia)  
 Prof. Gennady Y. Gor (New Jersey Institute of Technology, USA)  
 Prof. Boris Gurevich (Curtin University, CSIRO, Australia)

Co-author	Conception and design	Experimental methods and data acquisition	Analysis of results and discussion	Paper writing and editing
Mr. Alexey Yurikov	60%	80%	50%	70%
I acknowledge that these represent my contribution to the above research output.				
Signature: 				
Prof. Maxim Lebedev	20%	20%	5%	–
I acknowledge that these represent my contribution to the above research output.				
Signature: <b>Maxim Lebedev</b> Digitally signed by Maxim Lebedev Date: 2018.12.19 06:55:23 +08'00'				
Prof. Gennady Y. Gor	–	–	15%	5%
I acknowledge that these represent my contribution to the above research output.				
Signature: 				
Prof. Boris Gurevich	20%	–	30%	25%
I acknowledge that these represent my contribution to the above research output.				
Signature: <b>Boris Gurevich</b> Digitally signed by Boris Gurevich Date: 2018.12.19 00:55:33 +08'00'				

# Copyright permissions

26/11/2018

Copyright Clearance Center



**Confirmation Number: 11766950**

## Special Rightsholder Terms & Conditions

The following terms & conditions apply to the specific publication under which they are listed

### Geophysics

**Permission type:** Republish or display content

**Type of use:** Thesis/Dissertation

#### TERMS AND CONDITIONS

**The following terms are individual to this publisher:**

None

#### Other Terms and Conditions:

#### STANDARD TERMS AND CONDITIONS

1. Description of Service; Defined Terms. This Republication License enables the User to obtain licenses for republication of one or more copyrighted works as described in detail on the relevant Order Confirmation (the "Work(s)"). Copyright Clearance Center, Inc. ("CCC") grants licenses through the Service on behalf of the rightsholder identified on the Order Confirmation (the "Rightsholder"). "Republishing", as used herein, generally means the inclusion of a Work, in whole or in part, in a new work or works, also as described on the Order Confirmation. "User", as used herein, means the person or entity making such republication.

2. The terms set forth in the relevant Order Confirmation, and any terms set by the Rightsholder with respect to a particular Work, govern the terms of use of Works in connection with the Service. By using the Service, the person transacting for a republication license on behalf of the User represents and warrants that he/she/it (a) has been duly authorized by the User to accept, and hereby does accept, all such terms and conditions on behalf of User, and (b) shall inform User of all such terms and conditions. In the event such person is a "freelancer" or other third party independent of User and CCC, such party shall be deemed jointly a "User" for purposes of these terms and conditions. In any event, User shall be deemed to have accepted and agreed to all such terms and conditions if User republishes the Work in any fashion.

#### 3. Scope of License; Limitations and Obligations.

3.1 All Works and all rights therein, including copyright rights, remain the sole and exclusive property of the Rightsholder. The license created by the exchange of an Order Confirmation (and/or any invoice) and payment by User of the full amount set forth on that document includes only those rights expressly set forth in the Order Confirmation and in these terms and conditions, and conveys no other rights in the Work(s) to User. All rights not expressly granted are hereby reserved.

3.2 General Payment Terms: You may pay by credit card or through an account with us payable at the end of the month. If you and we agree that you may establish a standing account with CCC, then the following terms apply: Remit Payment to: Copyright Clearance Center, 29118 Network Place, Chicago, IL 60673-1291. Payments Due: Invoices are payable upon their delivery to you (or upon our notice to you that they are available to you for downloading). After 30 days, outstanding amounts will be subject to a service charge of 1-1/2% per month or, if less, the maximum rate allowed by applicable law. Unless otherwise specifically set forth in the Order Confirmation or in a separate written agreement signed by CCC, invoices are due and payable on "net 30" terms. While User may exercise the rights licensed immediately upon issuance of the Order Confirmation, the license is automatically revoked and is null and void, as if it had never been issued, if complete payment for the license is not received on a timely basis either from User directly or through a payment agent, such as a credit card company.

3.3 Unless otherwise provided in the Order Confirmation, any grant of rights to User (i) is "one-time" (including the editions and product family specified in the license), (ii) is non-exclusive and non-transferable and (iii) is subject to any and all limitations and restrictions (such as, but not limited to, limitations on duration of use or circulation) included in the Order Confirmation or invoice and/or in these terms and conditions. Upon completion of the licensed use, User shall either secure a new permission for further use of the Work(s) or immediately cease any new use of the Work(s) and shall render inaccessible (such as by deleting or by removing or severing links or other locators) any further copies of the Work (except for copies printed on paper in accordance with this license and still in User's stock at the end of such period).

3.4 In the event that the material for which a republication license is sought includes third party materials (such as photographs, illustrations, graphs, inserts and similar materials) which are identified in such material as having been used by permission, User is responsible for identifying, and seeking separate licenses (under this Service or otherwise) for, any of such third party materials; without a separate license, such third party materials may not be used.

3.5 Use of proper copyright notice for a Work is required as a condition of any license granted under the Service. Unless otherwise provided in the Order Confirmation, a proper copyright notice will read substantially as follows: "Republished with permission of [Rightsholder's name], from [Work's title, author, volume, edition number and year of copyright]; permission conveyed through Copyright Clearance Center, Inc." Such notice must be provided in a reasonably legible font size and must be placed either immediately adjacent to the Work as used (for example, as part of a by-line or

<https://www.copyright.com/reviewCoITermsConfirm.do?confirmNum=11766950>

1/4

footnote but not as a separate electronic link) or in the place where substantially all other credits or notices for the new work containing the republished Work are located. Failure to include the required notice results in loss to the Rightsholder and CCC, and the User shall be liable to pay liquidated damages for each such failure equal to twice the use fee specified in the Order Confirmation, in addition to the use fee itself and any other fees and charges specified.

3.6 User may only make alterations to the Work if and as expressly set forth in the Order Confirmation. No Work may be used in any way that is defamatory, violates the rights of third parties (including such third parties' rights of copyright, privacy, publicity, or other tangible or intangible property), or is otherwise illegal, sexually explicit or obscene. In addition, User may not conjoin a Work with any other material that may result in damage to the reputation of the Rightsholder. User agrees to inform CCC if it becomes aware of any infringement of any rights in a Work and to cooperate with any reasonable request of CCC or the Rightsholder in connection therewith.

4. Indemnity. User hereby indemnifies and agrees to defend the Rightsholder and CCC, and their respective employees and directors, against all claims, liability, damages, costs and expenses, including legal fees and expenses, arising out of any use of a Work beyond the scope of the rights granted herein, or any use of a Work which has been altered in any unauthorized way by User, including claims of defamation or infringement of rights of copyright, publicity, privacy or other tangible or intangible property.

5. Limitation of Liability. UNDER NO CIRCUMSTANCES WILL CCC OR THE RIGHTSHOLDER BE LIABLE FOR ANY DIRECT, INDIRECT, CONSEQUENTIAL OR INCIDENTAL DAMAGES (INCLUDING WITHOUT LIMITATION DAMAGES FOR LOSS OF BUSINESS PROFITS OR INFORMATION, OR FOR BUSINESS INTERRUPTION) ARISING OUT OF THE USE OR INABILITY TO USE A WORK, EVEN IF ONE OF THEM HAS BEEN ADVISED OF THE POSSIBILITY OF SUCH DAMAGES. In any event, the total liability of the Rightsholder and CCC (including their respective employees and directors) shall not exceed the total amount actually paid by User for this license. User assumes full liability for the actions and omissions of its principals, employees, agents, affiliates, successors and assigns.

6. Limited Warranties. THE WORK(S) AND RIGHT(S) ARE PROVIDED "AS IS". CCC HAS THE RIGHT TO GRANT TO USER THE RIGHTS GRANTED IN THE ORDER CONFIRMATION DOCUMENT. CCC AND THE RIGHTSHOLDER DISCLAIM ALL OTHER WARRANTIES RELATING TO THE WORK(S) AND RIGHT(S), EITHER EXPRESS OR IMPLIED, INCLUDING WITHOUT LIMITATION IMPLIED WARRANTIES OF MERCHANTABILITY OR FITNESS FOR A PARTICULAR PURPOSE. ADDITIONAL RIGHTS MAY BE REQUIRED TO USE ILLUSTRATIONS, GRAPHS, PHOTOGRAPHS, ABSTRACTS, INSERTS OR OTHER PORTIONS OF THE WORK (AS OPPOSED TO THE ENTIRE WORK) IN A MANNER CONTEMPLATED BY USER; USER UNDERSTANDS AND AGREES THAT NEITHER CCC NOR THE RIGHTSHOLDER MAY HAVE SUCH ADDITIONAL RIGHTS TO GRANT.

7. Effect of Breach. Any failure by User to pay any amount when due, or any use by User of a Work beyond the scope of the license set forth in the Order Confirmation and/or these terms and conditions, shall be a material breach of the license created by the Order Confirmation and these terms and conditions. Any breach not cured within 30 days of written notice thereof shall result in immediate termination of such license without further notice. Any unauthorized (but licensable) use of a Work that is terminated immediately upon notice thereof may be liquidated by payment of the Rightsholder's ordinary license price therefor; any unauthorized (and unlicensable) use that is not terminated immediately for any reason (including, for example, because materials containing the Work cannot reasonably be recalled) will be subject to all remedies available at law or in equity, but in no event to a payment of less than three times the Rightsholder's ordinary license price for the most closely analogous licensable use plus Rightsholder's and/or CCC's costs and expenses incurred in collecting such payment.

#### 8. Miscellaneous.

8.1 User acknowledges that CCC may, from time to time, make changes or additions to the Service or to these terms and conditions, and CCC reserves the right to send notice to the User by electronic mail or otherwise for the purposes of notifying User of such changes or additions; provided that any such changes or additions shall not apply to permissions already secured and paid for.

8.2 Use of User-related information collected through the Service is governed by CCC's privacy policy, available online here: <http://www.copyright.com/content/cc3/en/tools/footer/privacypolicy.html>.

8.3 The licensing transaction described in the Order Confirmation is personal to User. Therefore, User may not assign or transfer to any other person (whether a natural person or an organization of any kind) the license created by the Order Confirmation and these terms and conditions or any rights granted hereunder; provided, however, that User may assign such license in its entirety on written notice to CCC in the event of a transfer of all or substantially all of User's rights in the new material which includes the Work(s) licensed under this Service.

8.4 No amendment or waiver of any terms is binding unless set forth in writing and signed by the parties. The Rightsholder and CCC hereby object to any terms contained in any writing prepared by the User or its principals, employees, agents or affiliates and purporting to govern or otherwise relate to the licensing transaction described in the Order Confirmation, which terms are in any way inconsistent with any terms set forth in the Order Confirmation and/or in these terms and conditions or CCC's standard operating procedures, whether such writing is prepared prior to, simultaneously with or subsequent to the Order Confirmation, and whether such writing appears on a copy of the Order Confirmation or in a separate instrument.

8.5 The licensing transaction described in the Order Confirmation document shall be governed by and construed under the law of the State of New York, USA, without regard to the principles thereof of conflicts of law. Any case, controversy, suit, action, or proceeding arising out of, in connection with, or related to such licensing transaction shall be brought, at CCC's sole discretion, in any federal or state court located in the County of New York, State of New York, USA, or in any federal or state court whose geographical jurisdiction covers the location of the Rightsholder set forth in the Order Confirmation. The parties expressly submit to the personal jurisdiction and venue of each such federal or state court. If you have any comments or questions about the Service or Copyright Clearance Center, please contact us at 978-750-8400 or send an e-mail to [info@copyright.com](mailto:info@copyright.com).

v 1.1



**Confirmation Number: 11766950**  
**Order Date: 11/20/2018**

#### Customer Information

**Customer:** Alexey Yurikov  
**Account Number:** 3001369142  
**Organization:** Alexey Yurikov  
**Email:**  
alexey.yurikov@postgrad.curtin.edu.au  
**Phone:** +61 (4)24058613  
**Payment Method:** Invoice

#### This is not an invoice

#### Order Details

#### Geophysics

Billing Status:  
**N/A**

**Order detail ID:** 71672560  
**ISSN:** 0016-8033  
**Publication Type:** Journal  
**Volume:**  
**Issue:**  
**Start page:**  
**Publisher:** SOCIETY OF EXPLORATION  
GEOPHYSICISTS,  
SOCIETY OF PETROLEUM  
GEOPHYSICISTS ; SOCIETY OF  
EXPLORATION GEOPHYSICISTS  
**Author/Editor:**

**Permission Status:** **Granted**  
**Permission type:** Republish or display content  
**Type of use:** Thesis/Dissertation  
**Order License Id:** 4473341443627

**Requestor type:** Author of requested content  
**Format:** Print, Electronic  
**Portion:** chapter/article  
**The requesting person/organization:** Alexey Yurikov  
**Title or numeric reference of the portion(s):** The full content of the article  
**Title of the article or chapter the portion is from:** Ultrasonic velocity measurements on thin rock samples: Experiment and numerical modeling  
**Editor of portion(s):** N/A  
**Author of portion(s):** Alexey Yurikov  
**Volume of serial or monograph:** 83  
**Page range of portion:**  
**Publication date of portion:** March-April 2018  
**Rights for:** Main product  
**Duration of use:** Life of current edition  
**Creation of copies for the disabled:** no  
**With minor editing privileges:** no  
**For distribution to:** Worldwide  
**In the following language(s):** Original language of publication  
**With incidental promotional use:** no  
**Lifetime unit quantity of new product:** Up to 499  
**Title:** Experimental and theoretical study of effects of varying hydration on

26/11/2018

Copyright Clearance Center

elastic properties and  
microstructure of shales  
and sandstones  
Curtin University

**Institution name**  
**Expected presentation  
date**

Dec 2018

**Note:** This item was invoiced separately through our **RightsLink service**. [More info](#)

**\$ 0.00**

**Total order items: 1**

**Order Total: \$0.00**

[About Us](#) | [Privacy Policy](#) | [Terms & Conditions](#) | [Pay an Invoice](#)

Copyright 2018 Copyright Clearance Center

## JOHN WILEY AND SONS LICENSE TERMS AND CONDITIONS

Nov 26, 2018

This Agreement between Alexey Yurikov ("You") and John Wiley and Sons ("John Wiley and Sons") consists of your license details and the terms and conditions provided by John Wiley and Sons and Copyright Clearance Center.

License Number	4473350251539
License date	Nov 20, 2018
Licensed Content Publisher	John Wiley and Sons
Licensed Content Publication	Geophysical Prospecting
Licensed Content Title	Water retention effects on elastic properties of Opalinus shale
Licensed Content Author	Alexey Yurikov, Maxim Lebedev, Marina Pervukhina, et al
Licensed Content Date	Aug 10, 2018
Licensed Content Volume	0
Licensed Content Issue	0
Licensed Content Pages	13
Type of Use	Dissertation/Thesis
Requestor type	Author of this Wiley article
Format	Print and electronic
Portion	Full article
Will you be translating?	No
Title of your thesis / dissertation	Experimental and theoretical study of effects of varying hydration on elastic properties and microstructure of shales and sandstones
Expected completion date	Dec 2018
Expected size (number of pages)	1
Requestor Location	Alexey Yurikov 26 Dick Perry Avenue  Kensington, other Australia Attn:
Publisher Tax ID	EU826007151
Total	<b>0.00 AUD</b>
Terms and Conditions	

### TERMS AND CONDITIONS

This copyrighted material is owned by or exclusively licensed to John Wiley & Sons, Inc. or one of its group companies (each a "Wiley Company") or handled on behalf of a society with which a Wiley Company has exclusive publishing rights in relation to a particular work (collectively "WILEY"). By clicking "accept" in connection with completing this licensing transaction, you agree that the following terms and conditions apply to this transaction (along with the billing and payment terms and conditions established by the Copyright Clearance Center Inc., ("CCC's Billing and Payment terms and conditions"), at the time that you opened your RightsLink account (these are available at any time at <http://myaccount.copyright.com>).

#### Terms and Conditions

- The materials you have requested permission to reproduce or reuse (the "Wiley Materials") are protected by copyright.
- You are hereby granted a personal, non-exclusive, non-sub licensable (on a stand-alone basis), non-transferable, worldwide, limited license to reproduce the Wiley Materials for the purpose specified in the licensing process. This license, **and any CONTENT (PDF or image file) purchased as part of your order**, is for a one-time use only and limited to any maximum distribution number specified in the license. The first instance of republication or reuse granted by this license

must be completed within two years of the date of the grant of this license (although copies prepared before the end date may be distributed thereafter). The Wiley Materials shall not be used in any other manner or for any other purpose, beyond what is granted in the license. Permission is granted subject to an appropriate acknowledgement given to the author, title of the material/book/journal and the publisher. You shall also duplicate the copyright notice that appears in the Wiley publication in your use of the Wiley Material. Permission is also granted on the understanding that nowhere in the text is a previously published source acknowledged for all or part of this Wiley Material. Any third party content is expressly excluded from this permission.

- With respect to the Wiley Materials, all rights are reserved. Except as expressly granted by the terms of the license, no part of the Wiley Materials may be copied, modified, adapted (except for minor reformatting required by the new Publication), translated, reproduced, transferred or distributed, in any form or by any means, and no derivative works may be made based on the Wiley Materials without the prior permission of the respective copyright owner. **For STM Signatory Publishers clearing permission under the terms of the [STM Permissions Guidelines](#) only, the terms of the license are extended to include subsequent editions and for editions in other languages, provided such editions are for the work as a whole in situ and does not involve the separate exploitation of the permitted figures or extracts.** You may not alter, remove or suppress in any manner any copyright, trademark or other notices displayed by the Wiley Materials. You may not license, rent, sell, loan, lease, pledge, offer as security, transfer or assign the Wiley Materials on a stand-alone basis, or any of the rights granted to you hereunder to any other person.
- The Wiley Materials and all of the intellectual property rights therein shall at all times remain the exclusive property of John Wiley & Sons Inc, the Wiley Companies, or their respective licensors, and your interest therein is only that of having possession of and the right to reproduce the Wiley Materials pursuant to Section 2 herein during the continuance of this Agreement. You agree that you own no right, title or interest in or to the Wiley Materials or any of the intellectual property rights therein. You shall have no rights hereunder other than the license as provided for above in Section 2. No right, license or interest to any trademark, trade name, service mark or other branding ("Marks") of WILEY or its licensors is granted hereunder, and you agree that you shall not assert any such right, license or interest with respect thereto
- NEITHER WILEY NOR ITS LICENSORS MAKES ANY WARRANTY OR REPRESENTATION OF ANY KIND TO YOU OR ANY THIRD PARTY, EXPRESS, IMPLIED OR STATUTORY, WITH RESPECT TO THE MATERIALS OR THE ACCURACY OF ANY INFORMATION CONTAINED IN THE MATERIALS, INCLUDING, WITHOUT LIMITATION, ANY IMPLIED WARRANTY OF MERCHANTABILITY, ACCURACY, SATISFACTORY QUALITY, FITNESS FOR A PARTICULAR PURPOSE, USABILITY, INTEGRATION OR NON-INFRINGEMENT AND ALL SUCH WARRANTIES ARE HEREBY EXCLUDED BY WILEY AND ITS LICENSORS AND WAIVED BY YOU.
- WILEY shall have the right to terminate this Agreement immediately upon breach of this Agreement by you.
- You shall indemnify, defend and hold harmless WILEY, its Licensors and their respective directors, officers, agents and employees, from and against any actual or threatened claims, demands, causes of action or proceedings arising from any breach of this Agreement by you.
- IN NO EVENT SHALL WILEY OR ITS LICENSORS BE LIABLE TO YOU OR ANY OTHER PARTY OR ANY OTHER PERSON OR ENTITY FOR ANY SPECIAL, CONSEQUENTIAL, INCIDENTAL, INDIRECT, EXEMPLARY OR PUNITIVE DAMAGES, HOWEVER CAUSED, ARISING OUT OF OR IN CONNECTION WITH THE DOWNLOADING, PROVISIONING, VIEWING OR USE OF THE MATERIALS REGARDLESS OF THE FORM OF ACTION, WHETHER FOR BREACH OF CONTRACT, BREACH OF WARRANTY, TORT, NEGLIGENCE, INFRINGEMENT OR OTHERWISE (INCLUDING, WITHOUT LIMITATION, DAMAGES BASED ON LOSS OF PROFITS, DATA, FILES, USE, BUSINESS OPPORTUNITY OR CLAIMS OF THIRD PARTIES), AND WHETHER OR NOT THE PARTY HAS BEEN ADVISED OF THE POSSIBILITY OF SUCH DAMAGES. THIS LIMITATION SHALL APPLY NOTWITHSTANDING ANY FAILURE OF ESSENTIAL PURPOSE OF ANY LIMITED REMEDY PROVIDED HEREIN.
- Should any provision of this Agreement be held by a court of competent jurisdiction to be illegal, invalid, or unenforceable, that provision shall be deemed amended to achieve as nearly as possible the same economic effect as the original provision, and the legality, validity and enforceability of the remaining provisions of this Agreement shall not be affected or impaired thereby.
- The failure of either party to enforce any term or condition of this Agreement shall not constitute a waiver of either party's right to enforce each and every term and condition of this Agreement. No breach under this agreement shall be deemed waived or excused by either party unless such waiver or consent is in writing signed by the party granting such waiver or consent. The waiver by or consent of a party to a breach of any provision of this Agreement shall not operate or be construed as a waiver of or consent to any other or subsequent breach by such other party.
- This Agreement may not be assigned (including by operation of law or otherwise) by you without WILEY's prior written consent.

- Any fee required for this permission shall be non-refundable after thirty (30) days from receipt by the CCC.
- These terms and conditions together with CCC's Billing and Payment terms and conditions (which are incorporated herein) form the entire agreement between you and WILEY concerning this licensing transaction and (in the absence of fraud) supersedes all prior agreements and representations of the parties, oral or written. This Agreement may not be amended except in writing signed by both parties. This Agreement shall be binding upon and inure to the benefit of the parties' successors, legal representatives, and authorized assigns.
- In the event of any conflict between your obligations established by these terms and conditions and those established by CCC's Billing and Payment terms and conditions, these terms and conditions shall prevail.
- WILEY expressly reserves all rights not specifically granted in the combination of (i) the license details provided by you and accepted in the course of this licensing transaction, (ii) these terms and conditions and (iii) CCC's Billing and Payment terms and conditions.
- This Agreement will be void if the Type of Use, Format, Circulation, or Requestor Type was misrepresented during the licensing process.
- This Agreement shall be governed by and construed in accordance with the laws of the State of New York, USA, without regards to such state's conflict of law rules. Any legal action, suit or proceeding arising out of or relating to these Terms and Conditions or the breach thereof shall be instituted in a court of competent jurisdiction in New York County in the State of New York in the United States of America and each party hereby consents and submits to the personal jurisdiction of such court, waives any objection to venue in such court and consents to service of process by registered or certified mail, return receipt requested, at the last known address of such party.

#### WILEY OPEN ACCESS TERMS AND CONDITIONS

Wiley Publishes Open Access Articles in fully Open Access Journals and in Subscription journals offering Online Open. Although most of the fully Open Access journals publish open access articles under the terms of the Creative Commons Attribution (CC BY) License only, the subscription journals and a few of the Open Access Journals offer a choice of Creative Commons Licenses. The license type is clearly identified on the article.

##### **The Creative Commons Attribution License**

The [Creative Commons Attribution License \(CC-BY\)](#) allows users to copy, distribute and transmit an article, adapt the article and make commercial use of the article. The CC-BY license permits commercial and non-

##### **Creative Commons Attribution Non-Commercial License**

The [Creative Commons Attribution Non-Commercial \(CC-BY-NC\) License](#) permits use, distribution and reproduction in any medium, provided the original work is properly cited and is not used for commercial purposes.(see below)

##### **Creative Commons Attribution-Non-Commercial-NoDerivs License**

The [Creative Commons Attribution Non-Commercial-NoDerivs License](#) (CC-BY-NC-ND) permits use, distribution and reproduction in any medium, provided the original work is properly cited, is not used for commercial purposes and no modifications or adaptations are made. (see below)

##### **Use by commercial "for-profit" organizations**

Use of Wiley Open Access articles for commercial, promotional, or marketing purposes requires further explicit permission from Wiley and will be subject to a fee.

Further details can be found on Wiley Online Library <http://olabout.wiley.com/WileyCDA/Section/id-410895.html>

#### **Other Terms and Conditions:**

v1.10 Last updated September 2015

Questions? [customer@copyright.com](mailto:customer@copyright.com) or +1-855-239-3415 (toll free in the US) or +1-978-646-2777.

## JOHN WILEY AND SONS LICENSE TERMS AND CONDITIONS

Nov 26, 2018

Total

**0.00 USD**

This Agreement between Alexey Yurikov ("You") and John Wiley and Sons ("John Wiley and Sons") consists of your license details and the terms and conditions provided by John Wiley and Sons and Copyright Clearance Center.

License Number	4473350464012
License date	Nov 20, 2018
Licensed Content Publisher	John Wiley and Sons
Licensed Content Publication	Journal of Geophysical Research: Solid Earth
Licensed Content Title	Sorption-Induced Deformation and Elastic Weakening of Bentheim Sandstone
Licensed Content Author	Alexey Yurikov, Maxim Lebedev, Gennady Y. Gor, et al
Licensed Content Date	Oct 27, 2018
Licensed Content Volume	0
Licensed Content Issue	0
Licensed Content Pages	13

BACK

Type of use	Dissertation/Thesis
Requestor type	Author of this Wiley article
Format	Print and electronic
Portion	Full article
Will you be translating?	No
Title of your thesis / dissertation	Experimental and theoretical study of effects of varying hydration on elastic properties and microstructure of shales and sandstones
Expected completion date	Dec 2018
Expected size (number of pages)	1
Requestor Location	Alexey Yurikov 26 Dick Perry Avenue  Kensington, other Australia Attn:
Publisher Tax ID	EU826007151
Total	<b>0.00 USD</b>
Terms and Conditions	

### TERMS AND CONDITIONS

This copyrighted material is owned by or exclusively licensed to John Wiley & Sons, Inc. or one of its group companies (each a "Wiley Company") or handled on behalf of a society with which a Wiley Company has exclusive publishing rights in relation to a particular work (collectively "WILEY"). By clicking "accept" in connection with completing this licensing transaction, you agree that the following terms and conditions apply to this transaction (along with the billing and payment terms and conditions established by the Copyright Clearance Center Inc., ("CCC's Billing and Payment terms and conditions"), at the time that you opened your RightsLink account (these are available at any time at <http://myaccount.copyright.com>).

#### Terms and Conditions

<https://s100.copyright.com/MyAccount/web/jsp/viewprintablelicensefrommyorders.jsp?ref=33456537-a32a-4222-800d-e46caa48e441&email=>

1/3

- The materials you have requested permission to reproduce or reuse (the "Wiley Materials") are protected by copyright.
- You are hereby granted a personal, non-exclusive, non-sub licensable (on a stand-alone basis), non-transferable, worldwide, limited license to reproduce the Wiley Materials for the purpose specified in the licensing process. This license, **and any CONTENT (PDF or image file) purchased as part of your order**, is for a one-time use only and limited to any maximum distribution number specified in the license. The first instance of republication or reuse granted by this license must be completed within two years of the date of the grant of this license (although copies prepared before the end date may be distributed thereafter). The Wiley Materials shall not be used in any other manner or for any other purpose, beyond what is granted in the license. Permission is granted subject to an appropriate acknowledgement given to the author, title of the material/book/journal and the publisher. You shall also duplicate the copyright notice that appears in the Wiley publication in your use of the Wiley Material. Permission is also granted on the understanding that nowhere in the text is a previously published source acknowledged for all or part of this Wiley Material. Any third party content is expressly excluded from this permission.
- With respect to the Wiley Materials, all rights are reserved. Except as expressly granted by the terms of the license, no part of the Wiley Materials may be copied, modified, adapted (except for minor reformatting required by the new Publication), translated, reproduced, transferred or distributed, in any form or by any means, and no derivative works may be made based on the Wiley Materials without the prior permission of the respective copyright owner. **For STM Signatory Publishers clearing permission under the terms of the STM Permissions Guidelines only, the terms of the license are extended to include subsequent editions and for editions in other languages, provided such editions are for the work as a whole in situ and does not involve the separate exploitation of the permitted figures or extracts**, You may not alter, remove or suppress in any manner any copyright, trademark or other notices displayed by the Wiley Materials. You may not license, rent, sell, loan, lease, pledge, offer as security, transfer or assign the Wiley Materials on a stand-alone basis, or any of the rights granted to you hereunder to any other person.
- The Wiley Materials and all of the intellectual property rights therein shall at all times remain the exclusive property of John Wiley & Sons Inc, the Wiley Companies, or their respective licensors, and your interest therein is only that of having possession of and the right to reproduce the Wiley Materials pursuant to Section 2 herein during the continuance of this Agreement. You agree that you own no right, title or interest in or to the Wiley Materials or any of the intellectual property rights therein. You shall have no rights hereunder other than the license as provided for above in Section 2. No right, license or interest to any trademark, trade name, service mark or other branding ("Marks") of WILEY or its licensors is granted hereunder, and you agree that you shall not assert any such right, license or interest with respect thereto
- NEITHER WILEY NOR ITS LICENSORS MAKES ANY WARRANTY OR REPRESENTATION OF ANY KIND TO YOU OR ANY THIRD PARTY, EXPRESS, IMPLIED OR STATUTORY, WITH RESPECT TO THE MATERIALS OR THE ACCURACY OF ANY INFORMATION CONTAINED IN THE MATERIALS, INCLUDING, WITHOUT LIMITATION, ANY IMPLIED WARRANTY OF MERCHANTABILITY, ACCURACY, SATISFACTORY QUALITY, FITNESS FOR A PARTICULAR PURPOSE, USABILITY, INTEGRATION OR NON-INFRINGEMENT AND ALL SUCH WARRANTIES ARE HEREBY EXCLUDED BY WILEY AND ITS LICENSORS AND WAIVED BY YOU.
- WILEY shall have the right to terminate this Agreement immediately upon breach of this Agreement by you.
- You shall indemnify, defend and hold harmless WILEY, its Licensors and their respective directors, officers, agents and employees, from and against any actual or threatened claims, demands, causes of action or proceedings arising from any breach of this Agreement by you.
- IN NO EVENT SHALL WILEY OR ITS LICENSORS BE LIABLE TO YOU OR ANY OTHER PARTY OR ANY OTHER PERSON OR ENTITY FOR ANY SPECIAL, CONSEQUENTIAL, INCIDENTAL, INDIRECT, EXEMPLARY OR PUNITIVE DAMAGES, HOWEVER CAUSED, ARISING OUT OF OR IN CONNECTION WITH THE DOWNLOADING, PROVISIONING, VIEWING OR USE OF THE MATERIALS REGARDLESS OF THE FORM OF ACTION, WHETHER FOR BREACH OF CONTRACT, BREACH OF WARRANTY, TORT, NEGLIGENCE, INFRINGEMENT OR OTHERWISE (INCLUDING, WITHOUT LIMITATION, DAMAGES BASED ON LOSS OF PROFITS, DATA, FILES, USE, BUSINESS OPPORTUNITY OR CLAIMS OF THIRD PARTIES), AND WHETHER OR NOT THE PARTY HAS BEEN ADVISED OF THE POSSIBILITY OF SUCH DAMAGES. THIS LIMITATION SHALL APPLY NOTWITHSTANDING ANY FAILURE OF ESSENTIAL PURPOSE OF ANY LIMITED REMEDY PROVIDED HEREIN.
- Should any provision of this Agreement be held by a court of competent jurisdiction to be illegal, invalid, or unenforceable, that provision shall be deemed amended to achieve as nearly as possible the same economic effect as the original provision, and the legality, validity and enforceability of the remaining provisions of this Agreement shall not be affected or impaired thereby.
- The failure of either party to enforce any term or condition of this Agreement shall not constitute a waiver of either party's right to enforce each and every term and condition of this Agreement. No breach under this agreement shall be deemed waived or excused by either party unless such waiver or consent is in writing signed by the party granting such waiver or consent. The waiver by or consent of a party to a breach of any provision of this Agreement shall not operate or be

construed as a waiver of or consent to any other or subsequent breach by such other party.

- This Agreement may not be assigned (including by operation of law or otherwise) by you without WILEY's prior written consent.
- Any fee required for this permission shall be non-refundable after thirty (30) days from receipt by the CCC.
- These terms and conditions together with CCC's Billing and Payment terms and conditions (which are incorporated herein) form the entire agreement between you and WILEY concerning this licensing transaction and (in the absence of fraud) supersedes all prior agreements and representations of the parties, oral or written. This Agreement may not be amended except in writing signed by both parties. This Agreement shall be binding upon and inure to the benefit of the parties' successors, legal representatives, and authorized assigns.
- In the event of any conflict between your obligations established by these terms and conditions and those established by CCC's Billing and Payment terms and conditions, these terms and conditions shall prevail.
- WILEY expressly reserves all rights not specifically granted in the combination of (i) the license details provided by you and accepted in the course of this licensing transaction, (ii) these terms and conditions and (iii) CCC's Billing and Payment terms and conditions.
- This Agreement will be void if the Type of Use, Format, Circulation, or Requestor Type was misrepresented during the licensing process.
- This Agreement shall be governed by and construed in accordance with the laws of the State of New York, USA, without regards to such state's conflict of law rules. Any legal action, suit or proceeding arising out of or relating to these Terms and Conditions or the breach thereof shall be instituted in a court of competent jurisdiction in New York County in the State of New York in the United States of America and each party hereby consents and submits to the personal jurisdiction of such court, waives any objection to venue in such court and consents to service of process by registered or certified mail, return receipt requested, at the last known address of such party.

#### WILEY OPEN ACCESS TERMS AND CONDITIONS

Wiley Publishes Open Access Articles in fully Open Access Journals and in Subscription journals offering Online Open. Although most of the fully Open Access journals publish open access articles under the terms of the Creative Commons Attribution (CC BY) License only, the subscription journals and a few of the Open Access Journals offer a choice of Creative Commons Licenses. The license type is clearly identified on the article.

##### The Creative Commons Attribution License

The [Creative Commons Attribution License \(CC-BY\)](#) allows users to copy, distribute and transmit an article, adapt the article and make commercial use of the article. The CC-BY license permits commercial and non-

##### Creative Commons Attribution Non-Commercial License

The [Creative Commons Attribution Non-Commercial \(CC-BY-NC\) License](#) permits use, distribution and reproduction in any medium, provided the original work is properly cited and is not used for commercial purposes.(see below)

##### Creative Commons Attribution-Non-Commercial-NoDerivs License

The [Creative Commons Attribution Non-Commercial-NoDerivs License \(CC-BY-NC-ND\)](#) permits use, distribution and reproduction in any medium, provided the original work is properly cited, is not used for commercial purposes and no modifications or adaptations are made. (see below)

##### Use by commercial "for-profit" organizations

Use of Wiley Open Access articles for commercial, promotional, or marketing purposes requires further explicit permission from Wiley and will be subject to a fee.

Further details can be found on Wiley Online Library <http://olabout.wiley.com/WileyCDA/Section/id-410895.html>

#### Other Terms and Conditions:

v1.10 Last updated September 2015

Questions? [customercare@copyright.com](mailto:customercare@copyright.com) or +1-855-239-3415 (toll free in the US) or +1-978-646-2777.